Massive star formation as seen by infrared long-baseline interferometry

Rebekka Barbara Grellmann

Massive star formation as seen by infrared long-baseline interferometry

Rebekka Barbara Grellmann

Dissertation der Fakultät für Physik
Dissertation of the Faculty of Physics

der Ludwig-Maximilians-Universität München
at the Ludwig Maximilian University of Munich

für den Grad des
for the degree of

Doctor rerum naturalium

vorgelegt von Rebekka Barbara Grellmann
presented by

aus Köln
from

München, 13. August 2012

1st Evaluator: Prof. Dr. Thomas Preibisch

2nd Evaluator: Dr. habil. Achim Weiss

Date of the oral exam: 9th October 2012

Abstract

While a detailed picture of low-mass star formation has evolved over the last years, the process of forming high-mass stars is much less understood. One of the main observational limitations is the angular resolution required to resolve the involved processes and structures on small scales. Furthermore, massive young stellar objects are mostly deeply embedded into the surrounding natal cloud and thus obscured by large amounts of gas and dust, what makes an observation in the optical impossible. In this thesis I use the recently developed technique of long-baseline infrared-interferometry, which provides an angular resolution on the scale of milliarcseconds, to spatially resolve the close circumstellar environment of young O- and B- stars. One possible application of infrared-interferometry is to study the structure and composition of circumstellar disks. Circumstellar disks are important for the star formation process as they can take over part of the angular momentum of the molecular cloud, are part of the jet and outflow as well as accretion mechanisms, and can help to overcome the radiation pressure barrier. Furthermore, circumstellar disks are the places where planets are born. Using MIDI at the VLTI, I spatially resolve for the first time the mid-infrared emission region around the massive, young stellar object NGC 2264 IRS 1. Measurements at different position angles indicate an asymmetric structure, possibly due to a circumstellar disk. Employing a radiative transfer code I find that the parameters for the disk are consistent with an overall geometrical model based on the jet-like feature seen to the north-east of IRS 1. This result supports the assumption that massive young stellar objects form via accretion from circumstellar disks. The current generation of infrared interferometric instruments does not only come along with a high spatial resolution but also with spectroscopic capabilities, which can provide additional information about the chemical composition and kinematics by resolving spectral bands and lines. Using AMBER at the VLTI in its medium resolution mode I spatially and spectrally resolved the near-infrared emission region around the Herbig Be star MWC 147. The size of the continuum near-IR emission region indicates an emission origin located inside the dust-sublimation radius. Looking at the spectrum we can detect the Brackett γ emission line of atomic hydrogen. The size of the line emitting region is comparable to that of the continuum emission region and thus points to the disk wind rather than magnetospheric accretion or X-wind scenario. We do not detect any emission lines originating from molecules. This result is in contrast to the picture of an inner gaseous disk whose opacity is caused by molecular emission lines and points to a more complex composition of material than previously thought. Another application of infrared-interferometry is the detection and characterization of close companions. While spectroscopy can resolve very close companions ($\leq$ 1 AU), adaptive optics searches are only sensitive to companions with separations of several tens to hundred AU. The remaining gap can only be filled employing infrared-interferometric techniques. Furthermore, companions in the observed range are attractive targets for tracing their orbits due to orbital periods on the scale of only years. I used AMBER to search for companions around a sample of O- and B-type stars in two star forming regions: In the Upper Scorpius region, part of the Scorpius-Centaurus association,and in the Orion Nebula Cluster, part of the Orion OB1 association. In Upper Scorpius, no previously unknown companions are detected using interferometry, but indications for two new companions come from archival X-ray ROSAT data. Using the new orbit point as measured with AMBER for the ν Sco system we can perform an orbit fit which yields a total system mass of 22 $M_\odot$ and an orbital period of $\sim$ 9 yrs. Including the new X-ray companions we find $\sim$ 2.0 companions per primary for our Upper Scorpius sample. In the Orion Nebula Cluster we find hints

for the presence of two new companions, around θ^1 Ori D and NU Ori. We furthermore reobserve the already known companions around θ^1 Ori A and θ^1 Ori C. Our new AMBER measurements confirm the previously determined orbital and stellar parameters of the θ^1 Ori C system and indicate that the companion of θ^1 Ori A is physically related to the primary and not just a chance projection. Including the new companions we find $\geq$ 2.2 companions per primary star on average for our sample of stars in the Orion Nebula Cluster. The number of companion stars per primary is comparable for the both observed region and around four times higher than for low mass stars.

För ming Mamm un minge Papp

Contents

List of Figures

List of Tables

Chapter 1

Introduction

1.1 Star formation

This chapter provides a short overview of the basic processes and theories important for the understanding of star formation. Although an elementary picture of the processes involved in star formation has evolved over the last decades, many questions are still unsolved and need to be investigated. This includes questions like: Do high-mass and low-mass stars form in the same way or by different processes? Which fraction of stars forms in multiple systems and on which timescales do such systems disperse? What is the role of circumstellar disks and how do they evolve? What is the origin of jets and outflows ejected by young stars? How important is triggered star formation and which are the relevant processes (e.g., supernova shocks, stellar winds, cloud-cloud collisions)?

The way stars form also has a large impact on other astrophysical fields. The star formation rate, e.g., influences the dynamics, structure, and evolution of galaxies. Furthermore, also the planet formation process is closely connected to the formation of the central star and in particular to the structure and evolution of circumstellar disks.

This chapter follows mainly the detailed descriptions of our current understanding as described in Schulz (2005), Stahler & Palla (2005), McKee & Ostriker (2007), Zinnecker & Yorke (2007), and Bodenheimer (2011).

1.1.1 The Interstellar Medium

The space between the stars is not empty, but filled with what is called the *interstellar medium (ISM)*. New stars can be formed in the ISM under certain conditions (which will be discussed later). The processes that are taking place in the ISM and its different phases are therefore important to understand the star formation process. The composition of the matter in the ISM is: $\sim 70\,\%$ of the mass is hydrogen, $\sim 28\,\%$ helium, and $\sim 2\,\%$ heavier elements (e.g., oxygen, carbon, nitrogen). Nearly all of this matter exists in the gas phase, only $\sim 1\,\%$ is solid (Schulz, 2005), i.e., dust. The interstellar gas exists in the galaxy in several rather stable phases connected to different temperatures: the hot phase at a temperature of $T \sim 10^6\,\mathrm{K}$, (luminous) ionized gas at $T \sim 10^4\,\mathrm{K}$, neutral gas at $T \sim 10^2\,\mathrm{K}$, and molecular gas at $T \leq 10\,\mathrm{K}$ (Cox, 2005).

Discussing the gas content of the ISM, neutral means that the hydrogen atoms are neutral. The neutral gas can be studied by observing absorption lines (the light coming from a background star shining through the neutral gas) or emission lines from the atoms and ions in the neutral gas. As the

most abundant element in the ISM is hydrogen, it is not surprising that the most famous emission line observed is the so-called *21 cm line* originating from the atomic transition between the two hyperfine levels of the hydrogens ground state (spins of proton and electron parallel or antiparallel).

If the interstellar gas is located close enough to, e.g., a hot main-sequence star (or a cluster of hot stars), the radiation emitted by the star will ionize the (hydrogen) gas. The ionized regions are then called *H II regions*. The radius of the H II region is depending on the luminosity of the star and the density of the gas and is called *Strömgren radius*. If the star emits photons with enough energy further elements can be ionized. Then inside the hydrogen ionization sphere, a helium and optionally further ionization spheres will form. For very hot stars the ionization spheres for H and He will almost be identical. The emission coming from H II regions consists of free-free emission (e.g., Bremsstrahlung), free-bound radiation (recombination continuum), recombination line emission, 2-quantum emission, and forbidden emission line radiation (Povich, 2012).

The hot phase ($T \sim 10^6\,K$) of the ISM was discovered first by the presence of absorption lines of O VI in spectra of stars and also through the detection of soft X-ray emission. It is not clear how this hot phase is generated, but one possibility is that shock fronts of supernovae explosions insert large amounts of kinetic energy into the gas (Pradas & Kerp, 2003).

The most important phase of the ISM in the context of star formation is the molecular gas. This phase will therefore be discussed in more detail.

Molecular Clouds

The *molecular clouds (MCs)* are the densest ($n \sim 100 - 1000\,cm^{-3}$) and coldest ($\sim 10 - 20\,\mathrm{K}$) parts of the interstellar gas and the places where star formation occurs (Bergin & Tafalla, 2007). The temperatures are the result of a balance between heating and cooling mechanisms. The clouds are heated by cosmic rays and the radiation emitted by nearby stars. Typical masses of MCs are between 10^3 and several 10^4 solar masses ($\mathrm{M}_\odot$), but can be as high as $10^6\,\mathrm{M}_\odot$ for so-called *giant molecular clouds (GMCs)* (Blitz et al., 2007; Fukui & Kawamura, 2010). Molecular clouds can be observed in thermal continuum from the infrared-, to mm-wavelengths. Spectral lines from various molecules can be detected in a wide range of spectral windows, ranging from UV- and optical observations down to radio frequencies. The most abundant molecule, H_2, is difficult to observe due to its lack of a dipole moment. Several H_2 lines can be seen in the UV, but observations of this lines in dense material are difficult due to the extinction caused by dust (see below). A solution for this problem is to measure carbon-monoxide (CO) instead, which is the second most abundant molecule (about a factor of 10^{-4} relative to H_2). As the emission from the most abundant isotope ^{12}CO becomes optically thick in the denser clouds, the rarer (around 100 times) isotope ^{13}CO is often used (Snow & McCall, 2006).

Molecular clouds are observed to have structures over a wide range of scales (Bodenheimer, 2011). They are fragmented and clumpy. Star formation takes place in the densest parts of MCs, in *clumps* and *cores.* Clumps are large, more massive ($\sim 10^3\,\mathrm{M}_\odot$) structures, which are believed to form stellar clusters (Banerjee et al., 2009). Cores have typical densities of $n \sim 10^5\,cm^{-3}$ (Frau et al., 2012), are thought to be gravitationally bound, and regions forming single or binary stars (Bergin & Tafalla, 2007).

Dust

Although only about $\sim 1\%$ of the ISM mass is found to be dust, it is an important ingredient for star formation as it re-processes and scatters radiation and serves as catalysator for the formation of several molecules, in particular H_2 (Gavilan et al., 2012). Dust absorbs a large part of the UV photons

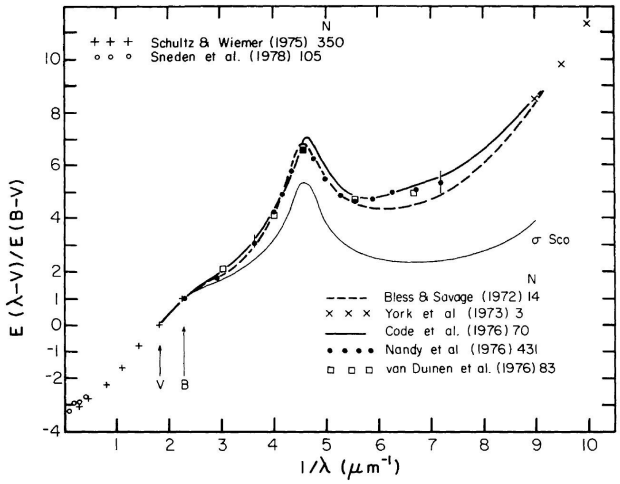

Figure 1.1: Averaged normalized interstellar extinction depending on the wavelength from Savage & Mathis (1979).The number behind the references for the various curves gives the number of objects used to derive each curve. The extinction bump at 4.6 μm^{-1} is due to graphitic dust particles.

emitted by stars. As they are re-emitted in form of IR or mm-wavelength radiation for which the interstellar gas is transparent, dust helps to cool the molecular cloud. The interaction processes of dust and radiation are very complex and one usually uses *radiative transfer models* (see Sect. 1.1.2) to understand how the photons propagate through a dusty medium.

The combined effect of scattering and absorption is also called *extinction*. The amount of extinction is wavelength dependent. Dust particles in the ISM have typical sizes of 0.01 to 1 μm and thus scatter more blue than red light (Draine, 2009). Astronomical objects observed through the dust appear more red, which is known as *interstellar reddening*. In Fig. 1.1 typical interstellar extinction curves are shown. Such curves are obtained by using photometric observations of two stars (having identical spectral type and luminosity) of which only one is reddened. The difference in magnitudes at two wavelengths λ_1, λ_2 is called the *color excess* $E(\lambda_1 - \lambda_2)$. The *standard color excess* is defined by using the central wavelengths of the B and V bands $\lambda_B = 0.44$ μm and $\lambda_V = 0.55$ μm and is usually denoted as $E(B - V)$. The extinction curve is then given by $E(\lambda - V)/E(B - V)$. In Fig 1.1 one can see an extinction bump at 4.6 μm^{-1}. This feature is due to the absorption of graphitic dust particles. Obviously, there also exist several other absorption features. They are, however, much more narrow and observed both in emission and absorption. The correlation between the *visual extinction* A_V in magnitudes (a commonly used quantity to describe the opaqueness of a cloud) and the standard color excess is

$$A_V = E(B - V) \cdot R_V,$$

where R_V is the *ratio of total to selective extinction* and is known to be mostly ~ 3.1 from observations, but may vary between ~ 2.1 (towards clouds at high galactic latitudes) and ~ 5 (towards molecular clouds) (Zagury, 2012).

The dust in the interstellar medium consists mainly of amorphous silicates and carbonaceous dust. The formation of dust is generally thought to happen in the winds and outflows during the late stages of stellar evolution (Asano et al., 2012). *Asymptotic giant branch stars (AGB stars)* of spectral type M as well as *red supergiants (RSGs)* are mainly responsible for the formation of silicate dust, whereas carbon dust is produced from AGB stars of spectral type C as well as Wolf-Rayet stars. Furthermore, more exotic dust is observed to form also during nova and supernova explosions. Once injected into

the ISM, the properties of dust are changed in shocks, through cosmic rays and due to accretion and coagulation in dense molecular clouds and circumstellar envelopes and disks (see also Sect. 1.3). The silicate dust formed from the AGBs and RSGs is observed to consist of $\sim 15\%$ crystalline dust, which will be amorphized probably by the cosmic ray radiation, such that the percentage of crystalline silicates in the average ISM is only a few precent (Henning, 2010).

Dust can be destroyed through photodesorption (which is not very efficient) or by *sputtering* (atoms or molecules are kicked off the grain surface when colliding with other particles). Such collisions are not efficient for high particle energies, i.e. MeV to GeV. Thus, cosmic rays do not efficiently destroy the dust grains.

1.1.2 Radiative Transfer

The expression *radiative transfer* denotes the propagation of electromagnetic radiation through some medium. Radiative transfer is essential for astrophysics as radiation originating from astronomical objects never reaches the observer without interaction with the ISM. There, the radiation can be absorbed, scattered, and re-emitted.

The fundamental equation of radiative transfer describes the variation of the intensity dI over a path with length ds at a frequency ν in a medium with density ρ. The derivation of the radiative transfer equation can be found in, e.g., Chandrasekhar (1960). The properties of the medium are given by the absorption-coefficient (and/or scattering-coefficient) κ_ν and emission-coefficient ϵ_ν (which can itself depend on the radiation field). The radiative transfer equation is then given by:

$$\frac{dI_\nu}{ds} = -\kappa_\nu \rho \, I_\nu + \epsilon_\nu \rho. \tag{1.1}$$

The solution of the radiative transfer equation is

$$I_\nu(s) = I_\nu(0)\, e^{-\tau(s,0)} + \int_0^s S_\nu \, e^{-\tau(s,s')} \kappa_\nu \rho ds', \tag{1.2}$$

with τ being the *optical depth* between the points s and s' defined by:

$$\tau(s, s') = \int_{s'}^{s} \kappa_\nu \rho \, ds. \tag{1.3}$$

Equ. 1.2 can, however, only be solved analytically in special cases and usually has to be solved numerically, e.g., using Monte-Carlo codes.

1.1.3 Low-Mass Star Formation

Low-mass stars form from the collapse of gravitationally bound cores in molecular clouds Bodenheimer (2011); Hennebelle (2012). To start the star formation process, a large mass of gas has to be collected in such a small space that the gas becomes self-gravitating. The mass, which is needed to start gravitational contraction (by some perturbation in a homogenous cloud) was first calculated by Jeans (1902) assuming an isothermal gas and including only thermal effects and gravitation. It is therefore called *(thermal) Jeans mass* $M_{\rm Jeans}$:

$$M_{\rm Jeans} \propto T^{3/2} \rho^{-1/2}. \tag{1.4}$$

Here, T is the temperature and ρ the density of the molecular cloud, i.e., the Jeans mass is higher for higher temperature of the MC and smaller for denser MCs. However, various other physical effects

may hinder the cores from collapsing, although the thermal Jeans-mass is reached, e.g., rotation, turbulence, and magnetic fields. The effect of rotation does not seem to hinder the initial collapse of molecular cores significantly, however, it has an important impact in the later stages of star formation. The angular momentum caused by rotation of the cloud makes the angular velocity increase the more the core is contracting. The centrifugal force will thus be too high to allow the core to collapse into stellar dimensions. Solutions for this problem are the evolution of circumstellar disks (see Sect. 1.3) and the evolution of multiple systems (see Sect. 1.2). Magnetic fields are also an important ingredient, as they can prevent the collapse on the one hand, and on the other hand may help to transport angular momentum away from the cores (Li et al., 2010; Dapp et al., 2012). Somehow similar to the thermal Jeans-mass, one can define a magnetic Jeans-mass. However, even if the cores have lower masses than the magnetic Jeans-mass, they can collapse despite the presence of magnetic fields through *ambipolar diffusion* (drift of neutral particles across magnetic field lines, Spitzer 1978). In the case of turbulence, one can similarly define a turbulent Jeans-mass. The origin of interstellar turbulence is still debated (Ballesteros-Paredes et al., 2007; McKee & Ostriker, 2007; Tachihara et al., 2012). It may be due to, e.g., colliding flows or magnetorotational instabilities in the galactic disk. Although the turbulence is on large scales the main mechanism to prevent the collapse of cores, shock patterns created randomly on small scales can lead to a compression of regions located behind these shocks and thus to a collapse. Finally it should be mentioned, that the collapse of molecular cloud cores could also be triggered by events like supernovae shocks, cloud-cloud collisions, or winds from massive stars (e.g., Gritschneder et al. 2011; Elmegreen 2011; Duarte-Cabral et al. 2011; Boss & Keiser 2012).

Once the molecular cloud cores become unstable, the protostellar phase starts. The pre-stellar core is optically thin in mid-infrared to sub-mm wavelengths and can radiate the released energy away freely. As its temperature thus stays nearly constant, this phase can be approximated with an isothermal collapse. However, at a density of $\sim 10^{-13}\,\mathrm{g\,cm^{-3}}$ the core becomes optically thick in its center and is then called *protostar*. The radiation can not freely escape anymore, the collapse slows down, and the temperature rises until the center of the core has a temperature of $\sim 1600\,\mathrm{K}$. At this temperature, the molecular hydrogen starts to dissociate. The released thermal energy is mostly used for the hydrogen dissociation process and the temperature thus increases much slower than before. This leads to a second collapse of the core center until most of the hydrogen molecules have dissociated. At the end of the second collapse a stellar core with a temperature of $\sim 20,000\,\mathrm{K}$, a density of $\sim 10^{-2}\,\mathrm{g\,cm^{-3}}$, and a mass of $10^{-3}\,\mathrm{M_\odot}$ has formed. Most of the final stellar mass is at that stage still located in the outer, much thinner parts.

During the protostellar collapse phase, which takes around 10^5 yrs (Bodenheimer, 2011), a circumstellar disk starts to form due to the initial rotation and thus angular momentum in the cloud. Part of this angular momentum can be taken away from the material finally building the star by, e.g., the disks viscosity (see Sect. 1.3). Furthermore, bipolar outflows remove additional angular momentum already in the protostellar phase. Material from the disk can accrete onto the central core and emits radiation due to the kinetic infall energy. This radiation is absorbed by the remaining circumstellar envelope and re-emitted at infrared wavelengths. The central *young stellar object (YSO)* begins to slowly contract. In the later phases of the accretion process the accretion rate decreases and the infalling envelope becomes optically thin. This phase is called the *pre-main-sequence (PMS)* phase. Low-mass objects with masses up to $\sim 2\,\mathrm{M_\odot}$ in the PMS phase are called *classical T Tauri stars (CTTSs)*. Pre-main sequence stars from $\sim 2\,\mathrm{M_\odot}$ to $\sim 8\,\mathrm{M_\odot}$ are called *Herbig Ae/Be (HAeBe) stars*. PMS objects are still surrounded by their circumstellar disks. The evolution of the disks will be discussed in more detail in Sect. 1.3. Circumstellar disks are dissipated by photoevaporation after around $1 - 10\,\mathrm{Myrs}$.

Finally, once the interior of the YSO is hot enough, nuclear reactions, i.e., hydrogen burning, start.

The formation of the star is finished and it reaches the main-sequence in the *Hertzsprung-Russell diagram*, or more precisely the *zero-age main sequence (ZAMS)*. The total time a star needs to form depends on its mass. The more massive the star is, the faster it will evolve to the ZAMS stage. For a star with final mass of $0.5\,M_\odot$ the time spent on the pre-main sequence phase is around $1.5 \cdot 10^8$ yrs and for a star with a final mass of $1\,M_\odot$ (e.g., our Sun) around $4 \cdot 10^7$ yrs. For a star with final mass of $3\,M_\odot$ to reach the ZAMS, it takes around $2 \cdot 10^6$ yrs (Bodenheimer, 2011). These numbers, however, can vary for different evolutionary models and depend on the exact definition of the ZAMS.

The formation of low-mass stars can be divided into an evolutionary sequence also from the observational point of view. The classes (0-III) were introduced by characterizing the objects by means of their observed *spectral energy distribution (SED)* (Lada, 1987; Andre et al., 1993, 2000). In Fig. 1.2 the SEDs connected to each class are shown together with the corresponding evolutionary stage.

Class 0 objects are in an early protostellar evolutionary stage. The central protostars are surrounded by large amounts of gas and dust. The mass of the protostar is at that stage less than half the mass of the surrounding dusty envelope. Thus, only radiation at longer wavelengths is able to escape and can be observed. Class 0 objects are defined via their bolometric temperatures (Chen et al., 1995) or the ratio between bolometric and submillimeter luminosity (Andre et al., 1993).

The other classes are identified using the slope α between 2.2 μm and 10 μm, 25 μm, respectively:

$$\alpha = \frac{d \log \lambda F_\lambda}{d \log \lambda},$$

where F_λ is the flux emitted at a certain wavelength λ. SEDs of class I sources have a slope of $\alpha > 0$. They are evolved protostars and usually have both, circumstellar disks and envelopes. Class II sources are usually believed to be in the pre-main sequence phase, i.e., have circumstellar disks, but less circumstellar dust in an envelope than Class I sources (i.e., T Tauri or HAeBe stars). They have slopes between around -1.5 and 0. Finally, Class III sources ($\alpha \leq -1.5$) are thought to be pre-main sequence or young main-sequence stars with little or no circumstellar material or disks. However, the geometry (e.g., the inclination of the object) has a significant impact on the shape of the SED (Dunham et al., 2010; Commercon et al., 2012; Offner et al., 2012). The same source could either appear as Class I or Class II source, if the inclination angle is large (i.e., the object is obscured by the disk) or low (i.e., the central star is visible).

1.1.4 High-Mass Star Formation

Compared to the formation of low-mass stars, less is known about the formation process of massive stars ($M > 8\,M_\odot$). Although massive stars (and also *massive young stellar objects, MYSOs*) are much brighter than low-mass stars and thus should be much easier to observe, the number of observations of adequate objects is still small due to several reasons.

Stars with higher masses are much rarer than star with lower masses, which can easily be seen from the *initial mass function (IMF)* (an empirical law which gives the number of stars with a certain mass built):

$$\frac{dN(M)}{d \log M} \propto M^x.$$

The exponent x depends on the model chosen and is often thought to vary for different mass ranges. Commonly used values are -1.35 (Salpeter, 1955) and for the upper IMF -1.3 (Kroupa, 2001). Additionally, low-mass stars evolve much slower and thus live much longer than high-mass stars. A $\sim 1\,M_\odot$ star lives, e.g., around 2000 times longer than a star with a mass of $\sim 30\,M_\odot$. Therefore, we can expect that around $2 \cdot 10^5$ more stars with $\sim 1 - -2\,M_\odot$ than with $\sim 25 - -30\,M_\odot$ exist.

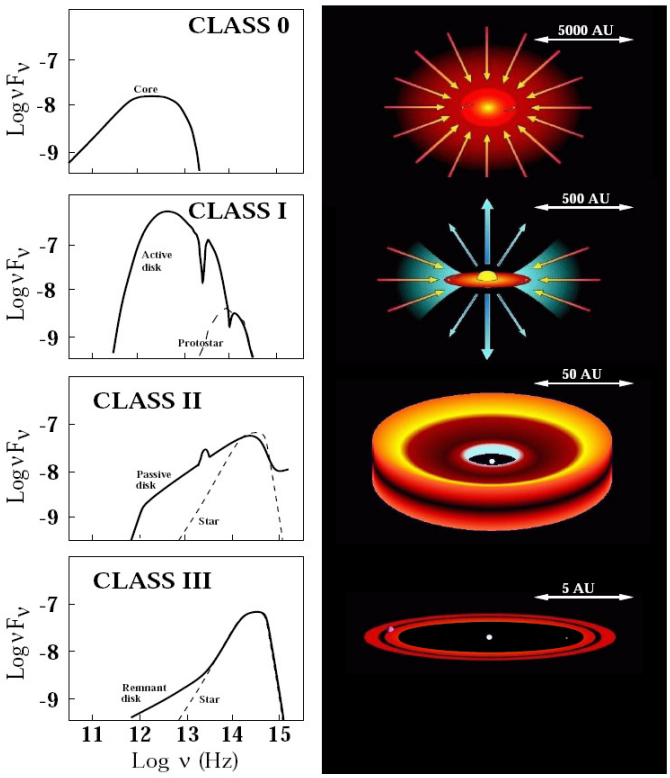

Figure 1.2: Classification scheme for young stellar objects from van Boekel et al. (2006), pictures of separate stages: M. McCaughrean. *Left:* Typical shapes of SEDs connected to the classes as defined by Andre et al. (2000). *Right:* Artists impression of the different circumstellar environments.

Furthermore, massive stars are seldomly found in isolation, such that their surroundings are very complex due to gravitational interactions with the cluster members, and outflows, winds, and ionizing radiation coming from neighboring stars. Other factors which complicate the observation of high-mass YSOs are that massive star forming regions are mostly far away (e.g., more than 2 kpc for the Carina Nebula in contrast to, e.g., $\sim$ 140 pc for Taurus Auriga) and that the MYSOs are deeply embedded into their parental clouds. Thus, they can usually only be observed at IR to mm wavelengths, at which the radiation is able to escape from the dense surroundings. The typically large distances of massive YSOs lead to a decrease in flux and require a very good angular resolution (i.e., big telescopes or interferometers) to resolve the complex structure.

Currently, three competing concepts of possible formation scenarios for high-mass stars are discussed: monolithic collapse and disk accretion in isolated cores, competitive accretion in a protocluster environment, and stellar collisions and mergers (Bonnell et al., 1998; Zinnecker & Bate, 2002). It is also possible that each of these three formation scenarios occurs in nature depending on the conditions in the molecular cloud.

The *monolithic collapse* scenario is in principle a scaled-up version of the formation of low-mass stars (see Sect. 1.1.3). In this scenario, massive stars would form from high-mass cores, i.e., the mass of the core would determine the mass of the star taking into account an efficiency factor, which is usually assumed to be $\sim$ 30% (Alves et al., 2007). Only little interaction between the cores takes place as soon as they have formed. The radiation pressure problem that would prevent spherical accretion as soon as the protostellar mass exceeds $\sim 10\,M_\odot$ is solved by stellar outflows and accretion via an accretion disk. The outflows open a bipolar cavity in the polar directions. The radiation pressure in the equatorial plane is lowered as the irradiated, heated regions of the circumstellar disk mainly cool in the vertical direction (similar to low-mass star formation). In the innermost parts the radiation then can escape through the bipolar cavity (known as *flashlight effect*, Yorke & Sonnhalter 2002). Furthermore, the accretion disk can transfer angular momentum to the outer regions and thus allows a mass accretion radially inwards (Nakano, 1989). Therefore, an infall of material in this plane is possible. This scenario has been investigated and verified in recent simulations (Krumholz & Bonnell, 2007; Krumholz et al., 2009; Kuiper et al., 2010). Evidence from observations comes from recent observations of circumstellar disks around massive stars (e.g., AFGL 490, Schreyer et al. 2006; IRAS 13481-6124, Kraus et al. 2010; IRAS 18151-1208, Fallscheer et al. 2011; NGC 7538 IRS 1, Beuther et al. 2012; IRAS 18162-2048, Carrasco-González et al. 2012). Furthermore, molecular outflows or collimated jets (e.g., Cunningham et al., 2009, 2011) are often interpreted as evidence for ongoing accretion.

In the *competitive accretion* scenario (Bonnell, 2000, 2005; Bonnell & Bate, 2006; Hsu et al., 2011) the stars formed in a cluster compete for the available reservoir of material. Those which are located in the center of the cluster potential can accrete much more material than the stars further out. In such a scenario the final mass of a star does not depend on the mass of the core but primarily on its location in the cluster. In this scenario multiple systems should be very common among stars with high masses. The competitive accretion scenario thus results in a distribution of stellar masses and could be a mechanism for producing the IMF. Indeed, massive stars are observed to form in clusters rather than in isolation (Varricatt, 2012; Chini et al., 2012). Furthermore, the competitive accretion model can account for the observed properties of multiple systems. The main disadvantage of the competitive accretion scenario is that too much of the cloud mass ends up in the formation of stars. The model seems thus to be too efficient. This could, however, be due to the presence of magnetic fields and radiative feedback which are currently not included into simulations with high initial cloud masses. Observed circumstellar disks are not in contradiction to the competitive accretion (Clark, 2010).

Finally, it was suggested by Bonnell et al. (1998) and Bally & Zinnecker (2005) that massive stars can form through the collision and merging of protostars with lower masses. Very recently it was shown using N-boy computations that during the evolution of clusters indeed a few single stars per cluster with masses of more than 150 $M_\odot$ will be formed by the mergers of massive binaries (Banerjee et al., 2012a,b). However, such mergers are unlikely to occur in any but the richest clusters and thus are thought to be rare and only relevant for the formation of the most massive stars (Zinnecker & Yorke, 2007; Bonnell & Smith, 2011).

1.2 Binary and Multiple Systems

The last two decades of observations of star forming regions and young stellar clusters has clearly established that most, if not all, stars form in binaries or higher order multiple systems (e.g., Mathieu & Zinnecker 2000; King et al. 2012). In total, the fraction of single systems is about 50% (McKee & Ostriker, 2007; Raghavan et al., 2010a), however, it is correlated with the stellar mass. Stars with higher masses are found to be in binary systems more often than low-mass stars (Preibisch et al., 1999; Chini et al., 2012). Sana et al. (2012) found very recently that over $\sim$ 70% of stars born as O-type star will exchange mass with a companion, what leads to a binary merger in one third of the cases. Furthermore, massive stars are often found in higher order multiple systems,i.e., triple or quadruple systems (Zinnecker & Yorke, 2007). During the last few years, numerical simulations of star cluster formation have reached a level where they can make quite detailed predictions about the multiplicity of the forming stars (see Goodwin et al. 2007). The work of Bate (2009) presents the largest hydrodynamical simulation of star cluster formation to date and provides unprecedented statistical information about the formed stellar systems that can be compared with observational surveys.

1.2.1 Observations

Duquennoy & Mayor (1991) performed a survey of all solar-type field stars within 22 pc distance of the Sun visible from the northern hemisphere. They conclude (taking into account probably missed companions due to their orbital distances and/or low brightness) that the fraction of single stars in their sample is $\sim$ 30%. The distribution of orbital distances peaks at a semi-major axis of $\sim$ 30 AU (Raghavan et al., 2010b). The multiplicity of field stars with later spectral types than G is probably lower than this (around 30%, Lada 2006). However, the fraction of binary or multiple system seems to be much higher when searching among PMS than among main sequence stars (Duchêne et al., 2007; Viana Almeida et al., 2012). For both T Tauri stars and embedded Class I sources it seems to be two times higher than for main sequence objects and for some star-forming regions the fraction of binaries seems to reach 100% (e.g., the Taurus-Aurigae region, Köhler & Leinert 1998).

As mentioned above, high-mass stars show a high frequency of binary and multiple systems. Massive stars are often found to be in hierarchical triples, where the two closer binaries have nearly similar masses and a more distant third companion (Zinnecker & Yorke, 2007). An accurate characterization of multiple stellar systems and their properties is thus one of the most important steps in understanding the star formation process itself. The observed properties of multiple systems, such as their separation distribution and mass ratios, provide important and strong constraints on star-formation theories.

1.2.2 Formation

Several different ideas how binary or multiple systems can form have been developed. The first early ideas were the formation by the breaking of a rapidly rotating object in hydrostatic equilibrium due

to dynamical instability (also known as *fission*) and secondly the capture of a totally independently formed star. While fission in the meantime has been essentially ruled out, capture might still be a possible formation scenario in the cores of dense young clusters. Currently, binaries are thought to form mainly as a result of fragmentation (Offner et al., 2011). However, different kinds of fragmentation will lead to different results. Fragmentation of a low-mass core during its collapse will produce a binary or a small multiple system, whereas fragmentation of a higher mass core will lead to the formation of a small cluster. Furthermore, a fragmentation of the gravitationally unstable circumstellar disk could lead to binary systems. However, in a fragmentation scenario it remains difficult to explain the existence of a large number of close binaries (with separations of lower than or equals to a few AU). Probably a combination of processes is required for their formation.

In the special case of high-mass binaries, the formation process could work through the following processes: Fragmentation of disks or filaments, accretion onto low-mass wide binaries, failed mergers in stellar collisions, disk-assisted capture, or n-body dynamical evolution. The formation through fragmentation works similar than for low-mass objects and, as already mentioned above, can not account for the existence of close massive binaries (which are, however, very often found in the center of hierarchical triples). A possible formation scenario for close binaries would be accretion onto an initially wide low-mass binary. Such an accretion can significantly decrease the separation of the components, while at the same time their masses are increased (Maeder & Behrend, 2002; Bonnell & Bate, 2005). However, the formation of the hierarchical triple systems which are often observed for massive stars is probably due to so-called n-body dynamical evolution. In this process an initially wide system consisting of a high-mass and a low-mass star starts an interaction with a third massive object (which should happen primarily in small clusters of high- and intermediate stars). The binding energy of this triple system is then taken by the massive companion and the low-mass member gets kicked further out (Bate et al., 2002). Finally, Sana et al. (2012) found, that 20-30% of all O-type stars will merge with their companion.

1.3 Circumstellar Disks

Circumstellar disks are an important ingredient for the formation of stars (and furthermore also for the formation of planets). It has been mentioned before that the initial rotation of molecular clouds would hinder the cores from collapsing to stellar dimensions if the angular momentum could not be removed through various processes. Circumstellar disks can, on the one hand, be part of the solution of this problem (Lin et al., 2011). On the other hand, for the formation process of stars with higher masses circumstellar disks might help to accrete material onto the protostar and thus allow it to grow further than it would be possible in a spherical accretion process. The observation of circumstellar disks is thus essential to draw conclusions on how star formation works.

The formation of circumstellar disks is a simple consequence of the conservation of angular momentum. While some of the disk mass moves to the outer parts and takes over a large part of the angular momentum, a large part of the disk mass moves inwards and finally accretes onto the protostar. Several mechanisms for the transport of angular momentum have been discussed in the literature, and it is accepted that the viscosity of the disk plays an important role, although the processes creating this viscosity are still under debate. The most accepted mechanism for angular momentum transport is the *magnetorotational instability* (Stone & Pringle, 2001), but other mechanisms such as transport through gravitational spiral waves (Pickett et al., 2003; Rosen et al., 2012) or through global magnetic fields (Stehle & Spruit, 2001) are also possible scenarios.

One of the most simple pictures of the structure of a circumstellar disk is a passive flat disk irra-

diated by a star. In such a picture, most of the radiation is absorbed and reemitted at small disk radii, which leads to large near-IR and small far-IR fluxes. SEDs of stars surrounded by flat circumstellar disks would thus show a relatively steep slope ($\nu F_\nu \propto \nu^{4/3}$), which is not observed for most sources. A natural explanation for the strong far-IR flux would be a flaring disk geometry (Kenyon & Hartmann, 1987) as a consequence of vertical hydrostatic equilibrium. Other possibilities to explain the large amount of far-IR flux are active disks, i.e., disks not only heated by the central star but self-heated, or the presence of an additional dusty envelope.

Flaring disk models (Chiang & Goldreich, 1997) are quite successful in reproducing the overall shape of the SEDs of young stars surrounded by circumstellar disks in the mid- and far-IR. The mid-IR emission features can easily be explained by emission from the dusty surface of such a disk. The dust grains in the optically thin disk atmosphere are directly irradiated by the stellar radiation. This leads to a temperature increase of a factor of two to four in contrast to the grain temperature deeper inside the disk. However, the so-called *near-infrared bump* observed in the spectra of a large number of Herbig Ae stars (Hillenbrand et al., 1992) can not be explained by this very simple models.

To solve this problem, Natta et al. (2001) suggested that truncated disks (i.e., disks with an inner hole) could produce such a bump at the inner rim. Dullemond et al. (2001) and Dullemond & Dominik (2004) investigated and refined this possibility and introduced the picture of a *puffed-up inner rim*. The idea behind this is, that the inner rim is much hotter than a disk without hole at the same radius and will thus also have a larger scale height. Such a puffed-up inner rim will, depending on its height and the flaring of the disk, lead to a shadow on parts of the disk or even to a shadowing of the whole disk. The inner rim radius of the dusty disk is equivalent to the *dust sublimation/condensation radius*. Monnier et al. (2005) confirmed the simple relation between size of the near-IR emission region and the stellar luminosity $R \propto L^{1/2}$. A sketch from Dullemond et al. (2007) of how a flaring circumstellar disk is structured can be found in Fig. 1.3.

However, for some YSOs, especially for luminous Herbig Be stars, deviations from this simple relation were found: the derived sizes of these objects are considerably smaller than the dust sublimation radius expected from the stellar parameters. This implies that a significant fraction of the infrared emission comes from regions closer to the star than the dust sublimation radius. Several possible explanations are currently discussed.

One of the most promising possibilities is emission from hot gas in the inner regions of the accretion disk, inside the dust sublimation radius (Benisty et al., 2011; Kraus et al., 2008b). Alternatively, the emission may come from dust that can survive very close to the star because it is shielded from the direct stellar light by optically thick gas (Monnier et al., 2005). As another explanation, Benisty et al. (2010a) suggested that the compact emission may perhaps come from refractory iron grains that can withstand temperatures considerably above the usually assumed dust sublimation temperature of 1500 K. A further possibility would be that the structure of the inner dust rim is more complex than usually expected, because large ($> 1\,\mu$m) dust grains survive considerably (around two times) closer to the star than smaller dust grains, what may perhaps explain the small observed sizes of the NIR emission regions. Finally, Pinte et al. (2008) and Benisty et al. (2010b) suggested that scattered stellar light may also play a role for the derived interferometric size estimates.

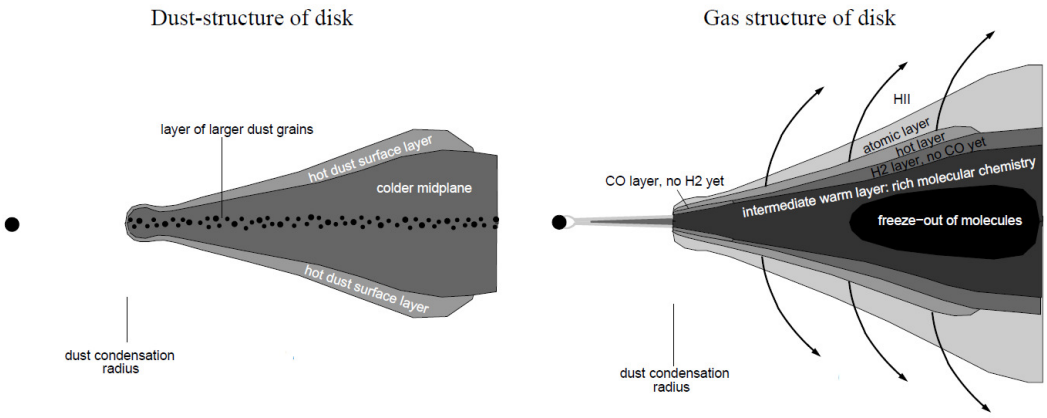

Figure 1.3: Sketch of the structure of a flaring protoplanetary disk in dust (left) and gas (right) from Dullemond et al. (2007).

Chapter 2

Interferometry

2.1 Basics of Interferometry

This chapter gives a basic overview of the ideas and principles of interferometric observations, which are necessary to be known to understand how interferometry is applied to astronomical observations. Complete reviews and mathematical derivations of interferometric principles can be found in various publications. Much of the content of this chapter follows Monnier (2003), Ratzka (2005), and Glindemann (2011), where more detailed information can be found.

The reason for using interferometric techniques in astronomy is the limited spatial resolution of classical single dish telescopes. The spatial resolution A of a single dish telescope is given by the Rayleigh criterion:

$$A = 1.22\lambda/D, \tag{2.1}$$

where λ is the observation wavelength and D is the diameter of a circular aperture. This is valid for the ideal, diffraction limited case, i.e., perfect telescope optics and no atmospheric effects. The Rayleigh-criterion can be derived in the following way: The response of the telescope to a point-like source (called *point-spread function, PSF*) describes the shape of the intensity distribution in the focal plane. In the case of a circular aperture (i.e., a circular telescope mirror) this intensity distribution is called *Airy disk* (Born & Wolf, 1980). The Rayleigh criterion is then defined as the angular distance between the peak of the Airy disk and its first minimum (which yields formula 2.1). Another possibility to define the resolution is the diameter of the Airy disk at half of the maximum intensity, the so-called *full width at half maximum, (FWHM)*, which yields approximately:

$$\mathrm{FWHM} = \lambda/\mathrm{D}. \tag{2.2}$$

Hence, the bigger the diameter of the telescope is, the better is its resolution. However, due to stability and costs, it is not possible to build mirrors for fully movable telescopes with diameters bigger than $\sim$ 100 m, even if composing them from a number of smaller mirrors as done for, e.g., big radio telescopes or the Extremely Large Telescope (ELT), which is currently under construction. A similar resolution criterion can be found for an interferometer (defining the resolution as the inverse of the highest spatial frequency):

$$\mathrm{FWHM} = \lambda/\mathrm{B} \tag{2.3}$$

Here, the spatial resolution of an interferometer depends on the distance (or baseline B) of the telescopes. Using different baselines it is thus possible to gain information about the object on different spatial scales (for a single aperture information on all spatial scales between 0 and D is provided).

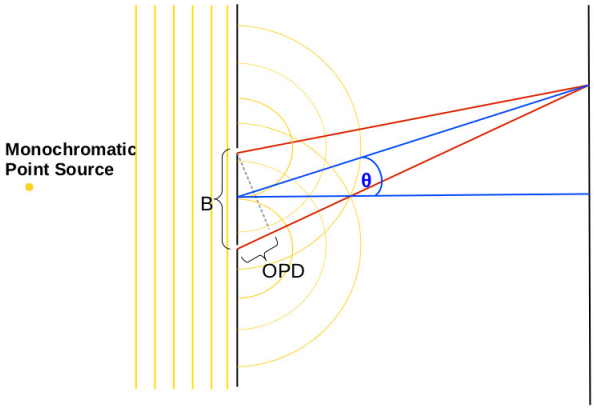

Figure 2.1: Scheme of Young's double-slit experiment. B denotes the distance of the two slits (or two telescopes).

2.1.1 Young's Experiment

Historically, the first step towards optical interferometry is probably the famous "double-slit experiment" of Thomas Young (Young, 1802). In this experiment (shown schematically in Fig. 2.1) two pinholes separated by a distance B are illuminated by a monochromatic source (with the wavelength λ) located at such a great distance, that the incoming light can be treated as a plane wave. The light passing through the pinholes is diffracted and (in case the two pinholes are small enough) can be assumed to originate from each pinhole as a spherical wave. The two spherical waves can now interfere with each other, causing an interference pattern on a screen located at a distance d behind the pinholes. The phase difference of the two waves arriving at the screen is depending on the *optical path difference, (OPD)*, the difference of the length of the two paths the light has to travel: $\mathrm{OPD} = \mathrm{B} \cdot \Theta$. Thus, the OPD depends on the distance of the two pinholes and the angle Θ, which depends on the location on the screen. If the OPD is an integer multiple of λ, the light is interfering constructively (i.e., the intensity, $I = |\vec{E}^2 = \vec{E} \cdot \vec{E}^*$, is doubled), if the OPD is half of an integer multiple of the wavelength, the light is interfering destructively (i.e., the intensity becomes zero). The distribution of the intensity pattern as a function of the location on the screen (i.e., as function of Θ) can be derived very easily considering the amplitudes of spherical waves (see e.g., Glindemann 2011):

$$I(\Theta) \propto (1 + \cos(k\Theta B),$$

with $k = 2\pi/\lambda$ being the wave number. Another name for the intensity distribution is *fringe pattern*. The *fringe visibility* V is defined as the contrast between the fringes (Michelson, 1920):

$$V = \frac{I_{\max} - I_{\min}}{I_{\max} + I_{\min}} \tag{2.4}$$

In the case of monochromatic point sources (as discussed until now) the intensities of the fringes oscillate between 0 and 1, thus, $I_{\max} = 1$ and $I_{\min} = 0$, which yields $V = 1$.

2.1.2 Mathematical Description of an Interferogram

A basic scheme of a two telescope interferometer is shown in Fig. 2.2. Comparing Fig. 2.2 and Fig. 2.1 it becomes clear, that the two pinholes from the double-slit experiment have been replaced by the two

telescopes. Furthermore, instead of directly interfering the light on a screen, the beams are guided to an interferometric instrument, which combines the beams (see Sects. 2.2.2, 2.3.2, and 2.3.3). The way from the telescope T1 to the beam combiner can be varied by a delay line (red).

An interferogram of a monochromatic point source observed with two telescopes can be described mathematically in a simple way, very similar to the description of the interference pattern in the double-slit experiment. The mathematical derivation given here follows essentially that of Lawson (2000). The two telescopes T1 and T2 located at the positions $\vec{x_1}$ and $\vec{x_2}$ are separated by the baseline vector $\vec{B}$ (thus, $\vec{B} = \vec{x_2} - \vec{x_1}$). The observed monochromatic object is located in such a great distance of the telescopes, that the incoming light can be described by a plane wave with wavelength λ (which is true for all astronomical objects). Following Jackson (1962), the electric field vector of a plane wave is

$$\vec{E}(\vec{x}, t) = \vec{E_0} \cdot \exp\left(i(\vec{k}\vec{x} - \omega t)\right),$$

where $|\vec{k}| = 2\pi/\lambda$ and $\omega = kc$ is the angular frequency. The path difference between the light arriving at T1 and T2 depends on the separation of the telescopes, i.e., the baseline $\vec{B}$ and the position of the source in the sky, i.e., the angle α (see Fig. 2.2). The planar waves arriving at the two telescopes T1 and T2 can thus be described by:

$$\vec{E_1} = \vec{E_{1,0}} \cdot \exp\left(i(\vec{k}\vec{x_1} - \omega t)\right),$$

and

$$\vec{E_2} = \vec{E_{2,0}} \cdot \exp\left(i(\vec{k}\vec{x_2} - \omega t)\right) = E_{2,0} \cdot \exp\left(i(\vec{k}\vec{x_1} + \vec{k}\vec{B} - \omega t)\right).$$

For the time averaged signal on the detector one then gets:

$$\begin{aligned} I &= |\vec{E_1} + \vec{E_2}|^2 \\ &= |\vec{E_{1,0}}| \cdot \exp\left(i(\vec{k}\vec{x_1} - \omega t)\right) \cdot |\vec{E_{1,0}}| \cdot \exp\left(-i(\vec{k}\vec{x_1} - \omega t)\right) \\ &+ |\vec{E_{1,0}}| \cdot \exp\left(i(\vec{k}\vec{x_1} - \omega t)\right) \cdot |\vec{E_{2,0}}| \cdot \exp\left(-i(\vec{k}\vec{x_1} - \omega t + \vec{k}\vec{B})\right) \\ &+ |\vec{E_{1,0}}| \cdot \exp\left(-i(\vec{k}\vec{x_1} - \omega t)\right) \cdot |\vec{E_{2,0}}| \cdot \exp\left(i(\vec{k}\vec{x_1} - \omega t + \vec{k}\vec{B})\right) \\ &+ |\vec{E_{2,0}}| \cdot \exp\left(i(\vec{k}\vec{x_1} - \omega t + \vec{k}\vec{B})\right) \cdot |\vec{E_{2,0}}| \cdot \exp\left(-i(\vec{k}\vec{x_1} - \omega t + \vec{k}\vec{B})\right). \end{aligned} \tag{2.5}$$

This yields:

$$I = {E_{1,0}}^2 + |\vec{E_{1,0}}| \cdot |\vec{E_{2,0}}| \cdot \exp\left(-i\vec{k}\vec{B}\right) + |\vec{E_{1,0}}| \cdot |\vec{E_{2,0}}| \cdot \exp\left(i\vec{k}\vec{B}\right) + {E_{2,0}}^2 \tag{2.6}$$

and with $\cos(z) = \frac{1}{2}\left(\exp(iz) + \exp(-iz)\right)$ and ${E_{1,0}}^2 = I_1$ and ${E_{2,0}}^2 = I_2$ one gets:

$$I = I_1 + I_2 + 2\sqrt{I_1}\sqrt{I_2}\cos\left(\vec{k}\vec{B}\right).$$

As mentioned above, one of the paths from the telescope to the detector can be varied, introducing an additional phase $\delta(t)$.

$$I = I_1 + I_2 + 2\sqrt{I_1}\sqrt{I_2}\cos\left(\vec{k}\vec{B} + \delta(t)\right). \tag{2.7}$$

In the case of two equally bright beams ($I_1 = I_2$) the total intensity varies between $2I_1$ and 0 depending on $\delta(t)$ (or, respectively, on the length of the additional path). If the additional path is equal to the OPD (or $\delta(t) = \mathrm{OPD} \pm \mathrm{n} \cdot \lambda$, $n \epsilon \mathbb{N}$) the beams are interfering constructively and the signal is doubled, in case the path is equal $\delta(t) = \mathrm{OPD} \pm \mathrm{n} \cdot \lambda/2$ ($n \epsilon \mathbb{N}$) the interference is destructive and no signal is detected. Furthermore, the path difference is not only depending on the separation of the two telescopes, but also on the actual position on the detector.

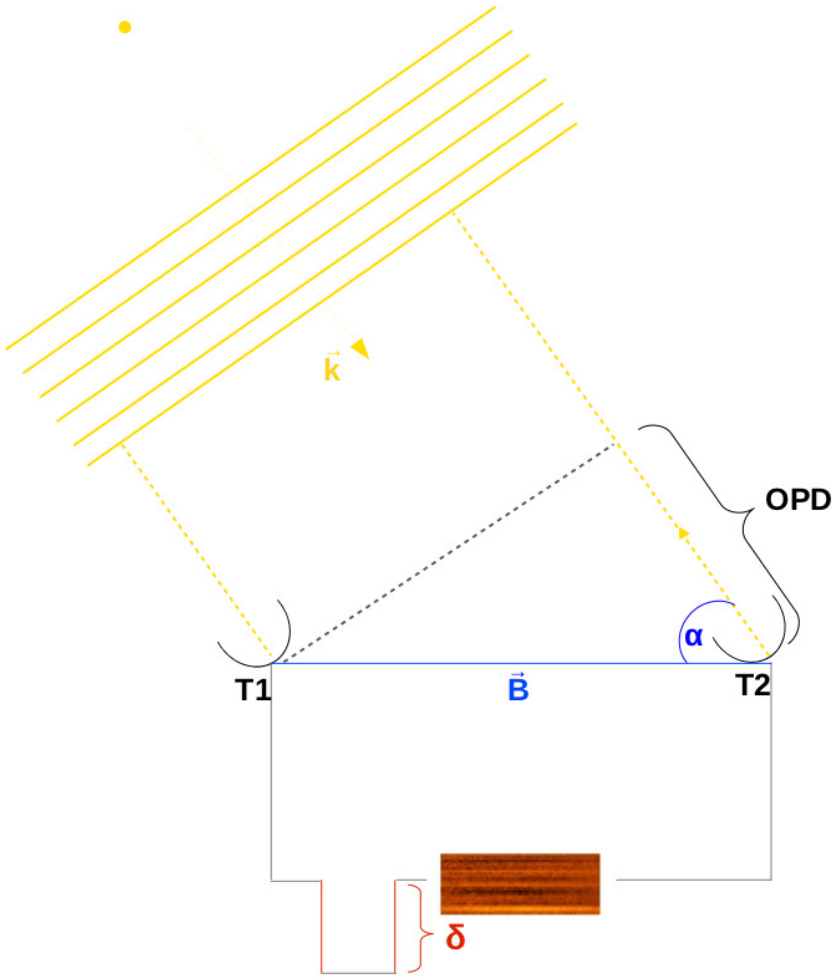

Figure 2.2: Scheme of a 2 telescope interferometer. $\vec{B}$ is the distance between the two telescopes T1 and T2, 2δ is the delay introduced between the two telescopes to account for the optical path difference between the incoming light between the two telescopes. The light from the two telescopes is then combined and a fringe pattern can be measured.

2.1.3 The Van Cittert-Zernike Theorem

The relation between the brightness distribution and the *complex visibility* (or spatial coherence function) of an object is described by the *Van Cittert-Zernike Theorem*:

$$V(u,v) = \int_{-\infty}^{\infty}\int_{-\infty}^{\infty} I(x,y)\cdot e^{-ik(ux+vy)}\frac{dxdy}{\sqrt{1-x^2-y^2}}, \tag{2.8}$$

where x and y are the coordinates on the sky. The coordinates u and v are the two components of the baseline projected on the sky. They are also called *spatial frequencies*, i.e., they are the length of the baseline measured in units of the observation wavelength ($u = B_u/\lambda$ and $v = B_v/\lambda$). The fringe visibility defined in Sect. 2.1.1 is directly related to the complex visibility, as it measures the amplitude of the complex visibility. The other part of the complex visibility, the fringe phase, can also be directly observed: It is defined as the location of the central fringe relative to the position of zero OPD. For the derivation and discussion of the theorem see, e.g., Thompson et al. (2001). Theoretically, knowing the complex visibility for all points in the *uv-plane* (i.e., the Fourier-plane), one can fully reconstruct the brightness distribution of an object by a simple Fourier-transformation (i.e., the image of the observed object can be reconstructed).

In practice, the number of uv-points is limited (due to the limited number of telescopes and the limited amount of observing time). However, if the number of uv-points is large enough (as a rule of thumb the number of visibilities and phases should be at least equal to the number of filled pixels in the reconstructed image), it is still possible to reconstruct an image (also called *synthesis imaging* or *aperture synthesis*).

Obviously, the quality of the reconstructed image depends on the number and distribution of data points in the uv-plane. The number of uv-points scales with the number of (different) baselines, which scales with the number of telescopes as follows:

$$N_B = \frac{N_T\cdot(N_T-1)}{2}.$$

Thus, adding just a few telescopes increases the number of uv-points significantly (e.g., two telescopes have only one baseline, three telescopes have three baselines, and four telescopes have already six different baselines) and allows an image reconstruction of much better quality. As the number of telescopes is limited in practice, strategies on how to efficiently fill the uv-plane with a sufficient number of measurements, even with a rather low number of telescopes, have to be developed. One important strategy for the observations is to use the rotation of the earth, which can cause (depending on the position of the object in the sky) the projected baselines (and position angles) to change significantly over several hours. Combining observations over several hours to fill the uv-plane is called *earth rotation synthesis* (see Fig. 2.3).

Using only a limited number of uv-points, the Fourier transform of the sampled visibilities is called *dirty map*. It has to be corrected with regard to the sampling of the uv-plane. Several algorithms for aperture synthesis have been developed for radio interferometric observations over the last decades, thus details can be found in a large number of publications (e.g., Thompson et al. 2001, Taylor et al. 1999, Glindemann 2011). One of the most successful methods is the CLEAN algorithm presented in Högbom (1974). CLEAN is an iterative process performing a deconvolution of the dirty map with the interferometer PSF.

In the case of an insufficient number of uv-points for image reconstruction, another possibility to obtain spatial information about the observed object is to fit model parameters to the measured visibilities. Possibilities of how to construct such models are discussed in Sect. 2.4.1.

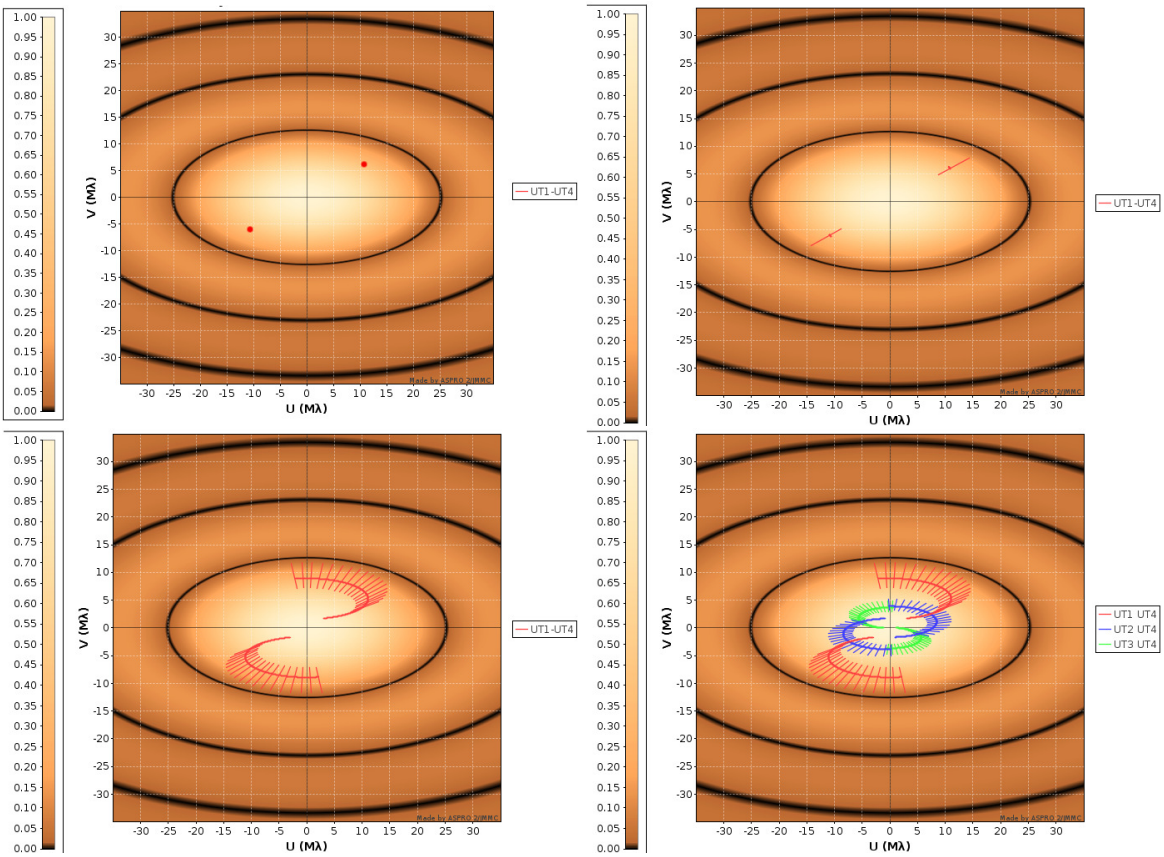

Figure 2.3: In this sequence of pictures it is shown how spectrally resolved visibility measurements and the rotation of the earth can help to get a better coverage of the uv-plane and thus more information on the object. The object model is an inclined uniform disk. The amplitude of the visibility is converted using a linear scale, where black regions belong to a visibility value of 0.0 and white regions to a visibility of 1.0. In this example MIDI (see Sect. 2.3.2) and the UTs (see Sect. 2.3.1) were chosen as instrumental setup. In the first picture (upper left) only one baseline is used for an observation. From such a measurement, we get only a uv-coverage of the two red points shown. In the next picture (upper right), the spectral resolution and bandwidth is taken into account. Thus, for one measurement using one baseline we do not anymore just get a point in the uv-plane but rather a line. The lower left picture shows the effect of earth rotation. The red curves show the tracks of the baseline. As before, spectrally dispersed visibilities are obtained which leads to the lines. Their separation depends on the time needed between two measurements (in this case we assumed one measurement every 30 minutes, which would be a realistic value for MIDI). Finally, we can increase the uv-coverage by adding more (different) baselines, what is shown in the lower right picture. This pictures were made using the Jean-Marie Mariotti Center `Aspro` service (available at http://www.jmmc.fr/aspro).

2.2 Interferometry in practice

This chapter deals with the practical issues of interferometric observations. For ground-based interferometry, one of the most important effects is the influence of the earth's atmosphere, which will be discussed in Sect. 2.2.1. Furthermore, there are different types of interferometers and different possible beam combination methods, of which the (for this thesis) most important ones are shortly discussed in Sect. 2.2.2. In Sect. 2.1.2 only the case of a monochromatic point source located at a great distance to the telescopes was discussed. While for astronomical objects the assumption of a great enough distance is generally valid, they are not monochromatic light sources. Furthermore, rather than observing astronomical objects which are unresolved by the interferometer, i.e., which are point sources, it is the goal of interferometry to resolve the object and constrain its geometry. Thus, the effects of polychromatic and extended sources are discussed in Sect. 2.2.3.

2.2.1 The Atmosphere

Observations performed with ground-based telescopes suffer from the influence of the earth's atmosphere. Effects of the atmosphere are emission and absorption of radiation at specific wavelengths and, what shall be discussed in this section, perturbations of the light from astronomical objects due to turbulence. This effect, also known as seeing, is recognized by everybody who takes a look in the night sky once: the stars seem to twinkle, which is caused by random focusing effects of the turbulent atmosphere. A detailed description of the atmospheric turbulence and their impact on ground based observations is given in, e.g., Glindemann (2011).

The earth's atmosphere can be considered as consisting of a large number of turbulence cells. The size of a turbulence cell is between a few hundred (in the free atmosphere) or ten meters (close to the ground) down to the order of a few millimeters, where the large cells are composed of a number of smaller cells. The cells, which have different temperatures and densities, scatter the light and induce random intensity and phase variations. Kolmogorov (1941, 1991) developed a relatively simple model, assuming that the kinetic energy from the largest turbulence cells is transferred successively to the smaller cells. Furthermore, the motion of the turbulence cells is assumed to be statistically stationary and isotropic, such that the higher order statistical moments are only depending on the distance between two points inside the cell. The so-called *Kolmogorov power spectrum* gets a very simple relation:

$$E(\vec{k}) = |\vec{k}|^{-11/3},$$

where $\vec{k}$ is the three-dimensional spatial wave vector and $E(\vec{k})$ is the kinetic energy.

The scattering of the light depends on the refractive index (which depends on the temperature and density in the turbulence cell). The refractive index also follows the Kolmogorov statistics (Glindemann, 2011) and is given by the equation:

$$\Phi(k) = 0.033\, C_n^2\, |k|^{-11/3},$$

where C_n^2 is the structure constant and characterizes the strength of the fluctuations.

The atmosphere can be described as a composition of many thin layers, each of them fulfilling the thin layer approximation (Roddier, 1981), i.e., each thin layer is assumed to be small enough to neglect diffraction effects within itself. Furthermore, all layers are unabsorbing and their properties depend only on their altitude h. This implies that the structure constant C_n^2 only depends on h. The spatial coherence length r_0 (called *Fried parameter*), the length over which an incoming wave is not

disturbed (i.e., the size of a turbulence cell), is then defined as (Fried, 1965):

$$r_0 := \left[0.423\left(\frac{2\pi}{\lambda}\right)^2 (\cos\zeta)^{-1} \int C_n^2(h)dh\right]^{-3/5}, \tag{2.9}$$

where ζ is the zenith distance and the number 0.423 scales the Fried parameter in such a way that the mean-square phase variation over an aperture with diameter r_0 is about 1 rad^2. This means that a telescope with a diameter larger than r_0 is seeing-limited. As can be seen in formula 2.9 r_0 is depending on the wavelength:

$$r_0 \propto \lambda^{6/5}.$$

In the K-band r_0 is typically 60 cm, in the visual it can reach values up to ~ 20 cm.

The coherence time of the atmosphere τ_0 can then be defined by the crossing time of a coherence cell, which depends on the size of the coherence cell (i.e., r_0) and the effective wind speed v:

$$\tau_0 \propto \frac{r_0}{v}.$$

The turbulence in the earth's atmosphere causes distortions in the planar wave arriving from the astronomical object, such as tip and tilt of the wavefront, spherical aberration, defocusing, and a general shift of the wavefront in total (also known as *atmospheric piston*). The earth atmosphere thus introduces an additional unknown phase to the signal, such that the phase information of the object gets lost. This is a problem especially for image reconstruction. In Fig. 2.4 an example of how important the phase information is shown. The two images on the top were Fourier-transformed, then the phase information was exchanged and the images were reconstructed. Looking at the two reconstructed images at the bottom of Fig. 2.4 it becomes clear that the phase carries most of the small scale image information. However, it should be mentioned that although this example is good to recognize the importance of the phase information, for astronomical objects (having simpler brightness distributions) the difference in the reconstructed images would not be that large, so that we can already learn a lot looking only at the amplitude of the complex visibility.

However, for image reconstruction there are two ways to handle the problem of the unknown phase information. The atmospheric disturbances cancel out when adding the phases in a closed triangle telescope configuration. The quantity which is received by adding the three single phases is called *closure phase* (Jennison, 1958) and is invariant to phase perturbations introduced by the atmosphere. The second possibility is to observe a reference object with a known phase simultaneously to the science target. In this way, also called *phase referencing*, the atmospheric phase can be determined from the reference object.

2.2.2 Beam Combination

Combining the beams from two or more telescopes can be done in different ways. In general, interferometers are divided into two classes: *Michelson interferometers* and *Fizeau interferometers*. Fizeau interferometers combine the beams in the image plane (therefore also called image-plane interferometers). The imaging process is equivalent to that of a large telescope with an aperture mask. The holes in the mask correspond to the sizes and positions of the single telescopes in the interferometer. The interferometer array is mapped to the exit pupil with a fixed demagnification factor. In practice, it is difficult to build a Fizeau interferometer (on the earth) as due to the earths rotation the projected baselines vary constantly. Thus, the spacing of the fringes is variable, which causes significant technical problems.

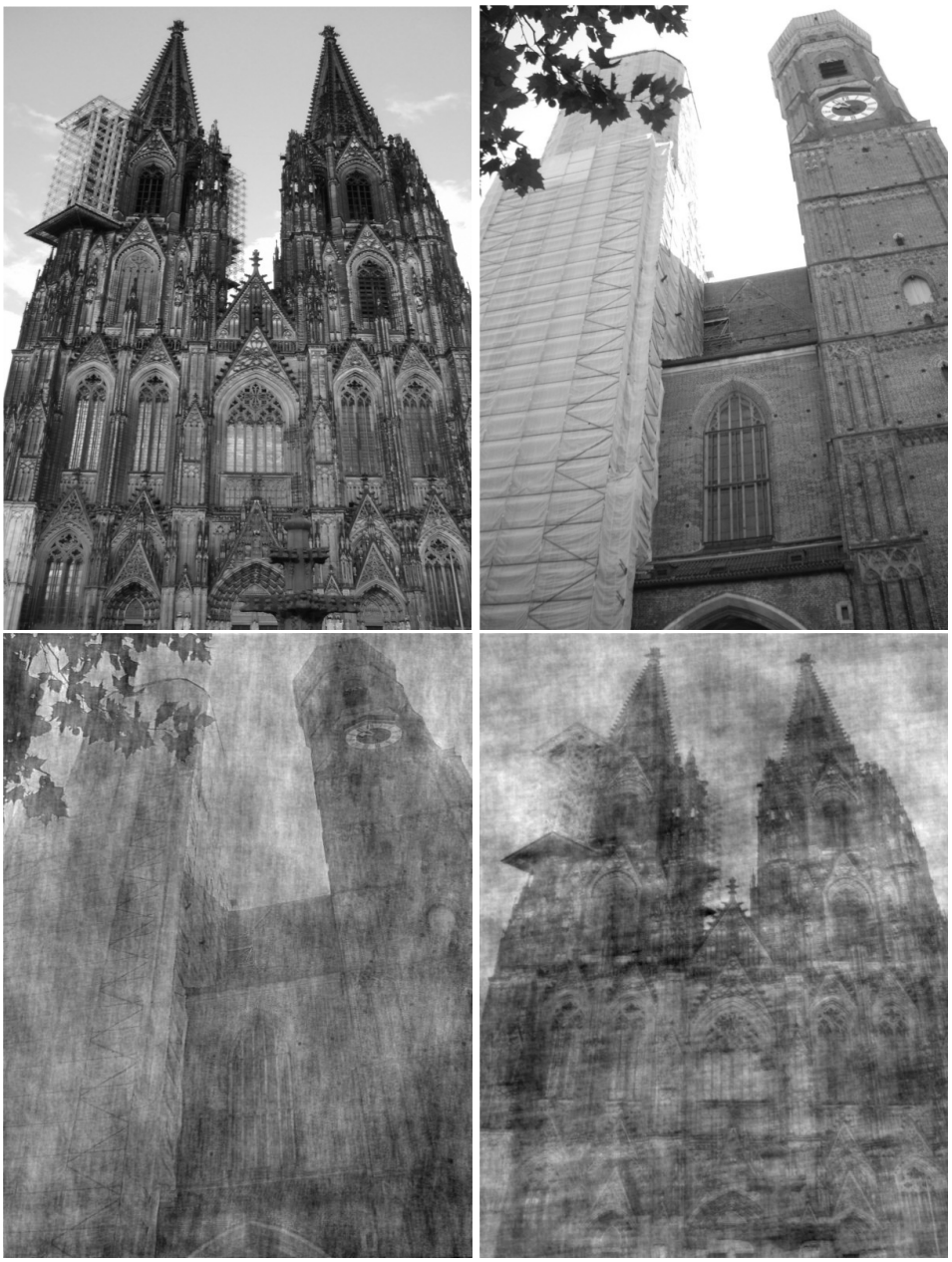

Figure 2.4: The importance of the phase information can easily be recognized by looking at this figure. The two lower images were produced by Fourier-transforming the two upper images, exchanging the phase information between them, and finally make an inverse Fourier-transformation. The picture with the same amplitude information, but different phase information are shown below the originals. Clearly, the transformed images look similar to the original image the phase information comes from.

Michelson interferometers combine the incoming beams in the pupil plane (therefore also-called pupil-plane interferometers) using a beamsplitter or fiber optics. The scheme of a 2 telescope interferometer in Fig. 2.2 shows the basic principle of a Michelson interferometer. In contrast to the Fizeau interferometer the baselines are not necessarily projected to the exit pupil in scale. The Michelson configuration thus allows a separate determination of the visibility for each telescope pair, i.e., for each baseline (even in the case of redundant baselines). The beam combination can either be done pairwise (in which case the visibility determination for each baseline is straightforward) or all-in-one (in which case the fringe coding can either be done temporally or spatially). The interferometric instruments used for the data collection in this thesis are both Michelson-type interferometers. To combine the light coherently two different methods can be used: the co-axial and the multi-axial beam combination.

Co-axial Beam Combination

The co-axial beam combination is done by aligning, combining and then focusing the beams on the detector. To obtain a fringe pattern, the delay between the incoming beams is modulated by varying the OPD between each telescope pair. In the case of co-axial beam combination the fringes are thus coded temporally. Examples for the use of co-axial beam combination are the Michelson-Morley interferometer and MIDI (see Sect. 2.3.2).

Multi-axial Beam Combination

The multi-axial beam combination is done by placing the exit pupils at varying distances to each other and combine the beams using, e.g., a lens. The fringe pattern is spread over many pixels of the detector thereby introducing geometric path difference. The fringes are thus coded spatially. Examples for the use of multi-axial beam combination are the double slit experiment and AMBER (see Sect. 2.3.3).

2.2.3 Visibilities of polychromatic and extended Sources

Obviously, real astronomical objects do not emit only monochromatic light, but light is emitted over a large range of wavelengths. The range of observed wavelengths is limited by the atmosphere (see Sect. 2.3) and instrumental filters. Considering polychromatic objects (with a finite bandwidth) can simply be done by describing the object as an addition of monochromatic objects emitting at different wavelengths. The position of the maxima and minima in the interference pattern depends on the wavelength, but at the position of zero OPD all wavelengths have an intensity maximum. This is the so-called *white-light fringe*. The resulting fringe pattern (for three monochromatic point sources) is shown in Fig. 2.5. The contrast of the resulting polychromatic fringe pattern (black) is reduced depending on the OPD (or the diffraction angle α, respectively) and depending on the spectral bandwidth $\Delta\nu$. As the OPD is related to a difference in the arriving time τ, one can say that the resulting fringe contrast is reduced with increasing τ. Thus, the τ at which the fringe contrast is lost can be defined as coherence time. It is proportional to $1/\Delta\nu$, i.e., the broader the spectral band the shorter is the coherence time.

The assumption of being point-sources made in Sect. 2.1.2 is obviously also not valid for astronomical sources, as most of them are extended. Even stars, since they are thermal sources, radiate from every point on their surfaces independently. Therefore, not only the temporal coherence of the signal is important for the fringe contrast, but also the spatial coherence, which is depending on the on the angular size of the observed object.

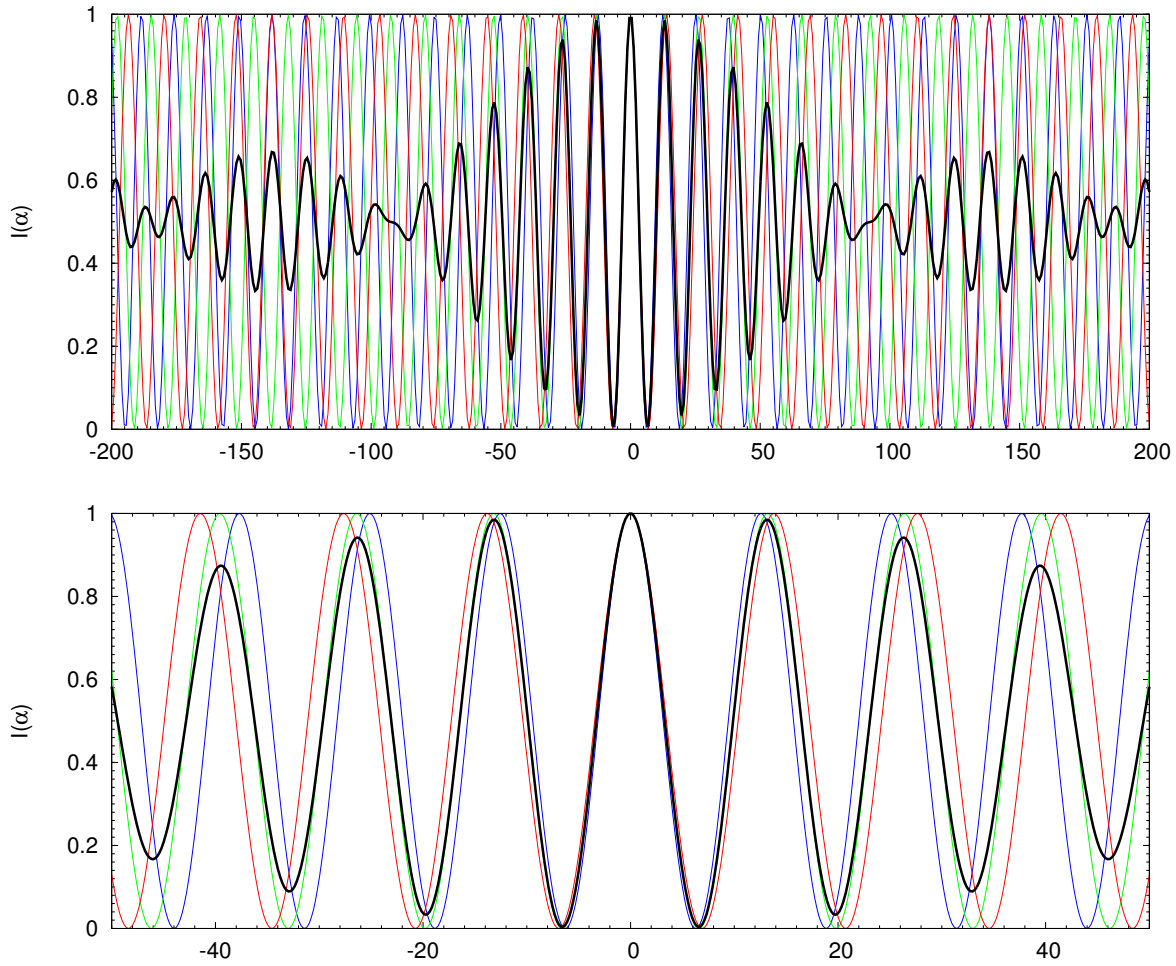

Figure 2.5: *Top:* Fringe patterns for three individual monochromatic sources (blue, green, red) and resulting fringe pattern for a polychromatic source (adding the three monochromatic intensity distributions). *Bottom:* Zoom-in of the left Figure

2.3 Optical very long baseline interferometry

In the context of interferometry, optical interferometry is not restricted to the part of the electromagnetic spectrum, which is visible for our eyes (i.e., $\sim 400 - 800\,\mathrm{nm}$), but extends to the infrared. The reason for calling it optical interferometry is rather the way of processing the light, i.e., using optics (in contrast to radio interferometry). By definition, the infrared is divided into the near-infrared ($\sim 0.8\,\mu\mathrm{m}$ to $\sim 4\,\mu\mathrm{m}$), the mid-infrared ($\sim 4\,\mu\mathrm{m}$ to $\sim 40\,\mu\mathrm{m}$), and the far-infrared ($\sim 40\,\mu\mathrm{m}$ to $\sim 500\,\mu\mathrm{m}$).

However, observing in the infrared comes along with several difficulties: First, the earth's atmosphere is not completely transparent in the infrared regime. Different molecules absorb large fractions of the infrared radiation; some prominent lines are due to e.g., H_2O at $\sim 1.8\,\mu\mathrm{m}$ and $\sim 2.7\,\mu\mathrm{m}$, O_3 between $9.3\,\mu\mathrm{m}$ and $9.8\,\mu\mathrm{m}$, or CO_2 at $\sim 4.7\,\mu\mathrm{m}$ and $\sim 15.1\,\mu\mathrm{m}$. This produces so-called atmospheric windows (see Table 2.1). Fig. 2.6 displays the transmission of the earth's atmosphere in the infrared. The data (Lord, 1992) used for the plot were taken with Gemini North. Ground-based observations are therefore only possible in this relatively small atmospheric bands and under special atmospheric conditions.

Second every blackbody with a temperature T emits electromagnetic radiation according to the Planck law:

$$S_\nu(T) = \frac{2h\nu^3}{c^2}\frac{1}{\exp\left(\frac{h\nu}{kT}\right) - 1}, \tag{2.10}$$

where k is the Boltzmann and h the Planck constant. The wavelength at which most radiation is emitted depends on the temperature of the blackbody according to Wien's Law:

$$\lambda_{\max} \cdot T/[\mathrm{K}] = 2897.8\,\mu\mathrm{m}.$$

The mean temperature on the earth is $\sim 15^\circ\,\mathrm{C}$ ($\sim 288\,\mathrm{K}$), which implies $\lambda_{\max} = 10\,\mu\mathrm{m}$. Thus, the intensity of radiation emitted by, e.g., the atmosphere, the telescopes, and the electronics, peaks in the mid-infrared regime, causing a large background, which can be several orders of magnitude higher than the radiation coming from the observed sources. This requires a careful background estimation and subtraction (see Sect. 2.3.2 and 2.3.3).

Technically, optical interferometry differs from radio interferometry in two important points: First, detectors working in the optical are generally square-law devices. This means, that the amplitude or the phase of the visibility function are not measured directly, but rather the intensity of the electric field. Still, as discussed above, both amplitude and phase can be inferred from the intensity pattern on the detector. Second, due to the much smaller wavelength, it is technically not possible to record the wave signal by interfering the beams from the single telescopes subsequently, but they have to be combined directly. Thus, the possible maximum separation of the telescopes used for optical interferometry is very limited. While radio signals can be combined from telescopes located at different continents, the longest baselines in optical interferometry are a few hundred meters.

2.3.1 The Very Large Telescope Interferometer

The *Very Large Telescope Interferometer* (*VLTI*, Glindemann et al. 2001a,b) operated by the *European Organisation for Astronomical Research in the Southern Hemisphere* (ESO) is located in the Atacama desert in Chile on Cerro Paranal at a height of 2635 m and a distance of only 12 km to the Pacific Ocean. The Atacama desert is one of the driest places on earth. It is located west of the Andes, which shield the desert from rain. Winds coming from the East are therefore dry. On the West site, close to the Pacific coast, the Humboldt stream helps to create an inversion layer and thus to

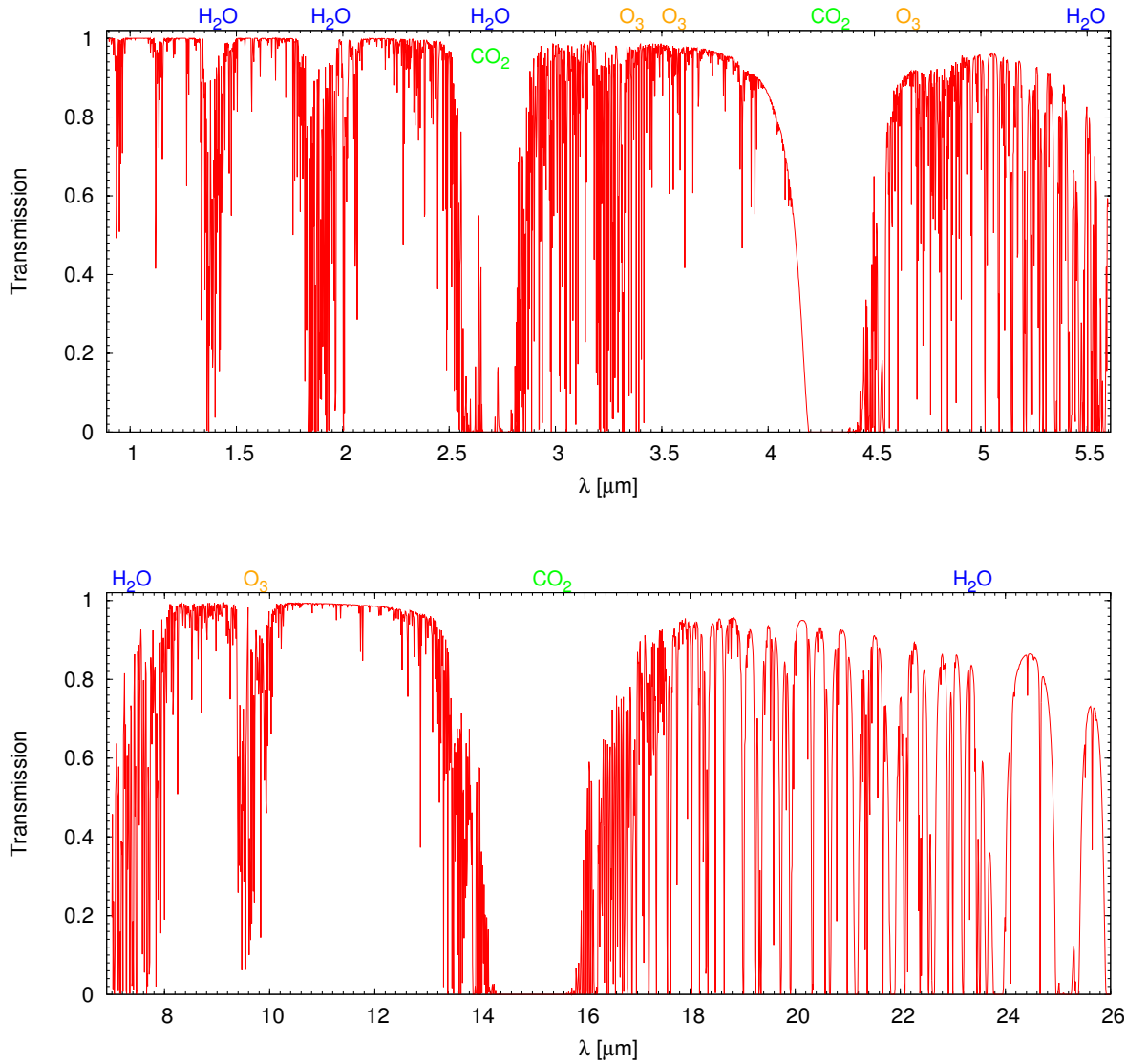

Figure 2.6: *Top:* Transmission curve of the earth atmosphere in the NIR. *Bottom:* Transmission curve of the earth atmosphere in the MIR. Curves are plotted using data (Lord, 1992) taken with Gemini North.

Table 2.1: Astronomical bands in the visual and infrared

Band		V	R	I	J	H	K	L	M	N	Q
λ_c	[μm]	0.55	0.70	0.90	1.25	1.65	2.20	3.40	5.00	12.20	21.00
$\Delta\lambda$	[μm]	0.09	0.22	0.24	0.30	0.35	0.40	0.55	0.30	5.00	8.00

λ_c is the central wavelength and $\Delta\lambda$ the width of the corresponding band. This values may vary when using different instruments and thus different filters.

hinder rain clouds from rising. Usually, the humidity at the VLTI is below 10%. As primarily water vapor is responsible for the absorption of infrared light, especially for observations in this wavelength regime a low humidity is extremely important. Furthermore, the atmospheric conditions on Paranal are relatively stable, which is especially important in interferometry considering the coherence time.

For the interferometric combination of light either the four *Unit Telescopes* (UTs) with main mirror diameters of 8.2 m or the four *Auxiliary Telescopes* (ATs) with diameters of 1.8 m can be used. The advantage of using the UTs is of course the bigger light collecting area, thus fainter sources can be observed. Furthermore, the UTs are equipped with an adaptive optics system (MACAO, Ivanescu et al. 2004), which optimizes the *Strehl ratio* (defined as the measured peak intensity over theoretical maximum peak intensity for a perfect imaging device). The ATs, on the other hand, can be moved to in total 30 different stations with baselines ranging between 8 and 202 m. Using different configurations, a better uv-coverage can be obtained. To correct for the optical path difference, the light coming from the telescopes is guided through the 168 m long delay line tunnels, which are located underneath the platform. The adjustment of the optical path difference is done by retroreflector carriages. Currently, there are three different instruments on site, performing interferometric observations: MIDI, which can combine two telescopes and works in the mid-infrared, AMBER, which can combine three telescopes and works in the near-infrared, and finally PIONIER (Berger et al., 2010), which is a visitor instrument, combining four telescopes in the near-infrared. In the following, the instruments used for the observations in this thesis, MIDI and AMBER, will be described.

2.3.2 MIDI

The *MID-infrared Interferometric instrument* (*MIDI*, Leinert et al. 2003) combines light from two telescopes in the N-band ($\sim$ 8 µm to $\sim$ 13 µm). Its design is following a co-axial beam-combination (see Sect. 2.2.2). Coming from the VLTI delay lines the two beams are compressed from a nominal diameter of 80 mm to 18 mm diameter. The compressed beams then enter small delaylines, realized by four mirrors (instrumental delay). Two of the mirrors can be moved by 100 µm each, which results in a maximal modification of the path length of 200 µm, as the beams pass the delay lines twice. Additionally, the two moveable mirrors are mounted on Piezo stages, which can be moved up to 50 mm. The rest of the instrument is located in a cryostat cooled with liquid nitrogen and helium and evacuated to 10^{-7} mbar. The beams enter the cryostat through an ZnSe window, which provides a good transmission between wavelengths of 0.63 µm and 18 µm. Next, the so-called cold pupil stop cuts the beams to a diameter of 17.7 mm and suppresses the thermal emission from outside the beams.

Located behind the cold pupil stop two parabolic mirrors build the intermediate focus by first focusing and then recolimating the beams to a diameter of 10 mm. After the intermediate focus two beamsplitters, which split $\sim$ 30% of the light directly into the photometric beams can be inserted optionally such that the photometric fluxes can be measured simultaneously to the interferometric channel. The instrument mode using the optional beamsplitters is called *SCI-PHOT mode* (science-photometry mode), the mode without the optional beamsplitters is called HIGH-SENS. In the *HIGH-SENS mode* the photometric fluxes have thus to be taken separately after the interferometric measurement. To combine the light interferometrically a ZnSe-plate covered half on one side with a 50:50 coating is used. Here, 50% of beam A and 50% of beam B are transmitted or reflected, respectively. The transmitted part of beam A is then combined with the reflected part of beam B and vice versa such that two interferometric channels with opposite phases are generated, which enables a good background subtraction (see Sect. 2.3.2). Behind the beam-combiner either a double prism made of NaCl and Ge or a KRS–5 grism (grating prism) can be inserted in the light path. The prism provides a spectral resolution of $R = \lambda/\Delta\lambda = 30$, the grism provides a spectral resolution of $R = \lambda/\Delta\lambda = 230$.

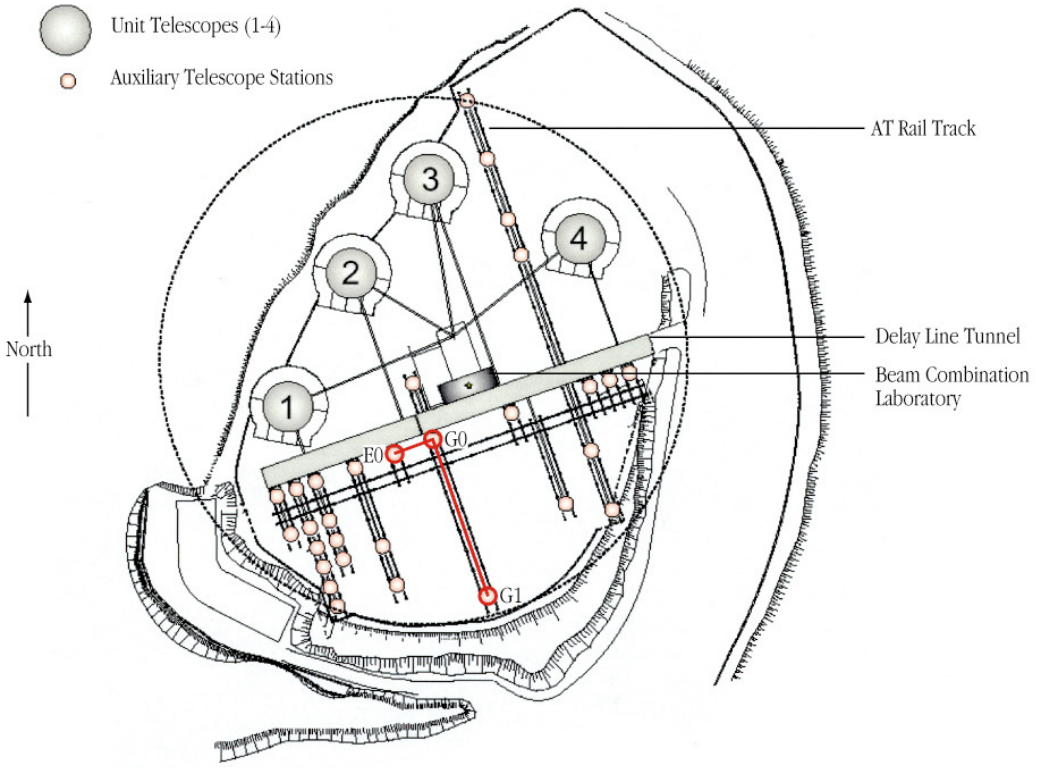

Figure 2.7: *Top:* Picture of the VLT platform with the four UTs and the four ATs. Image Courtesy: ESO *Bottom:* Scheme of the VLT platform showing the positions of the UTs (big gray circles) and all 30 thirty possible positions of the ATs (small red circles). Image Courtesy: ESO

A picture and a sketch of the instrument can be found in Fig. 2.8.

Observing with MIDI

Observing with MIDI at the VLTI requires different steps of preparation. The desired science object has to fulfill several criteria: First, its declination has of course to be such ($\delta < 25°$) that it can be observed from the location of the VLTI with an elevation $> 30°$. Second, the object has to be observable over a large enough time interval, as roughly half an hour is needed to obtain a visibility. To estimate the appropriate time intervals, besides from the declination, several factors have to be taken into account. This are the Moon, shadowing due to other telescopes, and the limitations of the delay lines. Although the Moon is generally not critical for observations in the mid-IR, it may influence the adaptive optics and should thus not be closer to the target than 10°. Observing with the ATs, the object may be hidden behind one of the much larger UTs, even if in principle it would be high enough in the sky to be observable. Finally, the delay lines can only correct for OPDs up to ~ 100 m.

Furthermore, in order to be observable, the object has to be bright enough in the N-band. Limitations of the brightness for objects which can be observed with MIDI can be found in Table 2.2. Doing interferometry, one has to consider that not the total flux of the source is the limiting factor, but the correlated flux. It is therefore necessary to make a prediction for the expected visibility. Moreover,a sufficiently bright star in the V-band is required for the telescope guiding. If the target itself is too faint in this band, another star within $57.5''$ of the science target can serve as guiding star (see Table 2.2). For the observation of, e.g., massive young stellar objects usually the N-band magnitude is sufficient for the observation, but it is difficult to find a guide star. This is due to the fact that the objects themselves are often deeply embedded and not detectable in the visual at all. Furthermore, typically the whole region is highly obscured by gas and dust, thus close stars are often also too dark in the V-band.

The measurement of one calibrated visibility takes roughly one hour including all overheads. First, *acquisition data* can be taken. Here, neither the beam-combiner nor the dispersive element are inserted into the light path. Originally, this procedure was designed to check the correct positioning of the beams on the detector. A good overlap (within one pixel accuracy) of the beams is very important, as otherwise the light can not interfere. Since 2006 the acquisition procedure is usually done using the InfraRed Image Sensor (IRIS, Gitton et al. 2004). Located in the interferometry laboratory, IRIS monitors the image drift of up to 4 telescopes in J, H, or K-band for stars with a magnitude of 14 for the UTs and 10.7 for the ATs. However, (if the target is bright enough and a high number of frames is taken) the acquisition images themselves, being diffraction-limited images taken in the mid-IR, can be used for science. To minimize the background, the telescope is chopped, i.e., the secondary mirror is tilted to take alternating images of the object and the sky. An example of an acquisition image for NGC 2264 IRS 1 is shown in the right part of Fig. 2.9. The detector is only exposed a few milliseconds (detector integration time, DIT) to avoid saturation by the high thermal background (see above).

The beam-combiner (and either the prism or the grism) is then inserted and interferometric data are taken. For the interferometric data it is not necessary to obtain and subtract the background by chopping as the background is incoherent and thus cancels out during the data reduction. First, the so-called *fringe search* is started. Here, the OPD is adjusted by searching for the interferometric signal close to the expected zero OPD (over a few mm). Once the real zero OPD is found, this position is scanned several thousand times to obtain a good signal-to-noise ratio. During this observations the OPD varies due to changes of the turbulent atmosphere (in the mid-IR on timescales of 100 ms). Thus, the internal delay lines have to be adjusted by analyzing the fringe signal, which is called *fringe tracking*.

As mentioned before, photometric data can either be taken simultaneously to the interferometric

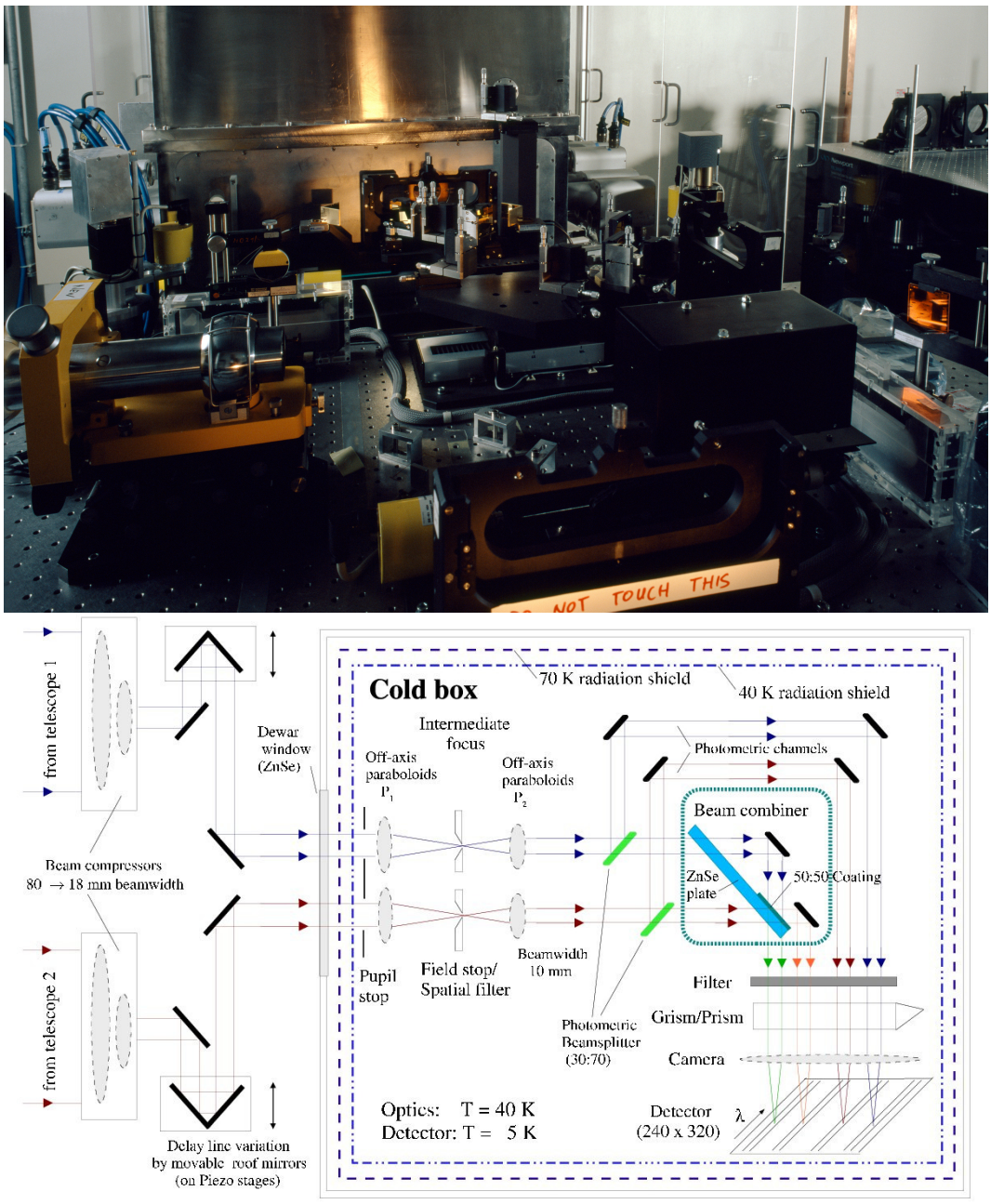

Figure 2.8: *Top:* Picture of the MIDI instrument. Image Courtesy: ESO *Bottom:* Scheme of MIDI. Image Courtesy: ESO

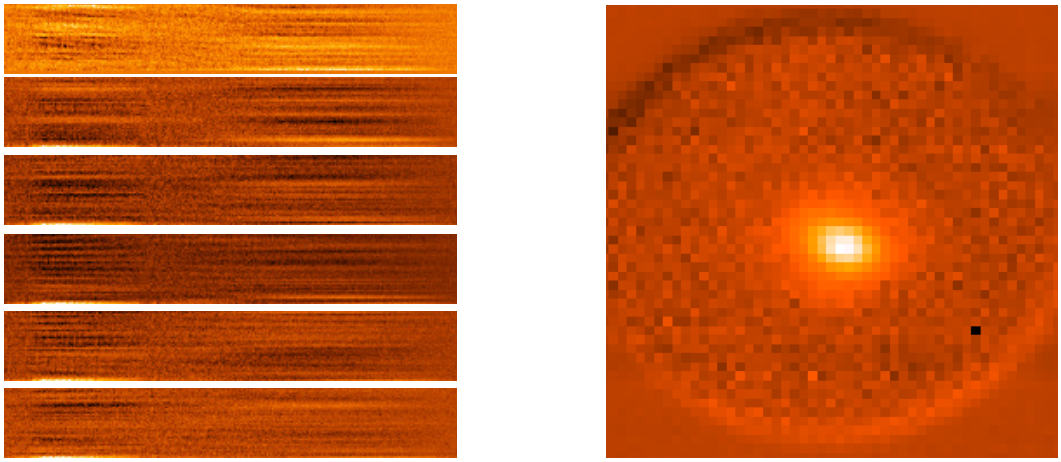

Figure 2.9: *Left:* Sample of dispersed interferograms obtained for NGC 2264 IRS 1 obtained with MIDI. *Right:* Acquisition image for NGC 2264 IRS 1 obtained with MIDI.

data (in which case chopping during the fringe tracking is necessary) or after the interferometric data (by blocking each of the telescopes once). The photometric data are then recorded for both telescopes separately, resulting in two photometric data sets. Finally, the same observations (but usually no acquisition image) have to be done for at least one calibrator star.

The above mentioned modes (Sci-Phot and High-Sens) can both be used with either the prism or the grism. This leads in particular to different limiting magnitude for the possible targets (see Table 2.2). As the intensity of the signal is splitted into more channels, using the grism requires much brighter targets than when using the prism. A better spectral resolution obviously provides more scientific information about the object, as spectral features (e.g., silicate absorption feature) can be seen in more detail. Furthermore, for bright enough targets the higher spectral resolution can lead to a better signal, as it is less polychromatic.

MIDI data reduction and calibration

For the reduction and calibration of MIDI data the software package MIA+EWS (Köhler & Jaffe, 2008) is available. Originally, it consisted of the two packages MIA, written by the MIDI group at the MPIA in Heidelberg, and EWS developed by W. Jaffe at the Observatory in Leiden. MIA (Midi Interactive Analysis) is using an incoherent method (the so-called power spectrum analysis), while EWS (Expert Work Station) uses a coherent method to obtain the amplitude of the interference pattern, which is the basic difference.

A detailed description of how the software package is working can be found in Ratzka (2005), Tristram (2007), and Chesneau (2007) and is shortly summarized in this chapter.

The first step in the data reduction process is to distinguish between the signal on the detector produced by the observed object and the background signals. Here, so-called masks are used. These provide information on which pixels the object is supposed to be and on how to weight the pixels. While EWS uses fixed (predefined) masks, MIA uses the photometric data to create masks interactively. Both approaches, fixed and interactive masks, have advantages: Fixed masks lead to a better signal to noise ratio (SNR), while interactive masks can adopt to changes in the instrument. After multiplying the signal on the detector with the masks, the data are compressed perpendicular to the

Table 2.2: Configurations of MIDI

Telescope	Mode	Resolution	N_{corr} [mag]	V [mag]	Distance $''$
UTs	High-Sens	PRISM	4.0	17	< 57.5
UTs	High-Sens	GRISM	2.8	17	< 57.5
UTs	Sci-Phot	PRISM	3.2	17	< 57.5
UTs	Sci-Phot	GRISM	2.0	17	< 57.5
ATs	High-Sens	PRISM	0.74	13.5	< 57.5
ATs	High-Sens	GRISM	0.31	13.5	< 57.5
ATs	Sci-Phot	PRISM	0.0	13.5	< 57.5
ATs	Sci-Phot	GRISM	-0.44	13.5	< 57.5

Limiting magnitudes for the MIDI instrument and the different possible configurations. N_{corr} is the minimum required correlated flux in the N band for an object to be observable with the corresponding instrument configuration. The magnitude limit for the V band is only important for the guiding of the telescopes and is thus the minimum total flux of the guiding star. The last column gives the maximum possible distance of a chosen guiding star to the science target.

spectral dispersion direction into one-dimensional arrays. As mentioned in Sect. 2.3.2, MIDI combines the light such that two interferometric signals with opposite phase are generated. To reduce the background signal (and double the object signal) these interferograms are subtracted. In EWS an additional high pass filtering is applied to remove the remaining background. The background only changes slowly in time in contrast to the rapid variation in the fringes due to the modulation of the instrumental delay.

After removing most of the background signal, the next step is to derive the interferometric observables. This is done with two completely different algorithms used by EWS and MIA:

EWS: Using the coherent data reduction the next step is to remove the instrumental OPD. Afterwards, each interferometric frame is Fourier transformed and the atmospheric delay is determined. Additionally, frames with too large OPDs or jumps in the OPD are removed. After removing the instrumental, the atmospheric delay, and a linear phase shift introduced by the varying index of refraction of water vapor the now coherent signal can be obtained by averaging the data. From the coherent signal the raw correlated flux and the differential phase are extracted.

MIA: Using the incoherent data reduction the first step is to select appropriate interferometric frames by checking the value of the Fourier amplitude of the white-light fringe. Frames which have been obtained close to zero OPD are identified and show a high amplitude, other frames are sorted out. Each frame is now Fourier transformed into the frequency space. The power spectrum is then defined as the squared absolute value of this Fourier transformation. The power spectrum shows two peaks centered asymmetrically around $\nu = 0$. The form and position of the peaks is depending on the present wavelengths and the rate at which the OPD changes. The power inside the correct frequency interval can thus be integrated and corresponds to the raw correlated flux.

As the visibility is obtained by dividing the correlated flux via the total flux, the next step is to derive the total photometric flux of the source (which also provides useful information on the observed object itself). This is done in a simultaneous way for both software packages: First, the average of the sky frames is subtracted from the average of the photometry object frames. Integrating the flux over the wavelength (the direction of the spectral dispersion on the detector) the total flux (in arbitrary detector units, ADU) can be calculated. In the case of the Sci-Phot mode there are no separate

photometric data. Thus, the photometry of the target has to be extracted from the interferometric frames. So-called κ-coefficients, which describe the relation between interferometric and photometric channels, are usually extracted from the data of one of the calibrators observed.

Finally, to derive the instrumental visibility losses and to get absolute flux values (e.g., Jansky) the science data need to be calibrated by using a calibrator star. Calibrator stars are usually well known stars with well-established flux and size. For the calibration of the MIDI data, data with the same instrumental setup (e.g., same baselines, spectral resolution) are taken and reduced.

The flux needs to be calibrated with regard to its spectral dependency. For this purpose a template spectrum (e.g., Cohen et al. 1999) of a star with similar spectral type as the calibrator star is used.

The visibility needs to be calibrated for instrumental visibility losses. Observing a point source, the visibility is expected to be equal to 1 over the whole wavelength range. The sizes of the calibrator should be $\lesssim 3$ mas to be unresolved at all wavelengths. Calibrated visibilities can then simply be obtained by dividing the visibility of the science object by the visibility of the calibrator.

2.3.3 AMBER

The *Astronomical Multi-BEam combineR* (*AMBER*, Petrov et al. 2007) was build to combine light from up to three telescopes in the J-, H-, and K-band. However, currently only the H- and K-bands are being used as the usually much lower fluxes of the objects as well as the shorter wavelength make the combination of the beams much more difficult in the J-band. Its design is following a multi-axial beam-combination (see Sect. 2.2.2). First, each beam is spatially filtered by single-mode fibers (which leads to a field of view of 65 mas for the UTs and 280 mas for the ATs). The fraction of light which enters the fiber is called the *coupling coefficient* (Shaklan & Roddier, 1988). A pair of cylindrical mirrors compresses the exiting beams into one dimensional elongated beams to minimize detector noise. Beam-splitters then separate small parts of each beam (this are the so-called *photometric channels*) which are used to derive the spectrum of the source from each telescope. The remaining part of the light is combined to form fringes (the so-called *interferometric channel*). To make the fringes from each baseline clearly distinguishable from the other ones, the three exit pupils are placed in separations of 1:2:3. The interferometric and the three photometric channels are finally spectroscopically dispersed. For this, a prism with a resolution of $R = \lambda/\Delta\lambda = 35$ can be used, the so-called *low-resolution (LR) mode*. Using a grism in the *medium-resolution (MR) mode* a resolution of $R = \lambda/\Delta\lambda = 1500$ is reached. Finally, the *high resolution (HR) mode* grism provides a spectral resolution of $R = \lambda/\Delta\lambda = 12000$. A picture and a sketch of the instrument can be found in Fig. 2.10. Besides from the already mentioned interferometric channel (IF, 32 pixels wide) and the three photometric channels (P1, P2, P3, each 32 pixels wide), a *dark channel* (DK, 20 pixels wide) is recorded. This channel contains masked pixels, i.e., it records the detector noise and the thermal background. To be able to work in the near-IR with high spectral resolution, the spectrograph has to be cooled down to about -60° C.

Observing with AMBER

As already described for the observation with MIDI (see Sect. 2.3.2) several criteria have to be fulfilled for the target to be observable (e.g., declination, distance to the moon, delay line constraints). Most of them are equally valid for the observation with AMBER, because the same telescopes and delay lines are used. The brightness limits, however, for the observation with AMBER can be found in Table 2.3. Again, the important parameter is not the total but the correlated flux of the object.

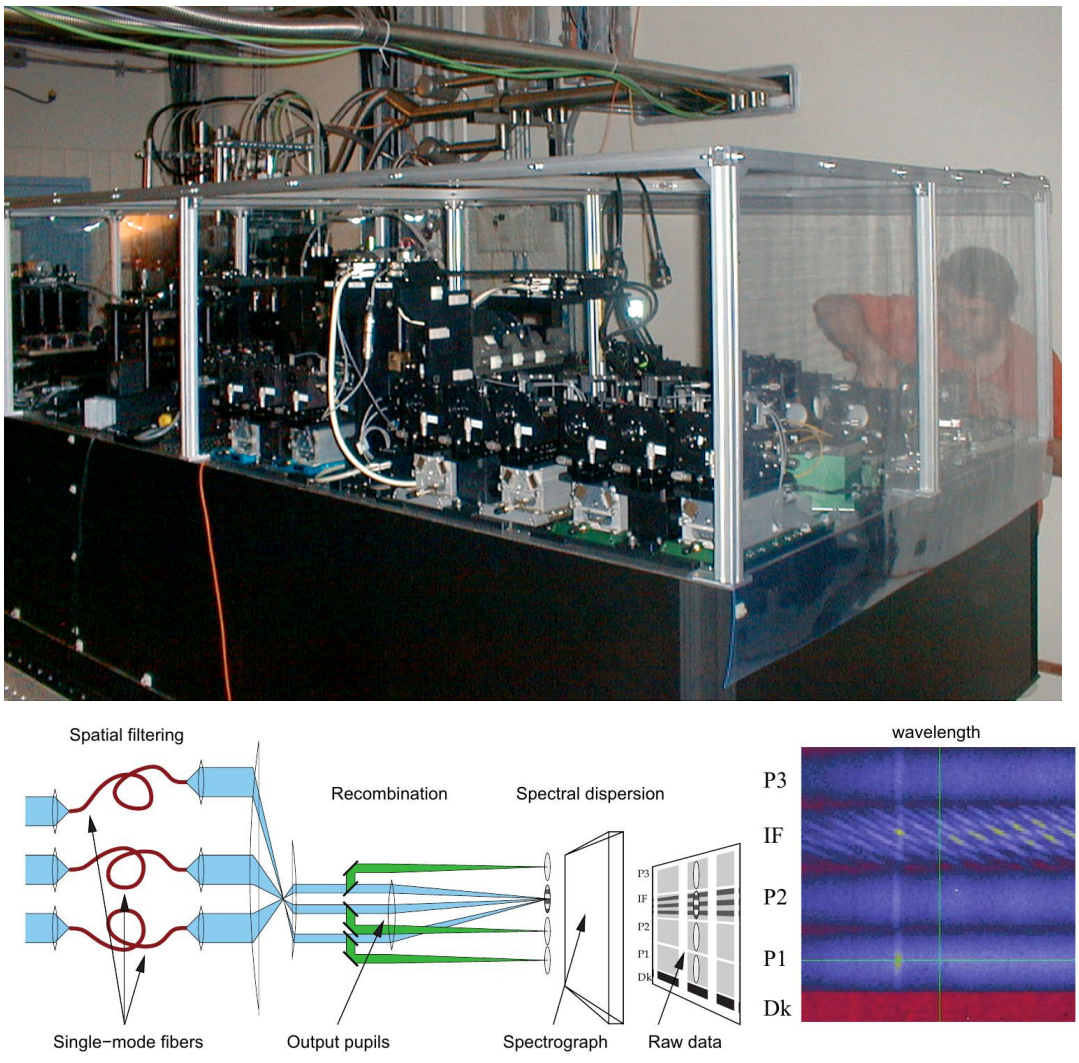

Figure 2.10: *Top:* Picture of the AMBER instrument. Image Courtesy: ESO *Bottom:* Scheme of AMBER, from Petrov et al. (2007).

The time needed for the observation of a calibrated visibility with AMBER (i.e., calibrator-science target-calibrator, CAL-SCI-CAL) depends on the spectral resolution mode and is currently 60 minutes for a standard observation in LR mode and 75 min for a standard observation in MR or HR mode. The time for one observation may, however, increase significantly. E.g., in MR and HR mode during the standard detector integration times (DIT) of 25 ms or 50 ms only a part of the spectral (H- or K-)band can be observed. The H- and K-band thus is split up in several spectral bands, with widths of 0.04 μm for MR and a DIT of 25 ms and 0.008 μm for HR and a DIT of 50 ms. If more than one channel is required, the observation time increases about 15 min per additional spectral band.

So-called *Bad Pixel Maps (BPM)* and *Flat Field Maps (FFM)* are taken by the team on Paranal whenever the instrument hardware changes and regularly about once a year. The BPM is used to mark defective pixels and exclude them from the data analysis (see next Sect.); the FFM is used for the calibration of the pixel gain. Before the observation of the targets starts, the instrument has to be calibrated for the later signal processing. This calibration procedure is done using an internal source located in the instrument. First, each beam is imaged separately by only opening the corresponding shutter. Second, an interferogram for each beam pair is recorded at zero OPD. Finally, this step is repeated close to $\lambda/2$ OPD. This calibration leads to (in case of three telescopes) nine so-called P2VM files (see next Sect.). The calibration procedure has to be redone, if the setup (e.g., spectral resolution mode) is changed. Otherwise, the P2VM is valid for 6 hrs. Then, to measure the read-out noise of the detector, *dark frames* are taken (as the name suggests, dark frames are taken without light falling onto the detector). The observation of the dark frames is repeated for every target.

As soon as the calibrations are done, the observation of the interferometric data can start. For the fringe tracking procedure, the *Fringe-tracking Instrument of NIce and TOrino* (*FINITO*, Gai et al. 2004) is usually used. FINITO works in the H-band and combines the incoming beams coaxially. It measures the relative phase difference between the incoming beams and thus identifies atmospheric effects. Located at the VLTI laboratory, it consists of several parts: the Alignment and Compensation Unit (ACU), the Fibre Modulation Unit (FMU), beam combiner, and detector. The ACU provides the longitudinal and transversal correction of the telescope beams, the FMU acts as a spatial filter. Furthermore, the FMU is used to perform a scan of the interferogram by varying the optical path length. In the end, FINITO sends a signal to the OPD controller, and thus the delay lines can be corrected to account for the relocation of the fringes due to atmospheric variations. Thus, FINITO "freezes" the location of the fringes on the detector and much longer DITs can be used.

For the calibration of the data (see next Sect.), usually two calibrators are observed for each science target, one before and one after (often the same one). For a good calibration several criteria have to be considered when choosing the calibrator objects: It should be as close as possible to the science target (to have the same atmospheric conditions), it should have a similar brightness, it should be unresolved by AMBER (i.e., have a diameter of $\lesssim$ 1 mas), and should be observable one hour before and after the science target (to make sure that the scheduling of the observation can be done in an as long as possible time slot).

AMBER data reduction and calibration

For the reduction and calibration of the AMBER data the software amdlib has been developed by the AMBER consortium[1] and is provided by the Jean-Marie-Mariotti-Center[2]. For the reduction of the AMBER data presented in this thesis, Vers. 3.0.3 (Malbet et al., 2010) was used. A detailed description of AMBER data in general and the amdlib software in particular can be found in Tatulli et al.

[1] http://amber.obs.ujf-grenoble.fr/
[2] JMMC, http://www.jmmc.fr

Table 2.3: Configurations of AMBER

Telescope	Resolution & Band	FINITO	K_{corr} [mag]	H_{corr} [mag]	Airmass	V [mag]	Distance $''$
UTs	LR (HK)	no	8.0, 7.0*	8.0, 7.0*	< 2.0	1...17	< 55
UTs	LR (HK)	group tracking	8.5, 7.5*	8.5, 7.5*	< 1.5	1...15	< 13
UTs	LR (HK)	fringe tracking	8.0, 7.0*	8.5, 7.5*	< 1.5	1...15	< 13
UTs	MR (K)	fringe tracking	8.0, 7.0*	8.5, 7.5*	< 1.5	1...15	< 13
UTs	MR (H)	fringe tracking		5.0*	< 1.5	1...15	< 13
UTs	HR (K)	fringe tracking	6.0*	6.0*	< 1.5	1...15	< 13
ATs	LR (HK)	no	< 5.5	< 5.5	< 2.0	-1.7...13.5	< 60
ATs	LR (HK)	group tracking	< 5.5	< 5.5	< 1.5	-1.7...11	< 15
ATs	LR (HK)	fringe tracking	< 5.0	< 5.0	< 1.5	-1.7...11	< 15
ATs	MR (K)	fringe tracking	< 5.0	< 5.0	< 1.5	-1.7...11	< 15
ATs	MR (H)	fringe tracking		< 4.0	< 1.5	-1.7...11	< 15
ATs	HR (K)	fringe tracking	< 5.0	< 5.0	< 1.5	-1.7...11	< 15

Limiting magnitudes for the AMBER instrument and the different possible configurations (* for seeing of $0.8''$, else for $0.6''$). K_{corr} and H_{corr} are the minimum required correlated fluxes in K and H band, respectively, for an object to be observable with the corresponding instrument setup. In the V band, the brightness limits are given for the total flux as this is only important for the selection of a guiding star. The last column gives the maximum possible distance of the guiding star to the science target.

(2007), Petrov et al. (2007), Chelli et al. (2009), and Kraus (2007), and will be shortly summarized here. The amdlib software consists of a library of C functions. For easier manipulation and production of plots, a Yorick interface is provided together with the main software routines.

The AMBER signal processing can be divided into three main parts: First, the instrument has to be calibrated such that a linear relationship between the interferogram (i.e., the pixels on the detector) and the complex visibility is given by the calibration matrix (the *Visibility-to-Pixel Matrix, V2PM*). This principle, i.e., the modeling of the interferogram in the detector plane, is similar to the ABCD method described in Colavita (1999). In the second step the calibration matrix is inverted (and becomes the *P2VM*) and used to obtain the complex visibility from the recorded interferogram. In the third and last step the interferometric observables (visibility, closure phase, and differential phase) are estimated from the complex visibility derived in step two.

In practice, before computing the P2VM from the nine (for two telescopes only four) calibration files, one has to correct for detector effects applying the BPM. After that, the pixel values have to be converted into photon counts. To remove biases and the readout noise from the signal, a number of dark frames (DARK) are taken, averaged and subtracted. As no detector is perfect, i.e., not every pixel is reacting exactly in the same way on incoming photons, a flat field map (FFM, an image of a plane, white surface) is used to account for deviations between the pixels. Another correction which has to be done before computing the P2VM is the correction of offsets in the spectral dispersion direction due to geometrical effects in the spectrograph (see below). Since version 3 of the amdlib software this correction is done automatically, as it was found (Malbet et al., 2010) that the offsets are constant as long as the cryostat is not opened and the position of the entrance slit is not changed.

Using the P2VM, the BPM, FFM, and the DARK, the raw object data (both for the science target and the calibrator) are converted into interferometric observables and stored as OI-FITS files. The

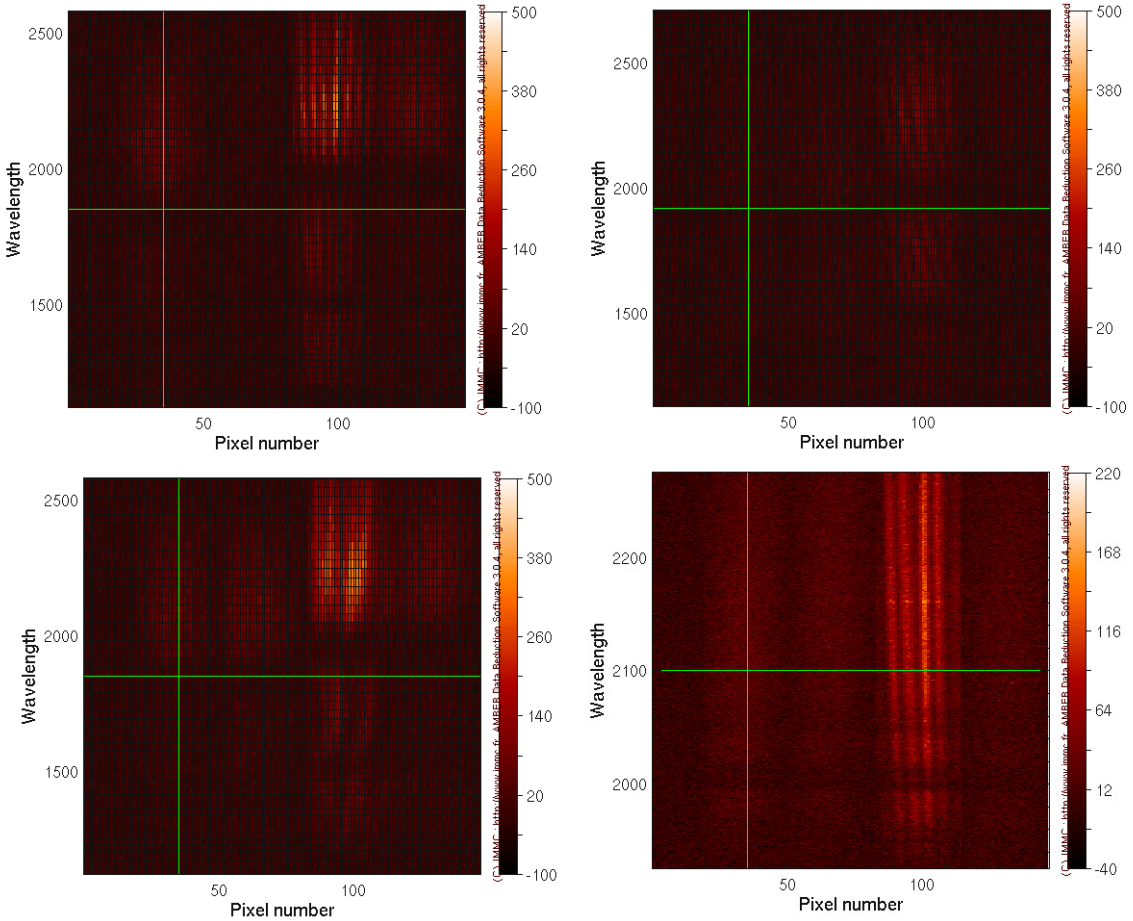

Figure 2.11: Single frames of different AMBER observing runs. *Upper left:* Good LR-HK data of θ Ori C observed on 26/12/10. *Lower left:* Bad LR-HK data of θ Ori C observed on 26/12/10. The fringes are smeared out completely. *Upper right:* Good LR-HK data of θ Ori D observed on 29/10/11. Comparing this with the data for θ Ori C the fringes are much fainter, what is due to the different K- and H-band magnitudes of the two objects. While θ Ori C has a K-band magnitude of 4.4 and an H-band magnitude of 4.5, θ Ori D has a brightness of 5.8 mag in the K-band and 5.9 mag in the H-band. *Lower right:* MR-K data of MWC 147. The Br γ line can be seen at a wavelength of ~ 2.17 µm.

next step is to select "good" frames using different selection criteria. These are: flux SNR (signal-to-noise, ratio of signal strength to background noise), piston, and fringe SNR. All three criteria can be combined or applied separately on the data. To obtain a clear interference pattern on the detector, enough photons from each telescope must reach it. Preferably, the number of photons should be roughly the same for each of the telescopes (i.e., similar brightness of the telescope beams). This requirement can be accounted for during the data reduction process by using the flux SNR criterion and choosing, e.g., only frames with SNR higher than 10. Vibrations coming from the VLTI optics (e.g., adaptive optics, delay lines) make the fringes move on the detector, thus reducing the fringe contrast (and thereby influencing the visibility). To correct for the vibrations, it is possible to select only those frames less affected by the variations using the fringe SNR selection criterion. On the other hand, choosing frames with certain fringe contrast influences the estimated visibility and can thus lead to errors in the calibrated visibilities especially if the science object and the calibrator have different magnitudes. A better way of using the fringe SNR criterion is thus to not use a threshold but rather the

best, e.g., 20 percent of frames. Correcting for the piston which tilts the fringe pattern with respect to the spectral dispersion direction, is especially important in the case of LR observations, because the piston correlates with the width of the spectral band. Obviously, if the piston is a significant fraction of the coherence length, it will reduce the fringe contrast (and thus influence the visibility).

For the wavelength calibration in LR mode the atmospheric gap between H- and K-band is used to calibrate the wavelength of the spectrum. As described in Kraus et al. (2009), the telluric features from the raw object spectrum are not pronounced enough due to instrumental absorption, thus the SKY and P2VM images can be used to correct for the instrumental absorption first. After that, the extracted spectra can be compared to standard atmospheric transmission spectra and be shifted accordingly. The remaining uncertainty is of the order of 0.03 μm. For MR and HR observations the wavelength calibration can be done using positions of known atmospheric lines.

To get absolute calibrated visibilities, one has to account for instrumental and atmospheric effects (e.g., seeing variation) by calibrating the visibilities with a star of known diameter. The brightness distribution of the calibrator is assumed to be similar to a uniform disk with the diameter of the calibrator. Then the correction for the visibility of the calibrator can be computed and the instrumental and atmospheric transfer function can be estimated. To get a transfer function for the whole night (what is needed for the estimation of the errorbars) this is done for all calibrator stars observed in the specific night. To get the transfer function at the time of the observation of the science target, the transfer function of the different calibrators have to be, e.g., interpolated. To obtain an absolute visibility for the science target, the uncalibrated visibility has to be divided by the transfer function at the time of the observation. A simplified (and incomplete) calibration can be done by just using the transfer function of one calibrator and assume that it has been constant between the observation of the calibrator and the observation of the science target.

2.4 Applications of IR-interferometry in star formation

In this section I shortly explain how interferometric studies are used to provide new insights into the star formation process. With respect to the content of Chaps. 3 to 6 I focus on the detection of companions in Sect. 2.4.1 and on observation of circumstellar disks in Sect. 2.4.2.

2.4.1 Detecting Companions

No single observational technique is able to reveal companions over the full range of possible separations. While spectroscopic studies can only find the very close companions at separations of about one AU or less, direct imaging (even with adaptive optics) can only reveal the wide companions at separations of more than tens or hundreds of AUs. Infrared long-baseline interferometry is very efficient in finding companions at angular separations between ∼2 and ∼100 mas. For distances of a few 100 pc, it is thus ideally suited to fill the observational gap between the very close spectroscopic companions and the wide visual companions, what was shown by several studies as well for MIDI as for AMBER (Ratzka et al., 2009; Kraus et al., 2009).

The Van Zittert-Cernike theorem (Sect. 2.1.3) directly relates the visibility profile to the brightness distribution of the source. For very simple geometries the visibility profile can be described by a simple formula. For a point source, which can be described mathematically by a δ-function, the Fourier-transform is a constant. Thus, the fringe visibility, i.e., the amplitude of the complex visibility, is equal to one. A binary can often be described by two δ-functions (in case the stars themselves are unresolved). Two binaries with a separation of $a = |\vec{a}|$ and a flux ratio of $f = I_1/I_2$ correspond to the

following visibility distribution:

$$V(B_\lambda) = \sqrt{\frac{1 + f^2 + 2f\cos(2\pi a B_\lambda)}{(1+f)^2}},$$

where B_λ is the baseline projected onto the separation vector $\vec{d}$ measured in units of λ. The derivation of the equation for the normalized visibilities can be found in, e.g., Berger & Segransan (2007). The amplitude of the oscillation in the visibility depends on the flux ratio of the binary and the frequency on the projected separation. Examples of how a visibility of a binary could look like are shown in Fig. 2.12, where binaries with different separation and flux ratio have been modeled. The lowermost picture shows that choosing a unfavorable baseline (length and/or position angle) the visibility curve can look like a straight line rather than oscillating, what makes the determination of the binary separation ambiguous if the flux ratio of the binary is not known from other observations.

2.4.2 Resolving Circumstellar Disks

To understand the structure and evolution of circumstellar disks and resolve the regions where planets are born, spatial information about the inner parts (from $\sim 0,1$ AU to ~ 100 AU) of the disks is needed. Modeling the SED alone can lead to highly ambiguous results (Thamm et al., 1994; Men'shchikov & Henning, 1997; Offner et al., 2012). Thus, for nearby star-forming regions the angular resolution required is on the order of some milliarcseconds (mas). Infrared interferometric long-baseline observations can not only provide the required angular resolution, but is also ideally suited with respect to the temperatures of the inner regions of circumstellar disks, which are ≥ 1500 K for the inner gas disk and several hundred to ~ 1500 K for the inner dusty part of the disk. An impression of how such a circumstellar disk could look like and which regions could be observed using infrared-interferometry is shown in Fig. 2.13. Near-infrared interferometry (e.g., AMBER) is sensitive to the innermost parts of the disk, i.e., the hot gas disk and emission originating from the inner dust rim. While the contribution of the star itself can usually be neglected in the mid-IR regime, its contribution at near-IR wavelengths may have to be taken into account. Mid-infrared interferometry is sensitive to the warmer, outer parts of the disk. However, to measure the outer radius and the total mass of circumstellar disks usually sub-mm observations have to be used.

If a star is resolved by the interferometer it can often be described as a uniform circular disk, in which case the visibility for a disk with diameter d is:

$$V(B_\lambda) = \left|\frac{2J_1(\pi d B_\lambda)}{\pi d B_\lambda}\right|,$$

where J_1 is the Bessel function of first kind and first order.

Circular symmetric structures with a non-uniform brightness distribution such as, e.g., circumstellar disks can in first approximation be described by a Gaussian disk. A Gaussian brightness distribution with a FWHM diameter d leads to a visibility

$$V(B_\lambda) = \exp\left[-\frac{(\pi d B_\lambda)^2}{4\ln 2}\right].$$

Using this simple analytical formula it is possible to estimate a size of the emitting region. The size of the emitting region of a particular object can then be compared with the Gaussian FWHM of other, similar objects or to sizes obtained for different position angles of the same object. This will provide information on the (a)symmetry, i.e., inclination of the circumstellar disk. In the most cases the

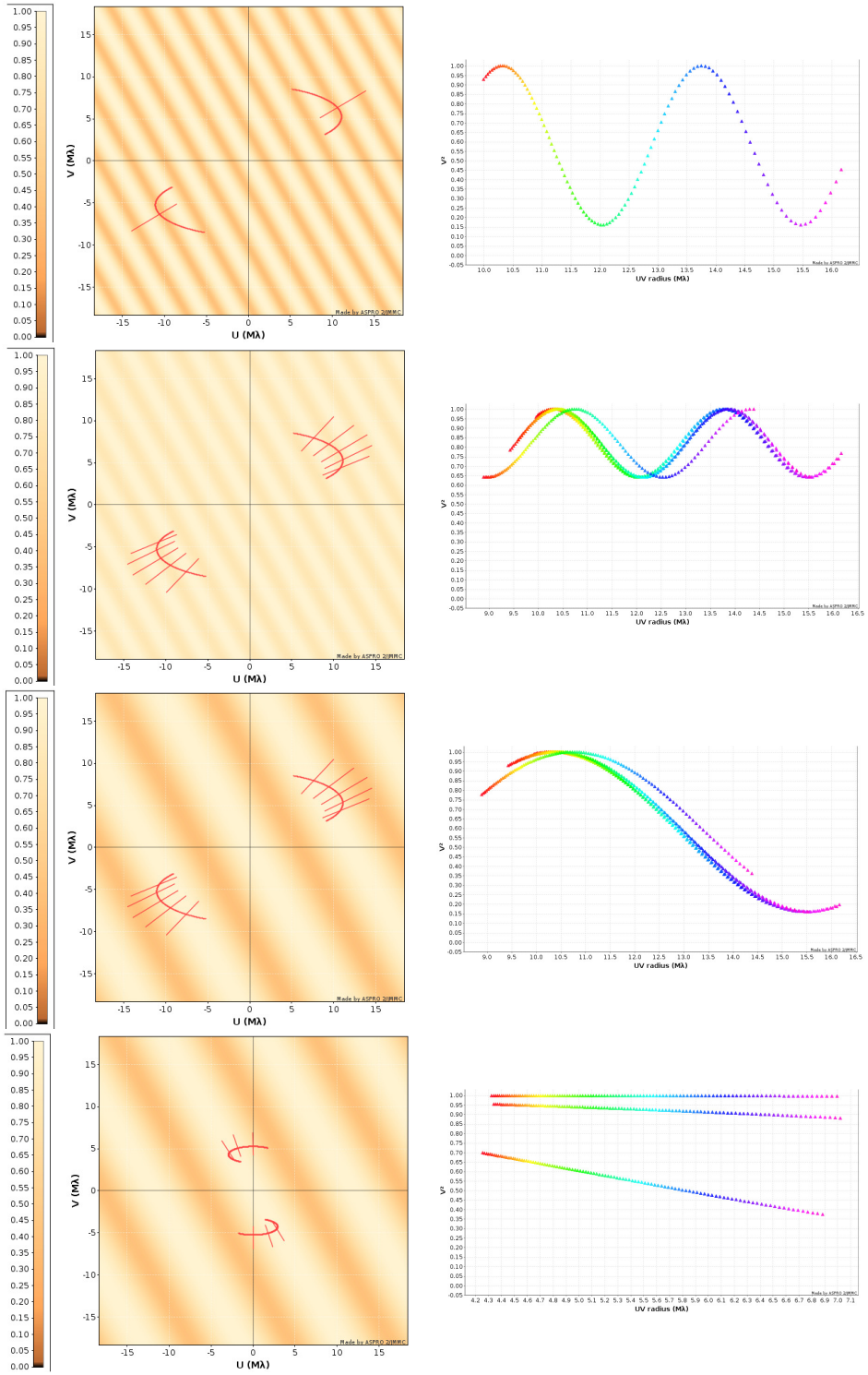

Figure 2.12: Examples of uv-coverage and expected visibility signal for different binary systems. The binary was modeled using two point sources with a certain separation and flux ratio. This pictures were made using the Jean-Marie Mariotti Center `Aspro` service (available at http://www.jmmc.fr/aspro). As for simplicity only one baseline is used in the pictures, MIDI with the grism was selected as observing instrument. The signal for the AMBER visibilities would, however, look quite similar for an appropriate close binary. In the left pictures the uv-plane is shown together with the model visibility amplitudes, the tracks of the baseline caused by earth rotation (red curve) and the measured points in the uv-plane (red line). In the uppermost picture the binary model consists of two point sources with a separation of 80 mas and a flux ratio of 1:2. The second picture shows the signal for the same binary with a flux ratio of 1:8. In the third picture the binary has a flux ratio of 1:2, but a separation of only 30 mas. In the last picture the binary has the same properties as in the third picture, but a different baseline was chosen.

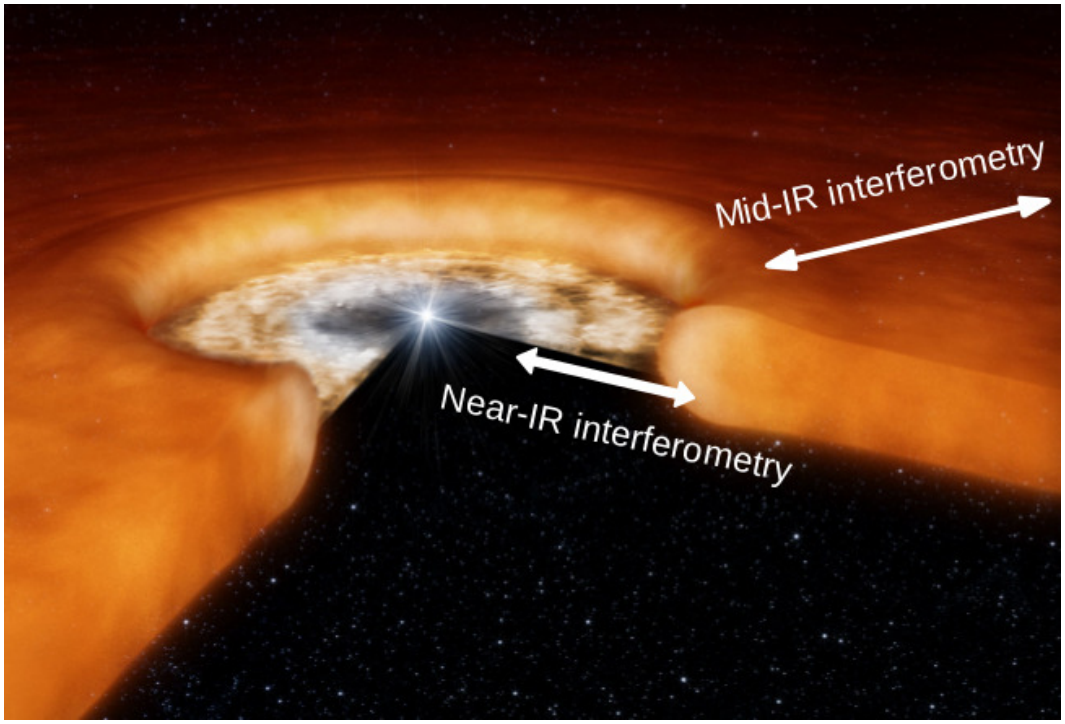

Figure 2.13: Artists impression of a circumstellar disk surrounding a YSO showing the geometry of the dusty disk in the outer areas and a hot gas disk inside the dust sublimation radius. The image is not to scale. The dust sublimation radius is usually located at $\sim$ 1 AU. The size of the whole disk can be up to $\sim$ 100 AU. While near-IR interferometry can resolve the hot inner parts of the disk and the structure of the inner dust rim, mid-IR interferometry is sensitive to the warm outer parts of the disk. Credit: ESO, L. Calcada

observed objects have, however, much more complicated brightness distributions, for which it is not possible to calculate an analytical description of the visibility. More complicated (numerical) models need then to be calculated and compared to the measured visibilities. For dust distributions around young stars, radiative transfer models are often employed.

Further possibilities to investigate circumstellar disks come from the spectral resolution of interferometric instruments. As described in Sects. 2.3.2 and 2.3.3, both, MIDI and AMBER, disperse the light spectrally. While the low-resolution modes of these two instruments already provide a resolution of $\sim$ 30, using the higher resolution modes significantly better spectral resolutions can be used. In the mid-IR regime this resolution can be used to study the silicate feature (Henning, 2010) at $\sim$ 10 µm. Using different baselines it is possible to probe the radial dust composition of the disks surface. A common result of such a study is that the silicate grains in the inner parts of the disk are larger and more crystalline than the silicate grains in the outer parts of the disk (van Boekel et al., 2004; van Boekel, 2008; Schegerer et al., 2009). In Fig. 2.14 typical silicate emission features coming from different parts of the circumstellar disk are shown.

While thus already a spatial resolution of 230 can deliver valuable information about dust grain processing and the chemical composition of circumstellar dust, the spectral capabilities of AMBER promise even more possibilities. With the highest available spectral resolution of 12,000 it is not only possible to detect spectral lines, but furthermore to investigate the structure and kinematics in the innermost disk regions, i.e., in the jet-launching and accreting regions around YSOs (Weigelt et al., 2011). The medium resolution mode of AMBER has been used, e.g., to resolve the Brackett γ line

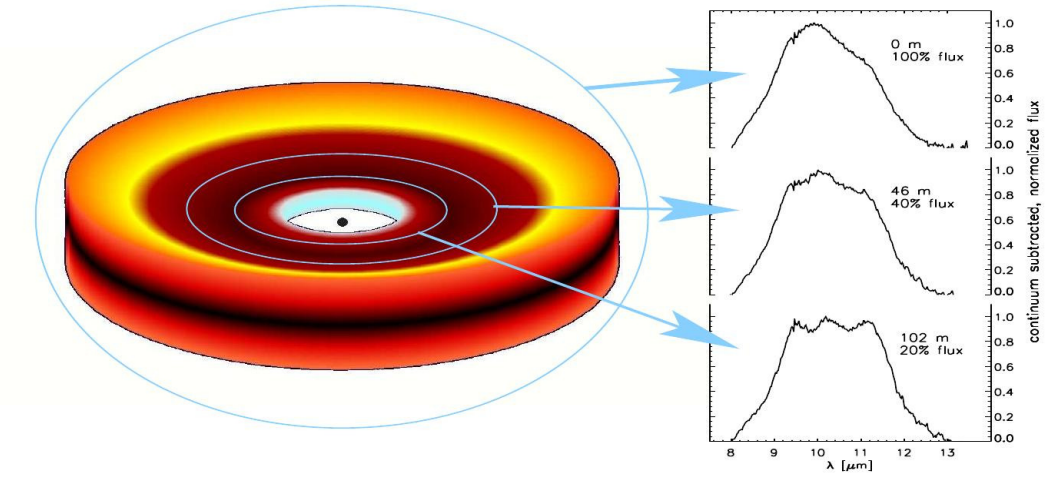

Figure 2.14: Continuum subtracted emission features of silicates of HD 144432 taken with MIDI for observations with different baselines. In the upper spectrum the total emission (i.e., as taken with the single-dish telescopes) are shown. Thus, it shows the emission coming from the whole disk. The middle spectrum was taken using a baseline of 46 m and shows the emission arising from the inner 3 AU of the disk. Finally, the correlated spectrum taken with a baseline of 102 m is shown, arising from the inner 1.5 AU of the disk. As can be seen from the comparison of the three spectra the dust composition in the disk depend strongly on the distance to the central object. From van Boekel (2008)

emission region around a small sample of Herbig AeBe stars (Malbet et al., 2007; Kraus et al., 2008a).

Table 2.4: List of accepted observing proposals

Observing Period	Proposal-ID & P.I	Description &Instrument	Time granted	Time observed
04/2010-09/2010	085.C-0260 R. Grellmann	Multiplicity in Upper Scorpius AMBER	28 hrs (SM)	9.5 hrs (SM)
10/2010-03/2011	386.C-0650 R. Grellmann	Disk around NGC 2264 IRS 1 AMBER + MIDI	1.0 nights (VM)	0.5 nights (VM)
10/2010-03/2011	386.C-0721 R. Grellmann	Jet of NGC 2264 IRS 1 AMBER + NACO	0.5 nights (VM) + 2 hrs (SM)	0.5 nights (VM) + 2 hrs (SM)
10/2010-03/2011	086.C-0156 Th. Preibisch	Spectro-interferometry of MWC 147 AMBER	11.3 hrs (SM)	3 hrs (SM)
10/2010-03/2012	086.C-0193 R. Grellmann	Multiplicity in Orion AMBER	1.5 nights (VM) + 9 hrs (SM)	0.5 nights (VM) + 4.5 hrs (SM)
10/2011-03/2012	088.D-0241 K. Helminiak	Orbit of a spectroscopic binary AMBER	6.0 nights (VM)	3.0 nights (VM)

SM: Service Mode Observations, VM: Visitor Mode Observations

Chapter 3

Mid-infrared interferometry of the massive young stellar object NGC 2264 IRS 1

Based on an article which appeared in A&A:
Grellmann, R., Ratzka, T., Kraus, S., Linz, H., Preibisch, T., Weigelt, G., A&A, 532, 109

3.1 Introduction

The question how massive stars ($> 8\,M_\odot$) form is still debated as observations of massive young stellar objects (MYSOs) are rare (Zinnecker & Yorke, 2007). This is due to several reasons: First of all, these objects are surrounded by large amounts of gas and dust, which absorb nearly all the optical and near-infrared (NIR) radiation from the central source, thus making a direct observation very difficult. Second, their large distances require a high angular resolution. Other difficulties are the fast evolution of MYSOs and the fact that they are rarely found in isolation.

Until recently, conclusions drawn on the spatial distribution of the surrounding dust were usually based mainly on the modeling of the spectral energy distribution. Such SED model fits are highly ambiguous (Thamm et al., 1994; Men'shchikov & Henning, 1997). Therefore, more information is required to obtain the real geometry of the circumstellar material. To test the existence of a circumstellar disk, and therefore the disk accretion scenario in massive star formation, information at high angular resolution (corresponding to physical scales below 100 AU) is needed. Furthermore, only radiation at long wavelengths (e.g., infrared, sub-mm) is able to escape from the dense surroundings. Infrared long-baseline interferometry can thus provide direct spatial information on the required small scales.

NGC 2264 is a young, star-forming cluster with an age of about 3 Myr located in the Mon OB 1 molecular cloud complex. Literature values for the distance of the cluster vary between 400 pc and 1000 pc, however, here we adopt the most recent value of 913 pc (Baxter et al., 2009). NGC 2264 IRS 1, the brightest IR-source in this region, was discovered in 1972 by D. Allen (therefore also called Allen's Source) and has no optical counterpart. Allen (1972) pointed out that since NGC 2264 IRS 1 is the brightest and most luminous source in this field, it is the likely source of the radiation pressure creating the Cone Nebula. It is believed to be a young star with a mass of $9.5\,M_\odot$, spectral type B0-B2 (Thompson et al., 1998), a luminosity of $3.5 \cdot 10^3\,L_\odot$ (Harvey et al., 1977), and a visual extinction

Figure 3.1: Color image (B, V, R, Hα) of NGC 2264 observed with the Wide Field Imager (Baade et al., 1999) at La Silla observatory. Credit:ESO

of 20-30 mag. However, due to its high extinction in the optical, all values are rather uncertain and should be taken with care, e.g., luminosity values between $4.7 \cdot 10^3\,L_\odot$ (Schwartz et al., 1985) and $2.3 \cdot 10^3\,L_\odot$ (Nakano et al., 2003) can be found in the literature.

NGC 2264 IRS 1 is associated with molecular outflows and dense molecular clumps, and in near-infrared images a twisted jet-like feature can be seen extending to the North of the source (Schreyer et al., 1997; Ward-Thompson et al., 2000). The morphology of the circumstellar environment is unclear. Several studies did not find a hint for an asymmetric structure. Neither Schreyer et al. (2003) could see signs of a circumstellar disk in their molecular line study, nor show the images taken in the MIR with COMICS (de Wit et al., 2009) a disk-like structure. On the other hand, models of a spherical symmetric distribution of the circumstellar material fail to reproduce the SED of the object in its entirety and were ruled out in several publications (Thompson & Tokunaga, 1978; Harvey et al., 1977). However, the spatial resolution of all these studies may not be sufficient to resolve a disk-like structure.

3.2 Observations and data reduction

NGC 2264 IRS 1 was observed on 2005 December 23 in the course of ESO observing program 076.C-0725(B) (PI: S. Kraus) and on 2009 February 15 in the course of ESO program 082.C-0899(A) (PI: M. Feldt) with MIDI at the VLTI (see Table 3.2 and Sect. 2.3.2). The 2005 data of NGC 2264 IRS 1 were taken with a baseline of 89.1 m in the SCI-PHOT mode. The grism with a spectral resolution of $\frac{\Delta\lambda}{\lambda} = 230$ was used. In the same night, two calibrators were observed with the same configuration. HD 39425 a few hours earlier and HD 61421 directly after the object. The 2009 data were taken with a baseline of 40.2 m in the HIGH-SENS mode. For this observation, the prism with a spectral

Table 3.1: Measured fluxes for NGC 2264 IRS 1

Wavelength [μm]	Flux [Jy]	Instrument/Reference	Aperture
2-45	9-670	ISO (Sloan et al. (2003))	$14'' \times 20''$
1.65	0.9 ±0.04	2-MASS	$4''$
2.2	6.8 ±0.016	2-MASS	$4''$
8-13	60-130	MIDI	$0.5''$
12.0	146 ±9	IRAS	$0.75' \times 4.5'$
24.5	330	COMICS	$42'' \times 32''$
25.0	324 ±13	IRAS	$0.75' \times 4.6'$
53.0	980 ±50	Harvey et al. (1977)	$17''$
60.0	911	IRAS	$1.5' \times 4.7'$
70.0	960 ±290	Sargent et al. (1984)	$3'$
100.0	1560	IRAS	$3' \times 5'$
100.0	1645 ±82	Harvey et al. (1977)	$28''$
175.0	1530 ±77	Harvey et al. (1977)	$46''$
350.0	188 ±70	Chini et al. (1986)	$30''$
1300	13 ±2.5	Chini et al. (1986)	$90''$

Table 3.2: Observation log of the MIDI measurements of NGC 2264 IRS 1

Date	Proj. Baseline [m]	PA [°]	Mode
12/23/2005	89.1 (UT2-UT4)	81.1	SCI-PHOT&GRISM
02/15/2009	40.2 (UT2-UT3)	43.9	HIGH-SENS&PRISM

resolution of $\frac{\Delta\lambda}{\lambda} = 30$ was used. HD 48217 and HD 49161 served as calibrators.

For data reduction and calibration, we used the software package MIA+EWS (Köhler & Jaffe, 2008). With this software, the correlated flux, visibility, and the total flux can be determined (see Sect. 2.3.2). Typical errors in one single MIDI visibility measurement are about 10% (Leinert et al., 2004). As an estimate of the error bars, the standard deviation in the results for different calibrators was used. As the conditions during the observation in 2009 were not photometric, we did not use the 2009 photometry data, but the photometry from the 2005 measurement to obtain the visibility. Figure 3.2 (left) shows the calibrated visibilities for both observations.

Furthermore, a low–resolution IR spectrum of NGC 2264 IRS 1, measured with the SWS instrument aboard the ISO satellite is available (TDT No. 71602619, PI: D. Whittet), as well as fluxes in several other wavelength bands. These data points are listed in Table 3.1. Fig. 3.2 (right) shows the total flux spectrum of NGC 2264 IRS 1 as measured by MIDI in 2005 compared to the total flux spectrum measured by the ISO satellite. Both spectra display a deep absorption feature over the whole MIDI wavelength range caused by silicates. The shape of both spectra (MIDI and ISO) is similar but the flux level of the MIDI spectrum is about 25 Jy (about 20%) lower, which might be due to the different beam sizes of the instruments (see Table 3.1). The spurious feature in the MIDI spectrum at wavelengths between 9.3 μm and 9.8 μm is due to atmospheric ozone. Several absorption features can be identified in the ISO spectrum (Gibb et al., 2004). The broad absorptions around 3.1 and 6.0 μm arise mainly from water ice, while the carrier of the 6.8 μm feature is more uncertain, but might be

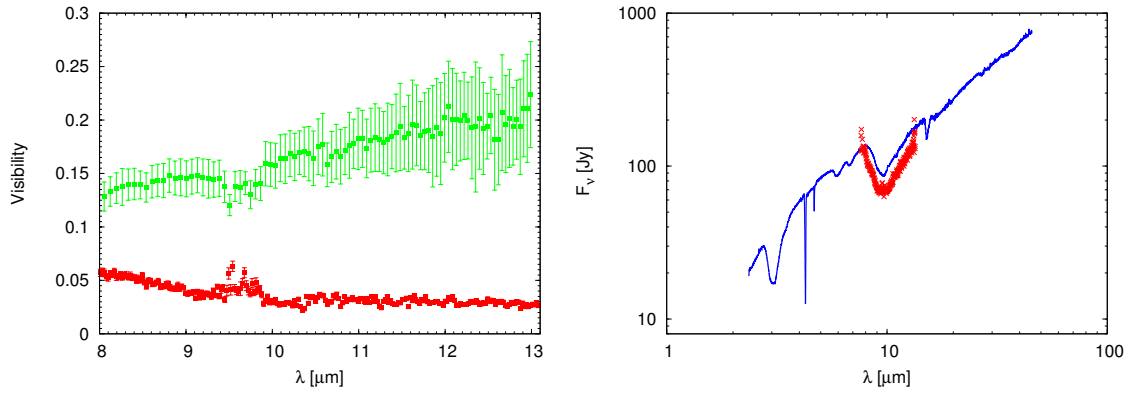

Figure 3.2: *Left:* Visibilities of NGC 2264 IRS 1 measured with MIDI. The visibility points measured in 2005 (projected baseline length 89.1 m) are shown in red, those measured in 2009 (projected baseline 40.2 m) are shown in green. *Right:* Spectrum of NGC 2264 IRS 1 as measured with MIDI (red crosses) in 2005 compared to the ISO spectrum (blue line).

associated with solid NH_4^+. A rather sharp feature at 4.27 μm is commonly attributed to CO_2 ice (Guertler et al., 1996), as is the absorption seen at 15.2 μm. The feature around 4.7 μm is probably a combination of CO gas line absorption and a variety of ice absorption features. All these findings point to relatively large column densities of cold dense material along the line of sight towards the central source.

3.3 Modeling

We now attempt to derive the properties of NGC 2264 IRS 1 from our measurements using different modeling approaches. First, we use simple geometrical models to characterize the size of the dust emission region (see Sect. 3.3.1). To test for the possibility of a circumstellar disk, we compare the data with a temperature-gradient model for such a disk (Sect. 3.3.2). To check the parameter space over a wider range, we employ the online model SED fitter by Robitaille et al. (2007) in Sect. 3.3.3. A more detailed modeling is done in Sect. 3.3.4, where the two-dimensional radiative transfer code RADMC is used.

3.3.1 Simple geometrical models

As a first step, one can derive an estimate of the diameter of the mid-infrared (MIR) emission region of the object from the visibilities by using simple geometrical models. For more details of this we refer to Berger & Segransan (2007) and Tristram (2007).

We first consider the possibility of a binary. Its existence would result in a sinusoidal variation in the visibility (versus wavelength), ranging between a maximum and a minimum value. The maximum value depends on the extension of the MIR emission regions (and would be 1 for point like sources), whereas the amplitude depends on the flux ratio of both components (the minimum would be 0 for a flux ratio of 1:1). Owing to the slit width of MIDI (see Table 3.1), the maximum separation of a binary that can be identified with this instrument is $\sim$ 230 AU. The minimum separation at which a binary could be resolved with the 90 m baseline is $\sim$ 30 AU (diffraction limit; half a period of the modulation in the visibility would be seen). Both observed visibilities show no typical sinusoidal variation, hence a binary system with a separation of $>$ 30 AU is unlikely and not considered during the modeling

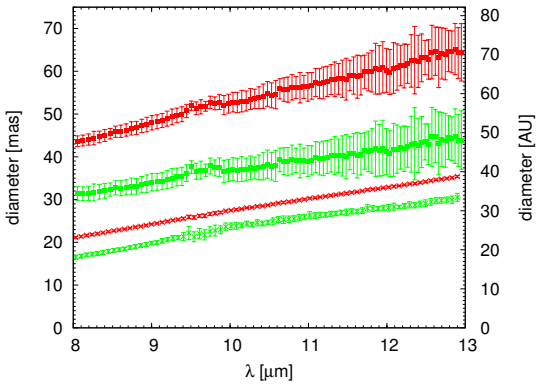

Figure 3.3: Mid-infrared diameter of NGC 2264 IRS 1 as a function of wavelength for the 2005 data (crosses) measured with a 90 m baseline and the 2009 data (rectangulars) measured with a 40 m baseline. The values for the diameter in AU (right y-axis) were computed using a distance of 913 pc. Two different models were used: a Gaussian model (green) and a uniform disk model (red).

process. However, with our measurements we could miss very faint binary companions or systems with separations of about 30 AU oriented non-parallel to the position angle of the 90 m baseline.

We consider two different geometrical models for a single source: a Gaussian distribution and a uniform disk (UD). The results can be seen in Fig. 3.3. All curves show an increasing size of the object with increasing wavelength, as expected because of the different dust temperatures in different parts of the dust distribution. For the measurement performed with the 90 m baseline, the size varies between 16 and 30 mas for the Gaussian model and between 20 and 35 mas for the uniform disk model, whereas for the 40 m baseline, the size of the object lies between 30 and 44 mas for the Gaussian model and between 44 and 64 mas for the uniform disk model. As the observations were taken at different position angles, the different size estimations suggest an elongation in the dust distribution (e.g., a circumstellar disk or a flattened envelope). Although the intensity profile of the real source possibly differs from those distributions, the Gaussian model in particular is usually a good approximation of the mid-infrared morphology of YSOs. Despite all the uncertainties in the visibility measurements, hence the size estimation, the fitting of the Gaussian model still helps us identify an asymmetry with a significance of $3\,\sigma$ and the UD model within $2\,\sigma$. This result clearly suggests that the MIR emission region is not spherically symmetric but elongated.

3.3.2 Temperature gradient model

Many young stars of both low and high mass are known to have circumstellar disks (e.g., Kraus et al., 2010; Leinert et al., 2004; Ratzka et al., 2009). As a first approach to interpreting simultaneously SED and N-band spatial data, we therefore use a temperature-gradient model for a circumstellar disk as described in Malbet et al. (2005). The disk specified by this model is optically thick, but geometrical thin with an inner radius r_{min} and an outer radius r_{max}. The distribution of the temperature in the disk is described following the equation

$$T(r) = T_0 \left(\frac{r}{r_0} \right)^{-q}, \tag{3.1}$$

where T_0 is the temperature at a reference radius $r_0 = 1\,\mathrm{AU}$. The exponent q is expected to lie approximately between 0.5 for passive, irradiated, flared disks and 0.75 for passive, irradiated, flat disks (Malbet et al., 2005).

One can imagine such a disk to be composed of rings with radius r and thickness dr. If every ring emits blackbody radiation, one can evaluate the flux by integrating over the radius r such that

$$F_\lambda(0) = \frac{2\pi}{d^2} \int_{r_{\min}}^{r_{\max}} r B_\lambda(T(r)) \cos(i) dr, \tag{3.2}$$

where d is the distance to the object, B_λ the Planck function for a blackbody with temperature $T(r)$, and i the inclination of the disk. For the visibility, one then gets

$$V_\lambda(b, 0) = \frac{2\pi}{F_\lambda(0) d^2} \int_{r_{\min}}^{r_{\max}} r B_\lambda(T(r)) J_0\left(2\pi b \frac{r}{d}\right) dr, \tag{3.3}$$

where J_0 is the Bessel function of zeroth order and b the baseline according to

$$b = \sqrt{u_\Theta^2 + v_\Theta^2 \cdot \cos^2(i)}.$$

Here, Θ is the position angle of the disk and u_Θ and v_Θ are given by

$$u_\Theta = u \cos\Theta - v \sin\Theta$$

and

$$v_\Theta = u \sin\Theta + v \cos\Theta.$$

We calculated a large number ($\approx$ 1000) of temperature-gradient models and tried to find a model that is simultaneously able to reproduce all observations (both visibilities and SED). For this, we varied the inner radius between 0.5 and 2 AU (in steps of 0.5 AU) and T_0 between 1400 and 3000 K in steps of 200 K. For the parameter q, we tested the values 0.5, 0.6, and 0.7. Inclination and position angle were varied in steps of 10°.

The temperature gradient model with the parameters listed below is able to reproduce the SED in the mid- and far-infrared, but fails in the near-infrared. All of the calculated models failed completely to reproduce the shape of the visibility measured with the 40 m baseline (rising values going to larger wavelengths). As the best-fit model, we therefore show the model that most successfully reproduces the other visibility curve and the SED simultaneously, although different models led to a better fit for the 40 m visibility at least with respect to its absolute level. The best-fit model is shown in Fig. 3.4 and has the following parameters:

- $r_{\min} = 0.5$ AU
- $r_{\max} = 4000$ AU
- $T_0 = 2350$ K
- $i = 75°$
- $q = 0.5$
- $\Theta = 90°$

The spectral features seen in the SED and the effects of the silicate absorption on the visibility cannot be reproduced, as radiative transfer effects (emission, absorption, and scattering) are not included in the model.

A temperature of $T_0 = 2350$ K at a reference radius of 1 AU would imply a temperature of 3250 K at the inner disk radius of 0.5 AU for this model. This is much too hot for the existence of normal dust grains. A possible explanation could be the existence of an inner gas disk (Kraus et al., 2008b) or of dust grains with higher sublimation temperature (Benisty et al., 2010a).

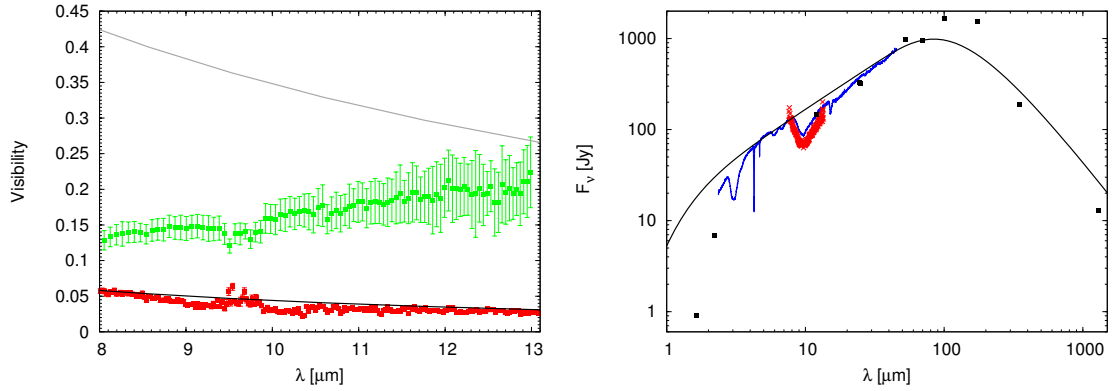

Figure 3.4: *Left:* Comparison of the best-fit temperature-gradient model to the visibilities of NGC 2264 IRS 1 with the model parameters described in Sect. 3.3.2 (green for the 40 m baseline, red for the 90 m baseline). The resulting modeled visibility for the 40 m baseline is shown by the gray line, the one for the 90 m baseline by the black line. *Right:* Comparison of the SED of our best-fit temperature-gradient model (black line) described in Sect. 3.3.2 with the ISO spectrum (blue line) of NGC 2264 IRS 1. The MIDI spectrum is shown with red crosses, all other measurements from Table 3.1 are shown with black rectangulars.

3.3.3 Disk and envelope models in the Robitaille grid

To check a wider parameter space for different models (especially for the possibility of a circumstellar envelope), we employed the online SED fitting tool developed by Robitaille et al. (2007). This tool compares 200,000 models of the SEDs of YSOs, which were precomputed using a 2D radiative transfer code (Whitney et al., 2003), with the measurements. These models are described by a set of 28 parameters, such as the properties of the central object (e.g., mass, temperature), the properties of the circumstellar envelope (e.g., outer radius, accretion rate, opening angle), the circumstellar disk (e.g., mass, outer disk radius, flaring), and the ambient density (for details see Robitaille et al., 2006). In addition to defining SED points, the user has to set a range for the interstellar extinction and for the distance of the object. We chose the interstellar extinction A_V to be between 0 and 40 mag and the distance d to be between 800 pc and 1000 pc.

The number of points that can be fitted by the SED online tool is limited. Therefore, from the ISO spectrum about one flux point per one micron was used. From the MIDI spectrum, about two flux points per micron were chosen as the shape of the spectrum changes much more in this wavelength regime because of the silicate absorption feature.

When comparing the model visibilities and fluxes to the observed data, it is important to consider the very different (effective) beam-sizes of the different observations. The MIDI instrument has an effective field-of-view of 0.5″ (slit width), corresponding to $\approx$ 450 AU at the distance of our target. The beam sizes for all other data points beyond near-infrared wavelengths are much larger: the beam size from which the ISO spectrum was extracted ($\approx$ 13 000 × 18 000 AU) is already $\approx$ 1100 times larger, and the beam sizes for all far-infrared data points are at least $\sim$ 3000 times larger than the MIDI field-of-view. The ISO and far-infrared fluxes do therefore not only trace the emission from the central YSO and its immediate circumstellar material (on spatial scales of up to $\sim$ 500 AU), but also contain contributions from the surrounding extended molecular cloud, on spatial scales of $\sim$ 20 000 AU ($\sim$ 0.1 pc).

Therefore, as a first approach we include all SED points with $\lambda > 13$ μm only as upper limits. To compute the visibilities, we used the HO-CHUNK code from Whitney et al. (2003) to calculate images

for the model. Doing so, the ten best-fit models consist of circumstellar disks only (see Sect. 3.3.3). As a second approach, none of the data points was used as an upper limit, but they all were given with their errors. Here, rather different best-fit models are found by the fitting tool. They all consist of a large circumstellar envelope and either have no additional disk, or just a small ring-like structure with radii from 0.5 to 8 AU (see Sect. 3.3.3). For similar applications of this fitting tool and its advantages and limitations in this respect, we refer to for instance Linz et al. (2009), de Wit et al. (2010), and Follert et al. (2010). We note that the parameter space is not covered uniformly. In particular, the spacing of the grid parameters is much finer in the case of low-mass YSOs than for MYSOs.

Robitaille disk models

The SED and visibilities of the best-fit Robitaille disk models are shown in Fig. 3.5. This model is able to reproduce the flux in the near- and mid-infrared. To reproduce the flux in the FIR, one would have to add for example some blackbody components as shown later for the RADMC model (see Sect.3.3.4). The model can reproduce the level of the 90 m baseline visibility, and also the 40 m baseline visibility is reproduced within the errorbars. The parameters of this best-fit model are (model ID 3004478):

- $M_{\rm star} = 11.6\,{\rm M}_\odot$
- $T_{\rm star} = 27,720\,{\rm K}$
- $L_{\rm star} = 1.21 \times 10^4\,{\rm L}_\odot$
- $r_{\rm out} = 84\,{\rm AU}$
- $h_{\rm disk}(100\,{\rm AU}) = 5.6\,{\rm AU}$
- $m_{\rm disk} = 0.09\,{\rm M}_\odot$
- $i = 70°$
- $A_V = 20.27\,{\rm mag}$
- $\Theta = 40°$

Here, $r_{\rm out}$ is the outer disk radius and $h_{\rm disk}$ would be the height of the disk when extending it to a radius of 100 AU.

Envelope plus disk models

The Robitaille envelope model with the smallest χ^2 is shown in Fig. 3.6. It fails to model especially the shape of the 40 m baseline visibility curve. The flux in the mid-IR can be reproduced, but the model cannot reproduce the flux in the near-IR. To attain the flux level in the far-IR, one would once again have to add, e.g., a blackbody component. The parameters of the best-fit model are (model ID 3019090):

- $M_{\rm star} = 8.5\,{\rm M}_\odot$
- $T_{\rm star} = 4200\,{\rm K}$
- $R_{\rm star} = 82\,{\rm R}_\odot$

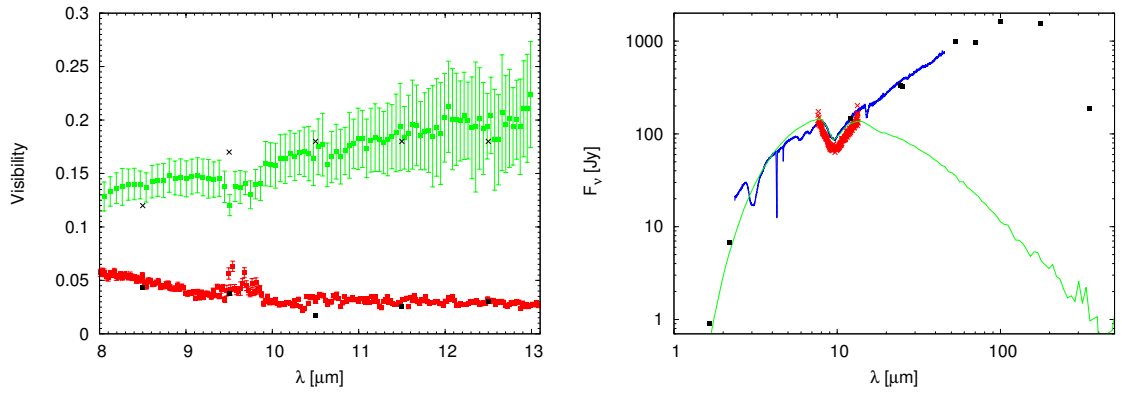

Figure 3.5: *Left:* Comparison of the best-fit Robitaille disk model (black crosses 40 m baseline, black rectangulars 90 m baseline) for the visibilities of NGC 2264 IRS 1 with the MIDI visibilities (red 90 m baseline, green 40 m baseline). *Right:* Comparison of the best-fit Robitaille model (green line) for the spectrum of NGC 2264 IRS 1 with the ISO spectrum (blue line), the MIDI spectrum (red crosses), and the data points from Table 3.1 (black rectangulars).

- $L_{\mathrm{star}} = 2.05 \times 10^3\,\mathrm{L}_\odot$
- $r_{\mathrm{envelope}} = 36{,}000\,\mathrm{AU}$
- $m_{\mathrm{envelope}} = 1.84\,\mathrm{M}_\odot$
- $r_{\mathrm{disk}} = 3.6\,\mathrm{AU}$
- $h_{\mathrm{disk}}(100\,\mathrm{AU}) = 7.7\,\mathrm{AU}$
- $m_{\mathrm{disk}} = 0.2\,\mathrm{M}_\odot$
- $i = 18°$
- $A_V = 3.8\,\mathrm{mag}$.

A change in the position angle does not in this case lead to significant differences for this model, as the dust distribution is nearly symmetric. Therefore, a best-fit position angle cannot be given. As mentioned before, this model consists mainly of a circumstellar envelope, with an outer radius of r_{envelope}. However, there is also a disk component with a very small outer radius $r_{\mathrm{disk}} = 3.6\,\mathrm{AU}$. The central object is much cooler and larger than the central object in the disk models.

3.3.4 Two-dimensional radiative transfer modeling

A more detailed physical model for a circumstellar disk is obtained by using the two-dimensional (2-D) radiative transfer model code RADMC (Version 3.1, Dullemond & Dominik, 2004), which provides calculations of continuum radiative transfer in three-dimensional axisymmetric (therefore 2-D) circumstellar dust distributions around a central illuminating star. The main radiative transfer calculations are done with a Monte Carlo algorithm. To produce spectra and images, a post-processing with a ray-tracing code is done. The disk is described using a passive irradiated flared disk based on the model of Chiang & Goldreich (1997), but the code also allows the user to insert a vertical puffed-up inner rim to produce a self-shadowed disk. The space is mapped in spherical coordinates. We therefore

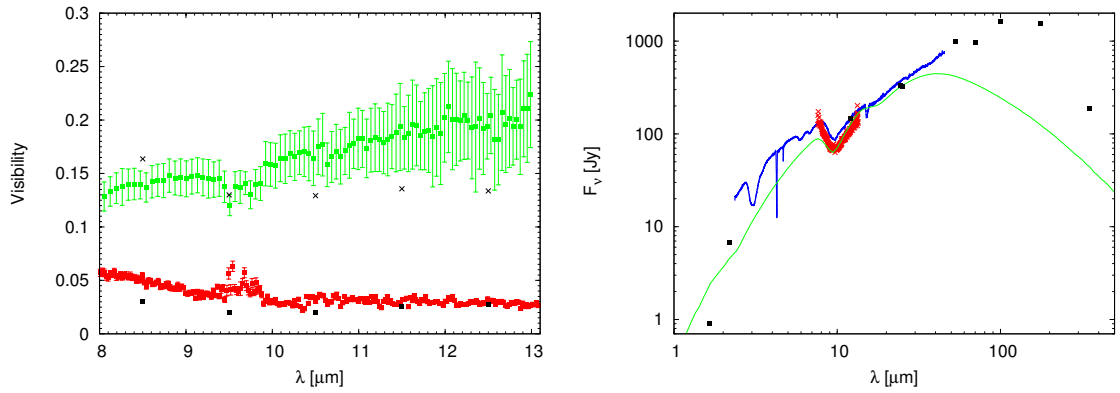

Figure 3.6: *Left:* Comparison of the best-fit Robitaille envelope model (black crosses 40 m baseline, black rectangulars 90 m baseline) for the visibilities of NGC 2264 IRS 1 with the MIDI visibilities (red 90 m baseline, green 40 m baseline). *Right:* Comparison of the best-fit Robitaille model (green line) for the spectrum of NGC 2264 IRS 1 with the ISO spectrum (blue line), the MIDI spectrum (red crosses), and the data points from Table 3.1 (black rectangulars).

have radial grid points r and angular grid points θ, where $\theta = 0$ is the polar axis and $\theta = \theta_{\max} = \frac{\pi}{2}$ is the equatorial plane. We again tried to reproduce the SED and visibilities simultaneously and also to fit the silicate absorption feature. To scan the parameter space, more than 10,000 different models were calculated and compared to the observed data.

The geometry of the disk is described by the pressure scale height $h_{\rm disk}$ at a reference radius $r_{\rm disk}$, and an exponent p in the following way (for $r_{\rm in} < r < r_{\rm disk}$):

$$h(r) = h_{\rm disk} \cdot \left(\frac{r}{r_{\rm disk}}\right)^{p}. \tag{3.4}$$

Furthermore, either the surface density at the outer radius σ_0 can be given by the user directly, or (as we did) be calculated from the user-defined total disk mass $m_{\rm disk} = m_{\rm gas} + m_{\rm dust}$. We used a gas-to-dust ratio of 100. The surface density as a function of radius is then given by

$$\sigma(r) = \sigma_0 \cdot \left(\frac{r}{r_{\rm disk}}\right)^{-q}. \tag{3.5}$$

For $r > r_{\rm disk}$, the exponent q is chosen to be equal to 12 such that the density drops so fast that $r_{\rm disk}$ is effectively the outer disk radius. This outer radius was varied between 30 AU and 150 AU. The density distribution in the whole disk is described by

$$\rho(r,\theta) \propto \frac{\sigma(r)}{h(r)\cdot r} \cdot \exp\left[-\frac{1}{2}\left(\frac{\theta_{\max}-\theta}{\mathrm{h(r)}}\right)^2\right]. \tag{3.6}$$

Parameters that remained fixed during the modeling process, were the temperature of the central object $T_{\rm star} = 25,000\,\mathrm{K}$ (according to the spectral type B0-B2), the exponent $q = 12$ for $r > r_{\rm disk}$, and the temperature at the inner rim $T_{\rm in} = 1700\,\mathrm{K}$. For the chemical composition of the dust, the optical properties of astronomical silicate (Draine & Lee, 1984) and graphite were chosen, using the grain size distribution of the MRN model (Mathis et al., 1977). A mixture of 70% silicate and 30% graphite was assumed.

In addition to the original RADMC code, we introduced foreground extinction A_V, as otherwise all models failed to reproduce the deep silicate absorption feature. Parameters that were varied during the fitting process are shown in the following list together with their values for the best-fit RADMC model:

- $r_{\rm disk} = 50\,{\rm AU}$
- $h_{\rm disk} = 0.1$
- $L_{\rm star} = 3.98 \times 10^3\,{\rm L}_\odot$
- $p = 2/7$
- $m_{\rm disk} = 0.1\,{\rm M}_\odot$
- $q = 2.5$ for $r < r_{\rm disk}$
- $i = 30°$
- PA $= 40°$
- $A_V = 27\,{\rm mag}$.

This best-fit model is shown in Fig. 3.7. It provides a good fit to the visibilities as well as the SED up to 12 μm.

The RADMC model describes the central YSO and its circumstellar matter up to the outer disk radius of 50 AU, i.e. predicts the emission in the central 100 AU diameter region. Since this area is completely inside the MIDI field-of-view, the model visibility can be directly compared to the observed visibilities. For the fits to the SED, however, we have to take into account that the very large beams of the far-infrared observations must clearly include emission from the surrounding large-scale cloud, on spatial scales of $\sim$ 20 000 AU ($\sim$ 0.1 pc) and larger, which is far outside the $r = 50\,{\rm AU}$ model area. This large-scale cloud emission should not be confused with a possible circumstellar envelope, but represents the molecular clump and the surrounding cloud in which IRS 1 is embedded (see discussion below). The mm-maps presented by Schreyer et al. (1997) show that the size of this cloud is about $1'$ (corresponding to $\sim$ 55 000 AU or $\sim$ 0.27 pc).

The effects of this large-scale cloud are as follows: our MIDI measurements are insensitive to this large-scale emission, because it is far more extended than the angular resolution (and also the field-of-view) of MIDI. Since the large-scale cloud emission is completely over-resolved for MIDI, it will not affect the observed visibilities. The observed fluxes, however, are expected to be strongly affected by the large-scale cloud. First, the cloud material in front of the embedded object IRS 1 will cause considerable extinction. This effect is represented by the foreground extinction we use in our modeling. The second effect is that the cool dust in the large-scale cloud will produce far-infrared and mm-emission. Owing to the large beam sizes of the far-infrared and mm-observations, a large fraction of the observed fluxes in these beams will result from the large-scale cloud, and not from the central embedded object IRS 1. This explains why our RADMC model fluxes at wavelengths ≥ 20 μm are considerably lower than the observed fluxes. To approximately include this large-scale cloud emission component in our model, we added to our SED model in Fig. 3.7 two additional blackbody components. For the temperature of the first component, we used $T = 55\,{\rm K}$, as determined by Schreyer et al. (1997) for the clump in which IRS 1 is embedded. For the second component, we

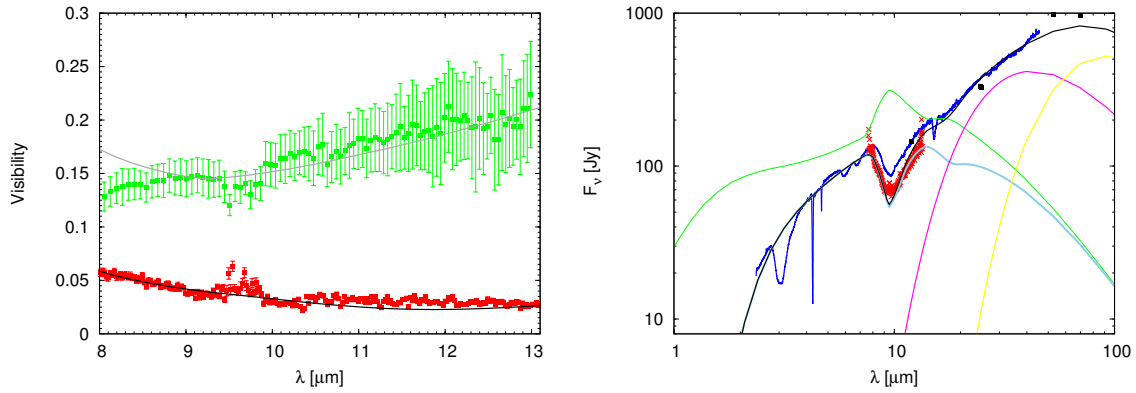

Figure 3.7: *Left:* Comparison of the best-fit RADMC model (gray line 40 m baseline, black line 90 m baseline) for the visibilities of NGC 2264 IRS 1 with the MIDI visibilities (red 90 m baseline, green 40 m baseline). *Right:* Comparison of the best-fit RADMC model for the spectrum of NGC 2264 IRS 1 with the ISO spectrum (dark blue line), the MIDI spectrum (red crosses), and the data points from Table 3.1 (black rectangulars). The green line is the RADMC model without foreground extinction, the light blue line the model with a foreground extinction of 27 mag, and the black line the RADMC model with extinction and two additional blackbody components with temperatures of 55 K (yellow line) and 120 K (pink line).

used a temperature of 120 K, which is typical of warm dust around massive YSOs in so-called "hot-cores" (Herbst & van Dishoeck, 2009). Fig 3.7 shows that with the addition of these two components good agreement between the observed fluxes and the model can be achieved.

An interesting question is whether this 120 K component could be considered as an envelope around the disk, as for one interpretation of hot cores as an infalling envelope undergoing an intense accretion phase (Osorio et al., 2009). The RADMC model of a disk without surrounding envelope provides a very good fit of both visibilities. Adding a spherical circumstellar envelope with a radius of $\leq$ 250 AU would change the model visibilities significantly (by $>$ 5%) and lead to disagreement between the model and the data. On the other hand, a (more or less) homogeneous envelope with a radius of $>$ 250 AU would be over-resolved for MIDI and not affect the visibilities. However, to reproduce the far-infrared fluxes in the SED, the radius of the 120 K emitting region has to be at least $\geq$ 400 AU (in the limiting case of optically thick blackbody emission). Owing to the limited MIDI field of view, the difference between the ISO and the MIDI spectrum could result from such an extended structure. The question of whether an extended circumstellar envelope is present can thus not be answered by the available data. Whether the material in such a hypothetical envelope would be gravitationally bound and ultimately accrete onto the circumstellar disk, remains another open question.

3.4 Discussion

We now want to discuss our findings presented in Sect. 3.3. We first compare the size of the mid-IR emission region as calculated in Sect. 3.3.1 to the corresponding sizes of similar objects. We then discuss the radiative transfer models.

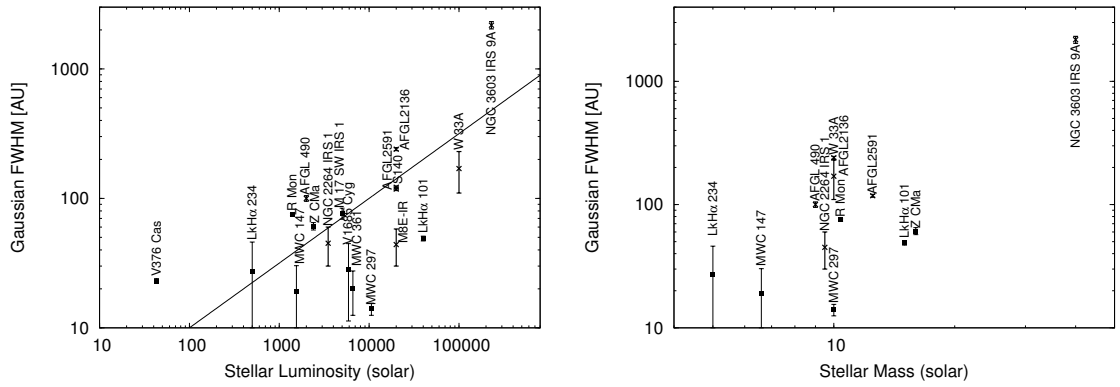

Figure 3.8: *Left:* Mid-infrared-size-luminosity diagram. Rectangulars correspond to Herbig Be stars, crosses to MYSOs. Values and references are shown in Table A.1. The black line corresponds to a $R \propto \sqrt{L}$ relation. *Right:* Mid-infrared-size-stellar-mass diagram. Rectangulars correspond to Herbig Be stars, crosses to MYSOs.

3.4.1 Comparison to MIR sizes of other massive YSOs

The near-IR sizes of the disks of most YSOs (in particular Herbig Ae stars) show a tight correlation with the luminosity (Monnier et al., 2005) because the emission in the NIR comes from regions close to the dust sublimation radius, which is sensitive to radiation from the central star and scales approximately with the square root of the luminosity. The mid-infrared emission, in contrast, originates from a wider range of regions: the hot inner wall located at the dust sublimation radius, the surface of an irradiated disk, and the circumstellar envelope. As shown in Monnier et al. (2009), the size of the region emitting in the MIR therefore spans a much larger region for a given luminosity. For circumstellar disks, factors such as the flaring of the disk and the shadowing caused by the inner rim play an important role. Here, we wish to compare the MIR size of NGC 2264 IRS 1 as found for the uniform disk model with the MIR sizes of other MYSOs, as well as with those of Herbig Be stars.

Only a few other MYSOs have been studied with high angular resolution in the MIR until now. Amongst them are AFGL 2591, AFGL 2136, AFGL 490, and S140 IRS 1 from the study of MIR sizes of Monnier et al. (2009), as well as W 33A (de Wit et al., 2007, 2010), and NGC 3603-IRS 9A (Vehoff et al., 2010). The sample of Herbig Be stars was also taken from Monnier et al. (2009). The disk size vs. luminosity diagram of these objects and NGC 2264 IRS 1, as well as the size vs. stellar mass diagram is shown in Fig. 3.8. Parameters such as stellar mass, distance, and the numbers for disk size and luminosity can be found in Table A.1. Both luminosity and mass of the central object seem to be correlated with the size of the MIR emission region. Owing to the factors considered above, objects with luminosities ranging between 1000 and 10,000 $L_\odot$ display a large scatter in their sizes (a factor of around 10). The same is true for the mass range of $\sim 8 - 20\,M_\odot$. The size of the MIR emitting region around NGC 2264 IRS 1 seems to be typical for their mass and luminosity.

3.4.2 Discussion of the radiative transfer models

Models of a circumstellar envelope only did not provide good fits, as they were unable to reproduce visibilities and NIR flux simultaneously. Furthermore, the estimated sizes of the dust distribution (Sect. 3.3.1) are different for different position angles, which implies that there is an asymmetric dust distribution.

The radiative transfer modeling performed with RADMC suggests that IRS 1 has an optical thick,

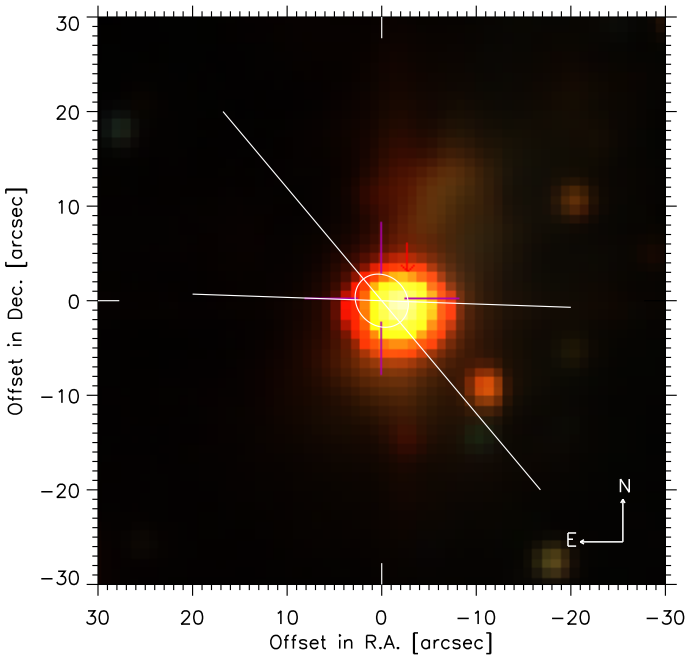

Figure 3.9: JHK composite image of NGC 2264 IRS 1 from observed with the 2MASS telescopes. We overlay an ellipse (white) that shows a disk seen under an inclination of 30° and a position angle of 40°. The size of the disk is not drawn to scale. The white lines show the orientations of the baselines.

but geometrically thin, flaring circumstellar disk with a mass of 0.1 $M_{\odot}$. This is supported by the results of the SED fitting process using the Robitaille grid. Not only the best-fit Robitaille disk model but also the ten best-fit models have parameters describing the central object and the circumstellar disk that compare very well with those of the best-fit model found using RADMC. However, the inclinations of the Robitaille models vary between 20° and 70°. The temperature and mass of the central object are slightly higher in all of these disk models than the values used for the RADMC model.

The two blackbody components producing the far-IR flux for our best-fit RADMC model could originate from a large surrounding cloud or envelope, respectively, that would with the large angular resolution of MIDI only be seen as foreground extinction. This would agree with the large foreground extinction (> 20 mag) as used in the best-fit RADMC and derived from the ten best-fit Robitaille disk models. Furthermore, previous publications have suggested that there is a large amount of foreground extinction with values between 20 mag (Thompson et al., 1998) and 35 mag (Thompson & Tokunaga, 1978). The inclination of the best-fit RADMC model is 30°, but owing to the poor uv-coverage this value is poorly constrained. The position angle of the jet-like feature seen in the near-IR is 20° (see Fig. 3.9), and the position angle in our best-fit disk model is 40°. This does not match perfectly, but the value for the position angle is also poorly constrained. However, an overall geometric picture of a moderately inclined disk seems reasonable.

3.5 Summary & conclusions

We have presented MIDI mid-infrared interferometric observations of the massive young stellar object NGC 2264 IRS 1. The observed visibilities provide *no* hint of multiplicity of the central source in the separation range from $\sim$ 30 AU (resolution limit) to $\sim$ 230 AU (slit width limit). Geometric models (Sect. 3.3.1) suggest a size of $\sim$ 30 – 60 AU for the mid-infrared emission region. This value is in good agreement with the mid-infrared sizes of similar objects.

Our modeling shows that a simple temperature-gradient model for a circumstellar disk can reproduce the SED at mid- and far-IR wavelengths, but fails to reproduce the SED in the near-IR and the observed visibilities; this model can therefore be ruled out.

We have performed a detailed radiative transfer modeling of the observed SED and visibilities with the RADMC code. It suggests a scenario of a geometrically flat but optically thick circumstellar dust disk. We also used the fitting tool by Robitaille et al. (2007), which leads to similar disk models and therefore confirms the results obtained with RADMC, whereas envelope models found within the Robitaille grid did not provide similarly good fits to SED and visibilities simultaneously. Although there is no observational evidence, the possible presence of a large ($r \geq 400$ AU) spherical envelope around the disk cannot be excluded by the data. The mass of the circumstellar disk is about 0.1 $M_\odot$. The data suggest an inclination angle of $\sim 30^\circ$ and a position angle of $\sim 40^\circ$ for the orientation of the disk. These values are consistent with an overall geometrical model based on the jet-like feature seen to the north-east of IRS 1. Comparing NGC 2264 IRS 1 to other YSOs, the size of its MIR emitting region seems to be typical of its luminosity and mass. However, the large scatter of sizes in this range of luminosities and masses points towards a wide variety of (disk) morphologies among these objects.

More observational research, such as future MIR interferometric observations, will provide tighter constraints on the circumstellar material around this interesting source and therefore will help us to clarify our understanding of the disks around high-mass YSOs.

Chapter 4

New constraints on the multiplicity of massive young stars in Upper Scorpius

Based on an article submitted to A&A on 05/11/2012:
Grellmann, R., Ratzka, T., Köhler, R., Preibisch, T., Mucciarelli, P., AA/2012/19577

4.1 Introduction

An accurate characterization of multiple stellar systems and their properties is one of the most important steps in understanding the star formation process itself . The observed properties of multiple systems, such as their separation, distribution, and mass ratios, provide important and strong constraints on star-formation theories. In order to make a comparison with observational surveys in a meaningful way, a complete knowledge of the 'primordial' multiplicity in a well characterized sample of young stars is needed. Complete means that all companion stars over the full range of possible orbital distances, that extends from a few stellar radii to several 1000 AUs, are known.

However, binaries are not only important from a statistical point of view. By following the orbital motion of a system, binaries can be used to determine fundamental stellar parameters. The most important stellar parameter is the stellar mass, as in combination with the chemical composition and the angular momentum a star's complete evolution can be determined. Direct mass measurements are particularly important for young stars, because the evolution models for the early stages of stellar evolution are still very uncertain and thus require mass measurements of adequate objects to be calibrated. Since the separations that can be resolved with long-baseline interferometry correspond to orbital periods between a few months and several years, many of the interferometrically detected multiple systems will be attractive targets for orbit determinations.

Another (and completely independent) indication for the presence of a companion to a B-type star is the detection of X-ray emission.

In this chapter new constraints on the multiplicity of a brightness selected sample of young stars in Upper Scorpius are presented. Both, interferometric and X-ray data are complementary methods to AO and spectroscopic searches of detecting and characterizing binary companions.

4.2 Target selection

OB associations are well-suited for studies of stellar multiplicity, because their youth implies that the binary parameters of only a handful of the most massive systems have changed and the low stellar densities guarantee that very little dynamical evolution will have taken place. Moreover, in contrast to small clusters or T associations like, e.g., Taurus-Auriga, OB associations contain a much wider range of stellar masses, including high- and intermediate-mass stars.

The OB association nearest to the Sun is the Sco OB2 or Scorpius-Centaurus association (145 pc). It consists of three subgroups, the youngest of which is Upper Scorpius (see e.g, Preibisch & Mamajek 2008; Blaauw 1991). The star formation process in Upper Sco is finished and there are neither dense molecular clouds nor deeply embedded young stellar objects. An extensive (and definitive) investigation of the high- and intermediate-mass stellar population in Scorpius-Centaurus was carried out by de Zeeuw et al. (1999). They used Hipparcos proper motions and parallaxes in conjunction with two moving group methods in order to accurately establish the stellar content down to mid-F spectral type ($\sim$2 $M_{\odot}$) and identified 120 stars as genuine members. In a series of spectroscopic studies, Preibisch & Zinnecker (1999) and Preibisch et al. (2002) have identified a large and statistically complete sample of low-mass members and then investigated the stellar population and star formation history of Upper Scorpius over the full stellar mass range from 0.1 $M_{\odot}$ to 20 $M_{\odot}$. They found that the whole stellar population in Upper Sco is very well characterized by a narrow age distribution around 5 Myr and that the initial mass function of Upper Sco is, within the uncertainties, consistent with recent determinations of the field initial mass function. These findings have been confirmed by an independent study of Slesnick et al. (2008).

Kouwenhoven et al. (2005, 2007) published an extended study about the primordial binary population in Scorpius Centaurus. Kouwenhoven et al. (2005) performed an adaptive optics search observing all Hipparcos members of spectral type A and late B using the ESO 3.6 m telescope at La Silla. Combining the literature data about multiplicity in Upper Scorpius and the new data they find that more than 80% of the B0–B3 type but only more than 60% of the B4–B9 type Hipparcos members in Upper Scorpius have one or more companions. The multiplicity for stars with spectral types A and F decreases even more.

To perform a search for close visual companions and to close the gap between the already existing spectroscopic and adaptive optics surveys, we selected all members of the Upper Scorpius association, which are bright enough to be observed with AMBER and the ATs (thus H- and K-band magnitudes $\leq$ 5.5 mag). AMBER is very well suited to find these companions, because in the near-infrared the contrast between the bright B stars and secondary components is much smaller than in the optical.

4.3 Interferometric AMBER Observations and data reduction

The AMBER (see Sect. 2.3.3) observations of B stars in Upper Scorpius at the VLTI (see Sect. 2.3.1) were performed in May 2010 in the course of the ESO observing program 085.C-0260(A). The Upper Scorpius data were taken with three ATs (diameter of 1.8 m) in the configuration A0-G1-K0 and in low-resolution mode (LR, spectral resolution 35).

For a reliable determination of the system parameters even in cases where a (rather wide) speckle companion is present, two observations (each yielding 3 visibilities and one closure-phase) per target are sufficient. An overview of the performed AMBER observations, including projected baselines, position angles, and calibrators used, can be found in Table 4.1. In total, only seven B stars of the 14 sample stars were observed, five of them only once, and only the remaining two have been observed

Table 4.1: AMBER Observations of targets in Upper Scorpius

Target	Other Name	Date	Projected Baselines						Calibrator(s)
π Sco	HIP 78265	06/05/10	87 m	-88°	75 m	151°	80 m	-140°	HD 143900
		10/05/10	90 m	-149°	90 m	-59°	126 m	-104°	HD 143404
τ Sco	HIP 81266	10/05/10	88 m	-85°	76 m	152°	79 m	-139°	HD 143404
ρ Sco*	HIP 78104	06/05/10	90 m	-160°	88 m	-70°	126 m	-115°	-
σ Sco	HIP 80112	11/05/10	124 m	-117°	87 m	109°	90 m	-162°	HD 135758, HD 143033
ω Sco	HIP 78933	11/05/10	128 m	-109°	91 m	116°	90 m	-154°	HD 143033
χ Oph	HIP 80569	06/05/10	90 m	-156°	90 m	-66°	127 m	-111°	HD 135758
		11/05/10	97 m	-97°	72 m	142°	86 m	-142°	HD 143033
ν Sco	HIP 79374	11/05/10	128 m	-106°	90 m	119°	90 m	-151°	HD 143033

*Data of low quality and not further mentioned in discussion

two times. However, the data taken of ρ Sco are very noisy and thus not taken into account for the further analysis and discussion. More information on the properties of all targets can be found in Table 4.2.

For the data reduction and calibration `amdlib` Vers. 3.0.4 (Tatulli et al., 2007; Chelli et al., 2009) provided by the Jean-Marie-Mariotti-Center[1] was used (see Sect. 2.3.3). In the here presented study, the calibration of the data was done by simply using only the associated calibrator. This is a simplified method, assuming that the (instrumental and atmospheric) transfer function has been stable between the science target and the calibrator. To get fully calibrated visibilities (i.e., a safe calibration for the absolute values of the visibilities), one would have to use a more sophisticated calibration method, using various calibrators taken over the whole night. Such a calibration of data taken in the LR-mode is, however, at the moment not validated. Anyway, for detecting a binary signal (i.e., a sinusoidal variation in the visibility) and revealing the position of the companion the employment of a more complicated method is not necessary.

In a first approximation, a binary can be described as composition of two point sources separated by the distance a. Here, a denotes the distance of the sources after projection on a plane parallel to the baseline $\vec{B}$. This means,that, e.g., having a baseline oriented perpendicular to the source separation vector, the projected distance would be equal to 0. The visibility of a binary is given by

$$V(B_\lambda) = \sqrt{\frac{1 + f^2 + 2f\cos 2\pi a B_\lambda}{(1+f)^2}},$$

with f being the flux ratio of the two sources ($f = I_1/I_2$). The frequency of this oscillation depends on the distance of the components, whereas the amplitude depends on their flux ratio.

To define the area in the separation-position angle parameter space, where a binary can be excluded due to our AMBER data, we make the following assumption: We can identify a binary signal if we see at least half a period of the modulation in one band (i.e., H- or K-band, sometimes we have only flux in the K-band data). Furthermore, considering a very wide binary, we need at least three data points per modulation. Due to the large errorbars of the data, we also need a flux ratio $\gtrsim 0.1$ (which

[1]JMMC, http://www.jmmc.fr

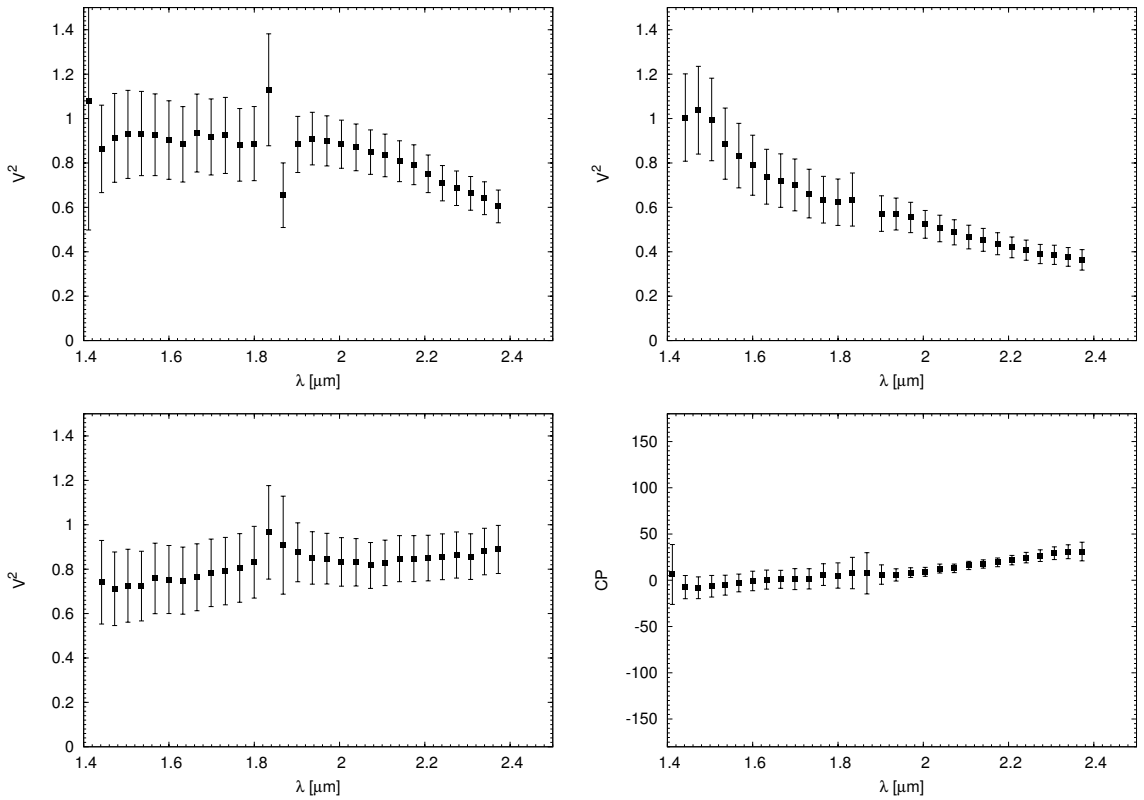

Figure 4.1: Visibilities and closure phase of σ Sco versus wavelength for the H- and K-band measured with AMBER on 11/05/10

is equivalent to $\Delta V = 0.2$), corresponding to a magnitude difference of $\Delta K \sim 2.5$ mag. This implies that we can detect companions with masses only down to $\sim 1.7\,M_\odot$ (Siess et al., 2000) to a primary of spectral type $\sim$ B3 ($M \sim 7\,M_\odot$).

4.4 Interferometric results

For four objects (τ Sco, π Sco, ω Sco, χ Oph) do not show any sign for a companion in their visibilities. Plots of the areas where a companion can be excluded from the AMBER data according to our definition can be found in Fig. A.1. We can estimate probabilities of missing a companion within a certain radius around the target, if it is by chance somewhere in the gaps of the covered area. The probability that we miss a component around one of the targets is $\sim 10 - 20\%$ for a radius of $\sim 0.12''$ around the primary star.

For σ Sco we can find an hint for an asymmetric structure (see Fig. 4.1). This signal seen in the closure phase and the visibilities might be due to the known spectroscopic companion (see Table 4.2). However, we can not exclude other possible reasons for the asymmetry, e.g., an inclined disk.

For ν Sco we can clearly detect a binary signal in the AMBER data. In Fig. 4.2 the calibrated AMBER visibilities in the H- and K-band of ν Sco are shown.

Table 4.2: Companions of the USco targets. s the observational limits for detectable companions change with the brightness of the primary target and the used baseline configuration, in row 7 the limits for each of the observed sample stars are given. The mass is the minimum required mass of the companion as obtained from the Siess et al. (2000) models for an age of 5×10^6 yrs to be able to be clearly detected. Below the range of separations covered by the observations is given.

Star	Component	Sep./Period [″]/days	Bright. (V) [mag]	SpT	Mass [$M_\odot$]	Detection Method	Comp. Det. Limit AMBER	Reference/Comment
ρ Sco	Aa		3.81	B2	10		$\sim 2.5\,M_\odot$ 2–125 mas	2
	Ab	4.003 d				spectroscopy		2,5
π Sco	Aa		2.83	B1	15		$\sim 4\,M_\odot$ 2–120 mas	2
	Ab	1.57 d		B2	10	spectroscopy		2,5 eclipsing binary
	B				0.4	X-ray companion		see Sect. 4.5
τ Sco	A		2.74	B0	18		$\sim 4\,M_\odot$ 2–100 mas	2
σ Sco	Aa		3.3	B1	15		$\sim 6\,M_\odot$ 2–105 mas	1,4
	Ab	33.01 d	5.3		3.5	spectroscopy		1,4
	B	0.43″	5.2	B7	3.5			1,4
	C	20″	8.6	B9.5	2.7			4
ω Sco	A		3.93	B1	15		$\sim 4\,M_\odot$ 2–100 mas	2
χ Oph	Aa		4.29	B2	10		$\sim 6\,M_\odot$ 2–130 mas	2
	Ab	34.12 d				spectroscopy		2,3
	Ac	138.8 d				spectroscopy		5
ν Sco	HR 6027 Aa		4.37	B2IV	10		$\sim 3.5\,M_\odot$ 2–100 mas	1
	HR 6027 Ab	5.55 d	6.9		1	spectroscopy		1,5,6,7
	HR 6027 B	1.305″	5.4		6			1,5,6
	HR 6027 C	0.063″	6.6		6			1,8
	HR 6026 A	41.1″	6.9	B8V	3			1
	HR 6026 Ba	2.0″	7.4	B9V	2.7			1,6
	HR 6026 Bb		7.9	B9V	2.7	spectroscopy		1,9
	HR 6026 C				1.5	X-ray companion		see Sect. 4.5

(1) MSC, Tokovinin (1997); (2) BSC, Eggleton & Tokovinin (2008); (3) Harmanec (1987); (4) North et al. (2007); (5) Kouwenhoven et al. (2007); (6) Levato et al. (1987); (7) Batten et al. (1989); (8) McAlister et al. (1990); (9) Andersen & Nordstrom (1983)

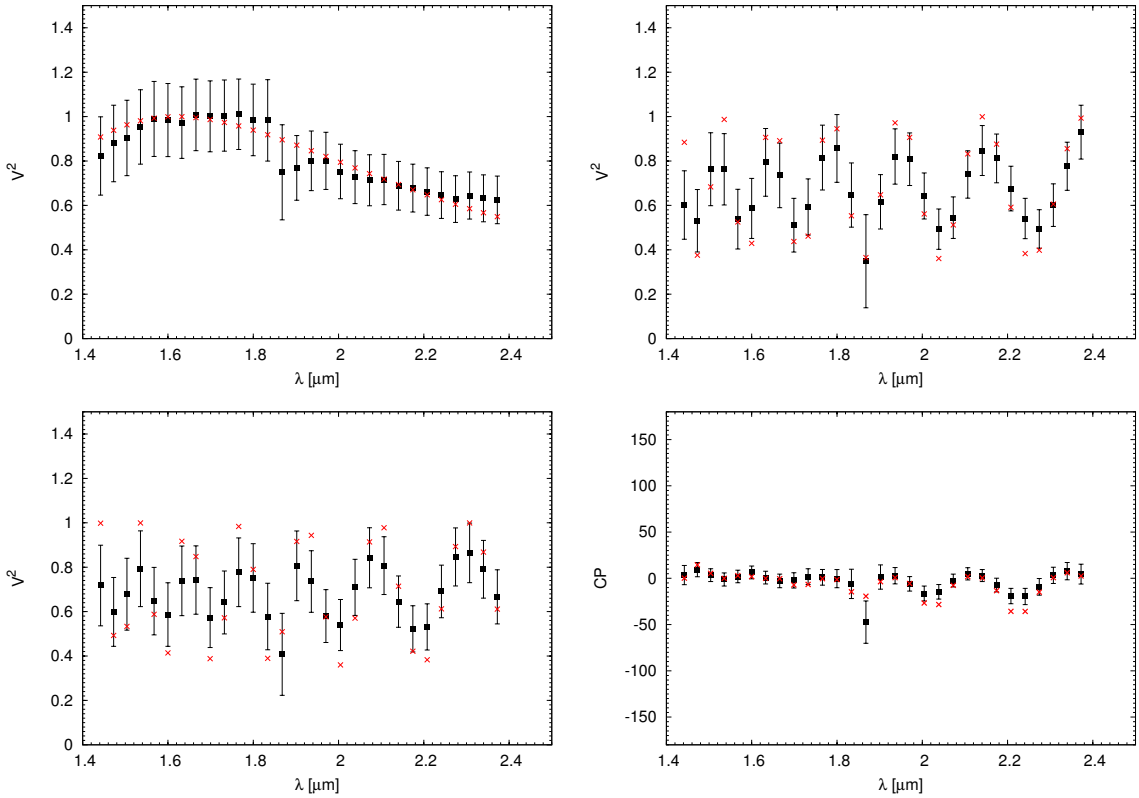

Figure 4.2: Visibilities of ν Sco versus wavelength for the H- and K-band measured with AMBER (black rectangulars) together with the best-fit LitPRO model (red crosses). *Upper Left:* Visibility with a baseline of 128 m and a PA of −106° *Upper Right:*Visibility with a baseline of 90 m and a PA of 119° *Lower Left:* Visibility with a baseline of 90 m and a PA of −151° *Lower Right:* Closure Phase

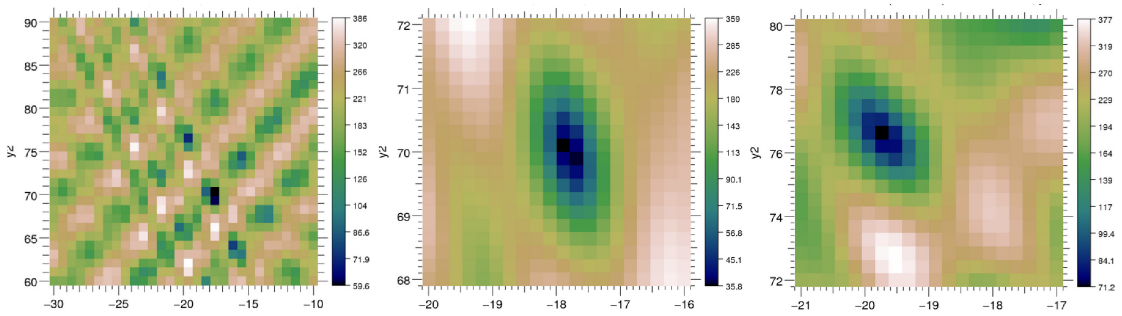

Figure 4.3: Reduced χ^2 maps produced with LitPRO from the fit of ν Sco. *Left:* Besides from the deepest minimum at −17.8 mas in RA and 70 mas in DEC we can see that there are other local minima. *Middle:* Zoom-in to the position of the minimum with lowest χ^2 *Right:* Zoom-in to the position of the minimum with second lowest χ^2

Table 4.3: Properties of the septuple ν Sco

Star	Sep./Period of Component [″]/days	Bright. (V) [mag]	SpT	Mass [$M_\odot$]	Reference
HR 6027 Aa Primary		4.37	B2IV	10	1
HR 6027 Ab Spectr.	5.55 d	6.9		1	1,2,3,6
HR 6027 B Visual 1	1.305″	5.4		6	1,2,6
HR 6027 C Visual 2	0.063″	6.6		6	1,4
HR 6026 A Primary	41.1″	6.9	B8V	3	1
HR 6026 Ba Visual	2.0″	7.4	B9V	2.7	1,2
HR 6026 Bb Spectr.		7.9	B9V	2.7	1,5
HR 6026 C X-ray				~ 1.5	see Sect. 4.5

(1) MSC, Tokovinin (1997); (2) Levato et al. (1987); (3) Batten et al. (1989); (4) McAlister et al. (1990); (5) Andersen & Nordstrom (1983); (6) Kouwenhoven et al. (2007)

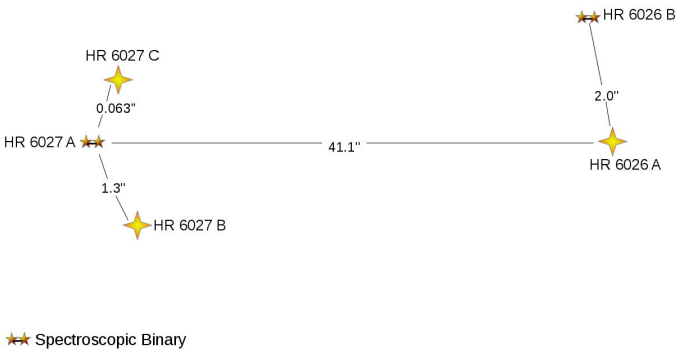

Figure 4.4: Schematic view of the ν Sco system (not to scale)

4.4.1 ν Sco

The object ν Sco (HIP 79374, HR 6027/HR 6026) is listed as a septuple system in the Multiple Star Catalog (MSC, Tokovinin, 1997). The system can be divided into two sub-systems, centered around the primary stars HR 6027 and HR 6026, which have a separation of 41.1″. HR 6027 is a spectroscopic binary and has two visual companions at ≈ 1.3″ and ≈ 0.060″. HR 6026 has one visual companion at a distance of ≈ 2.0″, which itself is a spectroscopic binary (see also Fig. 4.4). More details about this septuple of stars can be found in Table 4.3.

To determine the position of the companion of ν Sco, we used the LitPRO modeling tool developed at the Jean-Marie Mariotti Center (Tallon-Bosc et al., 2008). This tool was specially developed to perform model fitting of optical long-baseline interferometric data. The user can choose between a variety of simple geometrical models and different limb darkening functions, which are especially useful for the modeling of stellar sources. Furthermore, a visualization of the χ^2 plane for any two parameters allows a relatively easy finding of the global minimum.

As the radius for a star of spectral type B1 is ∼8 $R_\odot$, what corresponds for Upper Scorpius to a size ∼0.25 mas, the stars themselves are practically unresolved in the AMBER observations. Thus, a model consisting of two point-sources can be used for the determination of the companions position. We find that the companion is located northwest of the primary with an offset in Right Ascension of −17.8 mas and in Declination of 70 mas (χ^2 = 35.8). The error of the companion's position measured this way arises, i. a., from the uncertainty in the wavelength calibration of the AMBER data. Furthermore, the visibility obtained with the 128 m baseline shows only one oscillation for which it is difficult to determine the exact oscillation frequency. We thus assume an error of 10% in both directions (RA and Declination) of the final position. In the χ^2 map shown in Fig. 4.3 we can see a second minimum located at −19.7 mas in right ascension and 76.5 mas in declination. The χ^2 for this minimum is, however, around two times higher than for the other minimum. As it furthermore falls in the region included in our errorbars we don't discuss this solution separately. For the flux ratio of HR 6027 A and HR 6027 C the fit delivers $F_A/F_C \approx 4$, however, this value should be taken as very rough determination, as the errors on the absolute values of the visibilities are relatively large.

In addition to our new position obtained above, four earlier positions of the companion measured using speckle interferometry can be found in the literature (see Table A.3). Two data points were measured with the CTIO (Cerro Tololo Inter-American Observatory located in Chile, equipped with a 4.0 m primary mirror) and the CFHT (Canada France Hawaii Telescope located on Hawaii, equipped with a 3.6 m primary mirror) using adaptive optics systems (McAlister et al., 1990, 1993). The typical errors of such measurements were recalculated in Hartkopf et al. (2000). Furthermore, Tokovinin (2012); Tokovinin et al. (2010) and Hartkopf et al. (2012) measured the system recently using the 4.1 m SOAR telescope. All orbit points can be found in Table A.3.

4.4.2 Determination of the system orbit and the stellar parameters

We estimated the orbital parameters of the pair ν Sco A-C by fitting orbit models to all observations listed in Table A.3. We followed the procedure for fitting binary orbits outlined in Köhler et al. (2008, 2012): a grid-search in eccentricity e, period P, and time of periastron T_0. At each grid point, the Thiele-Innes elements were determined by a linear fit to the observational data using Singular Value Decomposition. From the Thiele-Innes elements, the semimajor axis a, the angle between node and periastron ω, the position angle of the line of nodes Ω, and the inclination i were computed.

The grid consisted of 100 points with $0 \leq e < 1$, 200 points within 1 yr $\leq P <$ 100 yr, and initially 200 points for T_0 distributed over one orbital period. After the initial scan over T_0, the best estimate

Table 4.4: Parameters of the best orbital solution.

Orbital Element	Best-fit value
Date of periastron T_0	$2453919\,^{+110}_{-7}$
	(2006 Jul 2)
Period P (years)	$8.9\,^{+0.1}_{-0.1}$
Semi-major axis a (mas)	$82.9\,^{+1.0}_{-2.2}$
Semi-major axis a (AU)	$12.0\,^{+0.4}_{-0.5}$
Eccentricity e	$0.17\,^{+0.02}_{-0.01}$
Argument of periastron ω (°)	$351.7\,^{+1.0}_{-14.}$
P.A. of ascending node Ω (°)	$167.9\,^{+0.3}_{-0.3}$
Inclination i (°)	$95.6\,^{+0.5}_{-0.5}$
System mass M_S (mas^3/year^2)	$7200\,^{+310}_{-460}$
Mass error from distance error ($M_\odot$)	±2.3
System mass M_S ($M_\odot$)	$22\,^{+3}_{-3}$
reduced χ^2	9.1

for T_0 was improved by re-scanning a narrower range in T_0 centered on the minimum found in the coarser scan. This grid refinement was repeated until the step size was less than one day.

The companion has been observed on opposite ends of its projected orbit in 1988/1989 and 2010/2012, but not in the 21 years between 1989 and 2010. Therefore, several families of orbits are possible, where 21 years corresponds roughly to half an orbital period, 1.5 periods, 2.5 periods and so on. Consequently, we find a series of local χ^2-minima at different periods. However, many of these minima can be excluded because they result in unphysically high system masses. Excluding orbits with $M > 30\,M_\odot$ left us with three local minima. To improve the fits and overcome the limited resolution of the grid-search, we used the orbits at these three minima as starting points for a Levenberg-Marquardt χ^2 minimization algorithm (Press et al., 1992). The best-fit orbit solution is shown in Fig. 4.5, and its orbital elements are listed in Table 4.4. Formal errors for the orbital elements were determined by studying the χ^2 function around its minimum and finding the variation of each parameter that results in $\chi^2 = 1$. To convert the semi-major axis from mas to AU, we used the distance of 145 pc.

The orbit with a period of 8.9 years yields a system mass of $22 \pm 3\,M_\odot$, reasonably close to the mass expected for the stars (cf. Tab. 4.2). The other orbits give masses that are significantly lower than expected ($\sim 7\,M_\odot$ and $\sim 1.5\,M_\odot$). We conclude that the orbit with a period of 8.9 years is most likely to be close to the true orbit. It would be interesting to observe the system again in or around the year 2015, to see whether the companion is indeed on the other side of the primary.

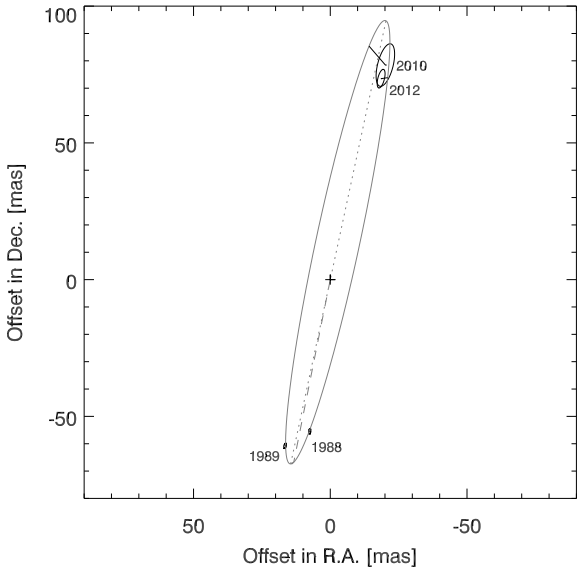

Figure 4.5: The orbit of HR 6027 C around HR 6027 A. The observed positions are marked by their error ellipses, the year of the observation, and lines connecting the observed and calculated position at the time of the observations. The dotted line indicates the line of nodes, and the dashed line marks the periastron.

4.5 X-ray emission as a tracer of late type companions

Stellar X-ray emission (see Güdel & Nazé 2009 for a recent review) is thought to be related either to coronal magnetic activity (e.g., Favata & Micela 2003) for low-mass stars ($M < 2M_{\odot}$) or to shocks in the wind of the very luminous O-type star (e.g., Kudritzki & Puls 2000). For stars in the spectral range between about B2 and A, neither of these two mechanisms can work: on the one hand, the winds of these stars are too weak to produce significant X-ray emission in shocks, and on the other hand, the lack of outer convection zones prevents the stellar dynamo generation of surface magnetic fields that would be required to produce significant X-ray emission from coronal plasma. These theoretical arguments are very well confirmed by the general lack of X-ray detections among late B- and A-type stars in a large number of X-ray observations (e.g., Preibisch et al. 2005; Stelzer et al. 2005b).

Some late B (and A) stars have been, nevertheless, detected as rather strong X-ray sources (Stelzer et al., 2006). In several of these cases, however, detailed observations (e.g., by the detection of X-ray eclipses) could show that the X-ray emission actually originates from a late-type (i.e., low-mass) companion and not from the B- or A-type primary star (e.g., Schmitt et al. 1993). In the context of the Chandra Carina Complex Project (Townsley et al., 2011), Evans et al. (2011) presented evidence that the X-ray-detected late B stars are binaries with low-mass companions. Consequently, the detection of X-ray emission from a late B or A-type star can be used as a good signature of the presence of an (unresolved) late-type companion.

We thus searched in the Heasarc Data Archive[2] to look for X-ray observations of the selected stars. We found available *ROSAT* data for three sources: HR 6026/6027, π Sco, and τ Sco. Count rates are extracted from circular regions for source and background using the FTOOLS XSELECT task.

[2]http://heasarc.gsfc.nasa.gov/docs/archive.html

We then used WebPIMMS[3] to convert the count rate into flux assuming a thermal APEC emission with kT ~1 keV and 0.4 solar abundances as typical for T Tauri stars. Galactic absorption is also taken into account using the A_V values reported by de Bruijne (1999).

ν Sco (HR 6026/6027): these two close sources have been observed by *ROSAT* with both HRI and PSPCB. We extracted the count rate from an on-axis HRI observation (Obs.Id. RH201631A01) that lasted about 2100 s. Extraction regions for HR 6026 and HR 6027 have radii of 20″ in order to avoid contamination between the two sources. The background region has a 40″ radius. The extracted net count rates are (3.9±0.4)×10 $^{-2}$ counts s^{-1} and (1.2±0.3)×10^{-2} counts s^{-1} for HR 6026 and HR 6027, respectively. The intrinsic luminosities for the two objects are log[L_X] ~30.7 and 30.2, respectively (energy interval [0.1-2.0] keV). According to the observationally established correlation between X-ray luminosity and stellar mass for coronal sources (see, e.g., Preibisch et al. 2005), these X-ray luminosities suggest companions with masses of M ~1.5 $M_\odot$ for the case of HR 6026 and M ~1 $M_\odot$ for HR 6027. Being late B-type stars, none of the known three components in the HR 6026 system can be the source of the X-ray emission; this suggest the presence of an additional component in this system. In the case of the HR 6027 system, the spectroscopic companion Ab (with an estimated mass of 1 $M_\odot$) is a good candidate for the source of the observed X-ray emission.

π Sco: two *ROSAT* HRI observations are available for this source. We analyzed the longer one (Obs.Id. RH202044N00), with a 5100 s exposure time. The source is at an off-axis angle of 16.9′ near the edge of the detector. Source and background counts are extracted from circular regions of 50″ and 80″ radii, respectively. The net count rate for the source is (4.4±0.3)×10^{-2} counts s^{-1}. The intrinsic luminosity in the [0.1-2.0] keV range is then log[L_X] ~29.6 and it suggests the presence of a late type yet unknown companion with M ~0.4 $M_\odot$.

τ Sco: this B0 V star is very well studied in X-rays (Mewe et al., 2003; Cohen et al., 1997). The analysis of the high-resolution X-ray spectrum showed that the X-ray emission of this star can be explained by shocks in the strong radiation line-driven stellar wind of this hot star. In this case, the X-ray emission does *not* provide evidence for the presence of a late-type companion.

4.6 Summary & Conclusions

We presented new near-infrared interferometric data taken with AMBER at the VLTI of seven B stars in the Upper Scorpius region. The AMBER data show a clear binary signal for one of the observed sources, ν Sco. We can determine a new position of companion C using the visibilities and closure phase measurements. Together with other positions found in the literature we performed an orbit fit yielding the best-fit orbit shown in Fig. 4.5 and derive a system mass of $\sim$ 22 $M_\odot$, P = 8.9 years, and a semi-major axis of $\sim$ 12 AU.

Our analysis of archival X-ray data leads to the detection of X-ray emission from π Sco, τ Sco, as well as from the two subsystems of ν Sco, which are HR 6027 and HR 6026. The measured X-ray luminosities allow independent mass estimations for the X-ray sources π Sco ($\approx$ 0.3 $M_\odot$), HR 6026 ($\approx$ 2 $M_\odot$), and HR 6027 ($\approx$ 0.7 $M_\odot$) (see Sect. 4.5). For the B0 star τ Sco the measured X-ray flux is due to shocks in the wind of the primary star itself. For HR 6027 the probable source of the X-ray emission is HR 6027 Ab. For π Sco and HR 6026 none of the already known components of the

[3]http://heasarc.gsfc.nasa.gov/Tools/w3pimms.html

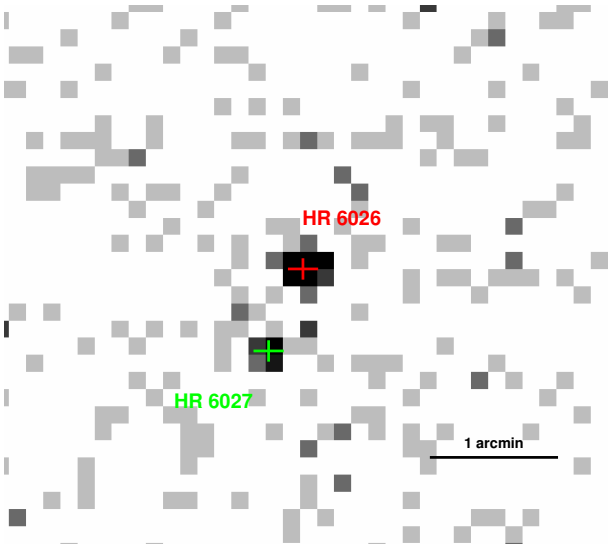

Figure 4.6: *ROSAT* X-ray image of the ν Sco system.

systems is in the mass range to serve as the source of the X-ray emission. Therefore, this observation strongly suggests the existence of an additional late type companion.

We do not detect any previously unknown companions with our interferometric observations. Although observations for our sample stars now exist over a complete spatial there may well be further, yet undetected companions. All of the used techniques (e.g., spectroscopic observations, interferometric observations, and adaptive optic surveys) might miss very faint companions. For the interferometric study the sensitivity limit implies that we miss companions with masses $\leq 1\,M_{\odot}$. For a more complete statistics our sample would have to be extended also with regard to the sensitivity.

Looking at Table 4.2 we find that the multiplicity for our sample is quite high. Including all stars and companions found (including the late type companions implied for π Sco and HR 6026 in the X-ray data, see Sect. 4.5) we find $\geq$ 2.0 companions per primary star on average. Even when not taking into account the HR 6026 system and component C of σ Sco (as they with 41″ and 20″ are relatively far away from the primary stars and thus likely unbound), we find $\geq$ 1.4 companions per primary. These numbers are comparable with the average number of companions found for stars with spectral type earlier than B3 in the Orion Nebula Cluster (~1.5, Preibisch et al. 1999).

Chapter 5

The multiplicity of massive stars in the Orion Nebula Cluster as seen with long-baseline interferometry

Based on an article submitted to A&A on 08/08/2012:
Grellmann, R., Preibisch, T., Ratzka, T., Kraus, S., Helminiak, K. G., Zinnecker, H., AA/2012/20192

5.1 Introduction

As already discussed in Sects. 4.1 and 1.2, the characterization of multiple stellar systems is an important ingredient for testing current star formation models. Stars are more often found in multiple systems, the more massive they are. This implies that a complete knowledge of the multiplicity of high-mass stars over the full range of orbit separations is essential to understand their still debated formation process. Such a complete picture can only be obtained by searching for companions in the full range of angular distances. Infrared long baseline interferometry is very well suited to close the gap between spectroscopic and adaptive optics searches.

The Orion Nebula Cluster

The Orion OB1 association is the nearest star forming region that produces low and high-mass stars. It is the most studied region of star formation spanning over 200 $\deg^2$ in the sky. A very detailed summary and discussion can be found in Reipurth (2008). The Orion OB1 association consists of several subgroups with different ages and different distances, what points to a sequential formation process (Bally, 2008). The very young subgroups are still embedded in their parental clouds, e.g., the Orion A and B molecular clouds (Megeath et al., 2005). The full membership of this OB association has not been established yet, but it is likely that between 5000 and 20,000 stars have been formed in the last 15 Myrs. The older subgroups of the Orion OB1 association lie with distances around 320 to 400 pc (Bally, 2008) closer to us than the younger subgroups with distances of 400 to 500 pc (Muench et al., 2008).

The Orion Nebula Cluster (ONC) is one of the two largest clusters in the youngest subgroup of the

Orion OB association and has an age of $< 2\,Myr$, Jeffries et al. 2011. Distance determinations found in the literature show a large range of determined distances for the ONC. This is probably due to the fact, that the ONC and the Orion 1c subgroup are projected along the same line of sight, with the Orion 1c group lying in front of the ONC. However, various recent studies point to a distance of $\sim 400\,pc$. E.g., Menten et al. (2007) used very long baseline radio interferometry to observe a couple of radio targets in the ONC and find a distance of 414 pc. The ONC contains $\sim$ 3500 young ($\leq 10^6$ yrs) stars, of which $\sim$ 30 are O- and B-stars (Hillenbrand, 1997; Da Rio et al., 2010, 2012). While many lower mass stars are still pre-main sequence (PMS) stars, the high-mass stars have evolved close to the main sequence.

The Orion Nebula H II region is created by the ionizing photons coming from the most massive star in the ONC, θ^1 Ori C ($\sim 38 M_{odot}$, Kraus et al. 2009). θ^1 Ori C is located in the so-called Trapezium system, consisting of the six primary stars A,B,C,D,E, and F, of which 5 are O- and B-stars. Each of the Trapezium stars is again multiple (see Fig. 5.1). Thus, conclusions if these systems are gravitationally bound can help to determine if predicted "mini-clusters" actually exist.

The multiplicity of the stars in the Orion cluster is already well characterized as far as either very close spectroscopic ($\leq$ 1 AU) or relatively wide visual systems ($\geq$ 50 AU) are concerned. Searches for spectroscopic binaries among ONC members have been performed by, e.g., Abt et al. (1991); Morrell & Levato (1991); Herbig & Griffin (2006). Searches for wide visual binaries have been performed with HST imaging (Padgett et al., 1997), speckle holographic observations (Petr et al., 1998), and near-infrared adaptive optic observations (Simon et al., 1999; Close et al., 2012).

Weigelt et al. (1999) and Preibisch et al. (1999) performed a bispectrum speckle interferometric survey for multiple systems among the O- and B-type Orion Nebula cluster members and found 8 new visual companions. A particularly interesting result of these speckle observations was the discovery of a close (33 mas, $\sim$ 15 AU) visual companion to θ^1Ori C, the most massive star in the cluster. Kraus et al. (2007, 2009) followed the orbital motion of this system. They used speckle observations, and several interferometric data taken with IOTA and the Astronomical Multi-Beam Combiner (AMBER) at ESOs Very Large Telescope Interferometer (VLTI). This allowed them to determine the orbit of this system and to derive fundamental parameters such as the stellar masses and an orbital parallax. Combining all results from the different observing techniques it is possible to draw general conclusions about the multiplicity of OB stars in the ONC. The number of known companions per primary star is with 1.5 companions per primary (Preibisch et al., 1999) around three times higher than for low-mass primary stars. This is in agreement with the suggestion that multiplicity is a function of the mass of the star and is increasing with increasing stellar mass.

While these searches for spectroscopic and visual companions have already provided us with important information about the multiplicity of those stars, there is still a serious gap in the range of separations covered, extending from separations of a few milliarcseconds (mas) [$\sim$ 1 AU] (too wide for spectroscopic detection) to $\sim$ 100 mas [$\sim$ 50 AU] (too close for speckle and adaptive optics studies). Thus, the derived number of 1.5 companions per primary is clearly a lower limit for the true multiplicity. An interferometric survey of a stellar sample that has already been searched for spectroscopic as well as wide visual companions can provide the required observational completeness, at least for sufficiently bright companions with flux ratios ≥ 0.1 ($\sim 2\,M_\odot$, see discussion section).

5.2 Observations and data reduction

The sample selected for the observations with AMBER consisted of all members of the Orion Nebula Cluster which are bright enough to be observed with AMBER (e.g., K magnitude $\leq$ 5.5) and the aux-

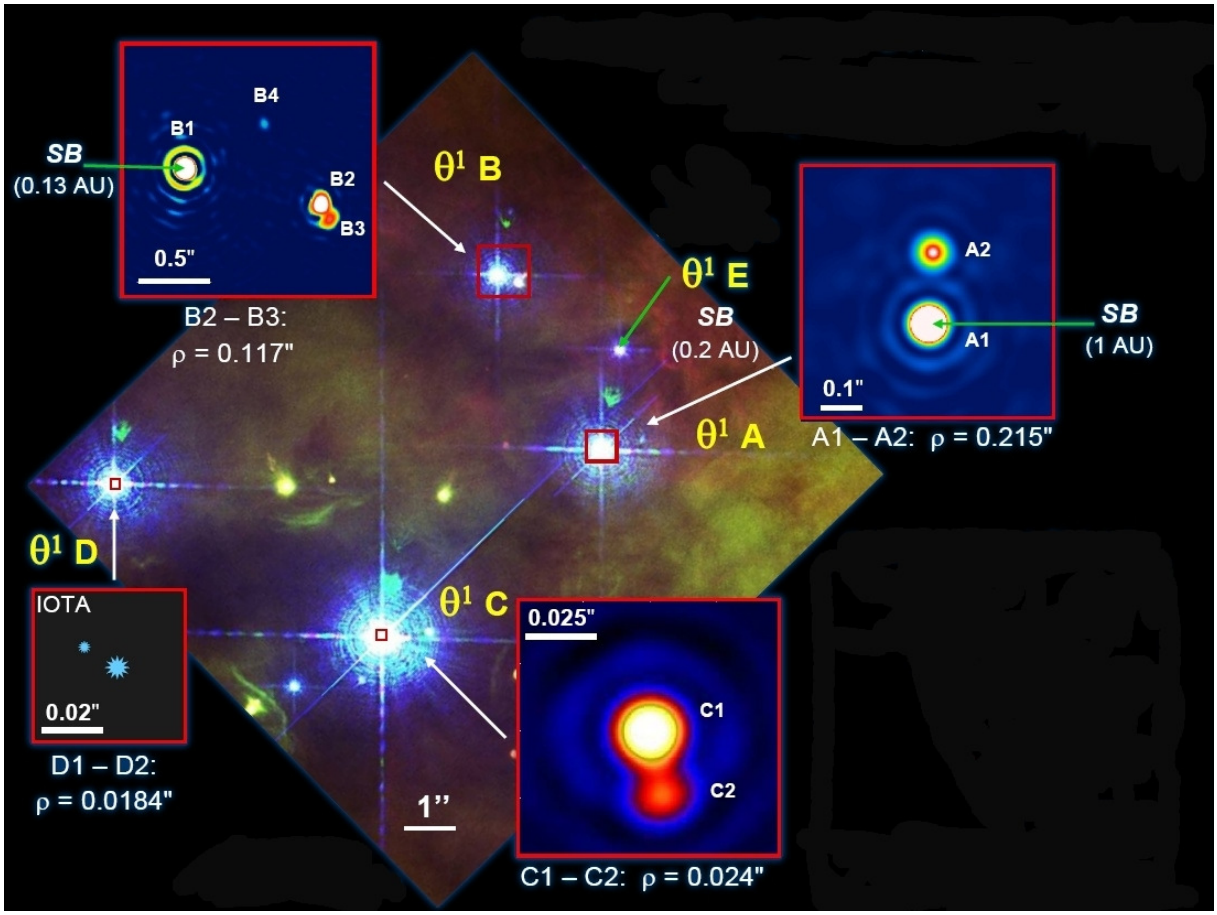

Figure 5.1: Hubble Space telescope image of the Trapezium system (Bally et al., 1998) together with the multiplicity of the stars as revealed by infrared interferometry.

iliary telescopes (ATs). This leads to a sample of 9 objects. For each target at least two observations are necessary for a reliable determination of the system parameters. For the observations of the ONC targets the low resolution mode (LR mode) with a spectral resolution of 35 was used.

The program was granted time in the course of the ESO program 086.C-0193 (P.I.: R. Grellmann). We also included in our analysis the previous observations of θ^1Ori C and D from the observing run 078.C-0360 (P.I.: S. Kraus). Further observations were taken as backup targets also in the course of the programs 386.C-0721 (P.I.: R. Grellmann), 386.C-0650 (P.I.: R. Grellmann), and 088.D-0241 (P.I.: K. Helminiak). Therefore, the data were taken with a variety of telescope configurations, which can be found together with information about baselines, position angles, and calibrators used in Table 5.1. All data were taken in the LR mode. In total, 6 stars (2 stars of spectral type O, 3 of spectral type B, and one A star) of the 9 sample stars were observed, two of them only once. However, some of the observations are of very low quality due to bad weather conditions. These data are not taken into account for the further analysis and discussion.

The amdlib software Vers. 3.0.3 (Tatulli et al., 2007; Chelli et al., 2009) provided by the Jean-Marie-Mariotti-Center[1] was used for the data reduction and calibration. As for the detection of a binary signal (i.e., a sinusoidal variation in the visibility) an absolute calibration is not necessary, the data were only calibrated using the associated calibrator rather than a set of calibrators observed over the whole night. This is a simplified method, assuming that the (instrumental and atmospheric) transfer function has been constant between the star and the calibrator. The most critical point for the calibration process is the accurate calibration of the wavelength, which is not guaranteed within the amdlib software. Thus, we compared the telluric absorption lines in the spectra of the calibrator stars (as they are brighter) with the telluric gaps in spectra observed at the Gemini Observatory, similar to the procedure described in Kraus et al. (2007) (but without dividing the object spectrum by the P2vm spectrum) and shifted them accordingly were necessary. However, the uncertainty in wavelength calibration is still the largest error source.

For the supplementing NACO data we searched the ESO archive, where we found a large number of observations in various filters. The data were reduced with the instrument-specific ESO pipeline and we selected those images in which θ^1Ori A is not or only marginally saturated. The relative positions of all stars were derived with `StarFinder` (Diolaiti et al., 2000), which performs PSF-fitting. In most cases θ^1Ori E served as PSF-reference. A comparison of the measured positions of the stars with the positions reported in McCaughrean & Stauffer (1994) allowed us to derive with `astrom`[2] for each image the detector orientation and plate scale. For this calibration the brightest stars, actual binaries and outliers were excluded. The relative position of the companion of θ^1Ori A in each epoch is listed in Table 5.4 . Since we have only analysed single images, the errors are hard to quantify. We thus show a conservative error of 5 mas in Fig. 5.3.

5.3 Modeling

As mentioned above, a typical sign for the existence of a companion (within a certain separation) is a sinusoidal variation of the visibility. Describing a binary as composition of two point-sources separated by the distance a the visibility is given by

$$V(B_\lambda) = \sqrt{\frac{1 + f^2 + 2f \cos 2\pi a B_\lambda}{(1+f)^2}},$$

[1] JMMC, http://www.jmmc.fr

[2] http://starlink.jach.hawaii.edu/

Table 5.1: AMBER Observations of targets in Orion

Target	Other Name	Date	Telescope Config.	Projected Baselines						Calibrator(s)
θ^1 Ori C	PAR 1891	05/10/10	A0-K0-I1	44 m	8°	110 m	-89°	123 m	70°	HD 32613, HD 34137
		26/12/10	A0-G1-K0	87 m	29°	88 m	-65°	128 m	72°	HD 32613, HD 33238
		27/12/10	A0-G1-K0	84 m	22°	90 m	-67°	122 m	70°	HD 32613, HD 33238
θ^1 Ori A	PAR 1865	14/12/10	G1-K0-I1	44 m	174°	38 m	-158°	79 m	-172°	HD 32613, HD 33238
		29/10/11	G1-K0-I1	44 m	171°	37 m	-162°	79 m	-176°	HD 40605, HD 33238
θ^1 Ori D	PAR 1889	14/12/10*	G1-K0-I1	43 m	180°	40 m	-150°	81 m	-166°	HD 33238, HD 47667
		17/01/11	U1-U3-U4	102 m	38°	58 m	-113°	130 m	64°	HD 34137, HD 33238
		29/10/11*	G1-K0-I1	43 m	177°	41 m	-147°	81 m	-163°	HD 33238
		30/10/11	G1-K0-I1	43 m	175°	38 m	-156°	79 m	-171°	HD 32613
		09/01/07*	U1-U3-U4	101 m	40°	43 m	125°	113 m	62°	HD 41547
θ^2 Ori A	PAR 1993	01/01/12	A1-G1-K0	128 m	-113°	74 m	110°	90 m	-147°	HD 34137, HD 40605
NU Ori	PAR 2074	26/03/11	A0-G1-K0	90 m	-144°	68 m	-52°	111 m	-106°	HD 32613, HD 40605
		27/03/11*	A0-G1-K0	89 m	-144°	60 m	-45°	99 m	-107°	HD 33238, HD 40605
		31/12/11	A1-G1-K0	127 m	-115°	80 m	107°	86 m	-153°	HD 32613, HD 40605
V* T Ori	PAR 2247	18/01/11	U1-U3-U4	102 m	40°	53 m	116°	126 m	64°	HD 34137

*Data of low quality and not further mentioned in discussion

with f being the flux ratio of the two sources ($f = I_1/I_2$, $0 < f < 1$), and a being the distance of the sources after projection on a plane parallel to the baseline $\vec{B}$. The distance of the two sources can then be determined from the oscillation frequency, whereas the oscillation amplitude depends on their flux ratio. When deriving the separation of the binary, i.e., the position of the companion, using only the visibilities an ambiguity of 180° remains. For a unique solution one needs to consider the closure phase, which is not affected by phase errors due to the earth atmosphere and provides information about the (a)symmetry of an object. The assumption of the sources being point-like is valid as the radius for a star of spectral type B1 is $\sim 8\,R_\odot$. For the Orion Nebula Cluster this corresponds to an angular size of ~ 0.1 mas. Thus, the stars themselves are unresolved with AMBER.

5.3.1 θ^1 Ori C

The most massive and brightest star in the Orion Nebula Cluster is θ^1 Ori C. According to its stellar temperature of $T_{\rm eff} = 39\,000$ K (Simón-Díaz et al., 2006) it is of spectral type O7-O5.5. θ^1 Ori C was discovered to be a close visual companion by Weigelt et al. (1999) using bispectrum speckle interferometry. Kraus et al. (2007, 2009) monitored the system to follow its orbital motion using infrared and visual bispectrum speckle interferometry as well as infrared long-baseline interferometry. They find a total system mass of $44 \pm 7\,M_\odot$ and an orbital period of 11 yrs.

For the determination of the position of the companion of θ^1 Ori C we used the LitPRO modeling tool developed at the Jean-Marie Mariotti Center (Tallon-Bosc et al., 2008). LitPRO is especially designed to perform model fitting of optical interferometric data. Different geometrical models can be chosen and combined, such as point-sources, disks, rings, and different limb-darkening functions. The fit of the model parameters can be visualized in a χ^2 plane for any two parameters, which enables an easy finding of local and global minima.

As mentioned above, a good model for binary sources in Orion observed with AMBER is a combination of two point-sources. Fitting the visibilities for the three observations of θ^1 Ori C, we find a minimum in the x-y-coordinate plane at ~ -25 mas in right ascension and ~ -35 mas in declination for all three measurements. The exact positions as well as older orbit points of the close visual companion can be found in Table 5.2. Plotting our positions together with the orbit points used by Kraus et al. (2009) (see Fig. 5.2) we find that the new obtained positions agree very well with the prediction. This confirms the orbital solution found by Kraus et al. (2009).

5.3.2 θ^1 Ori A

The B0.5 star θ^1 Ori A was discovered to have a spectroscopic companion at a separation of at ~ 1 AU by Bossi et al. (1989) and a close visual companion at a separation of ~ 500 AU by Petr et al. (1998). Schertl et al. (2003) followed the system's (orbital) motion over several years and found that the relative motion of the companion is consistent with an inclined circular or elliptical orbit, but also with a straight line (i.e., a physically unbound, chance projected system). Using the flux ratio from the speckle observations and photometric data compiled by Hillenbrand et al. (1998), Schertl et al. (2003) estimated the near-infrared magnitudes, the extinction, and finally the masses. For θ^1 Ori A1 they found $A_V \approx 1.89$ mag and $M \approx 16\,M_\odot$, for θ^1 Ori A2 they found $A_V \approx 3.8$ mag and $M \approx 4\,M_\odot$.

We determined new orbit points for θ^1 Ori A2 using archival NACO observations (see Table 5.3) and new AMBER observations. All new positions as well as the positions from older publications can be found in Table 5.4. The position determined from the AMBER data agrees very well with very recent observations taken with the Large Binocular Telescope (LBT) by Close et al. (2012). Fitting the observations with a linear movement, we obtain a relative velocity of $\sim 8.5 \pm 1$ km/s. This is

Table 5.2: Positions of the close visual companion of θ^1 Ori C

Date	PA [°]	Δ PA [°]	Sep. [″]	Δ Sep. [″]	Ref.
1997.784	226.0	3	33	2	1
1998.383	222.0	5	37	4	1
1999.737	214.0	2	43	1	2
1999.819	213.5	2	42	1	3
2000.873	210.0	2	40	1	3
2001.184	208.0	2	38	1	2
2003.8	19.3	2	29	2	3
2003.925	19.0	2	29	2	3
2003.928	19.1	2	29	2	3
2004.822	10.5	4	24	4	3
2005.921	342.74	2	13.55	0.5	3
2006.149	332.3	3.5	11.80	1.11	4
2007.019	274.9	1	11.04	0.5	5
2007.143	268.1	5.2	11.94	0.31	4
2007.151	272.9	8.8	12.13	1.58	4
2007.175	266.6	2.1	12.17	0.37	4
2007.206	265.6	1.9	12.28	0.41	4
2007.214	263.0	2.3	12.14	0.43	4
2007.901	238.0	2	19.8	2	5
2007.923	241.2	1	19.07	0.5	5
2008.027	237.0	3	19.7	3	5
2008.027	236.5	3	19.6	3	5
2008.071	236.2	2	20.1	2	5
2008.148	234.6	1	21.17	0.5	5
2008.173	236.4	1	21.27	0.5	5
2010.762	216.3	2	42.6	1	this paper
2010.986	215.7	2	43.4	1	this paper
2010.989	215.0	2	43.1	1	this paper

(1) Weigelt et al. (1999); (2) Schertl et al. (2003); (3) Kraus et al. (2007); (4) Patience et al. (2008); (5) Kraus et al. (2009)

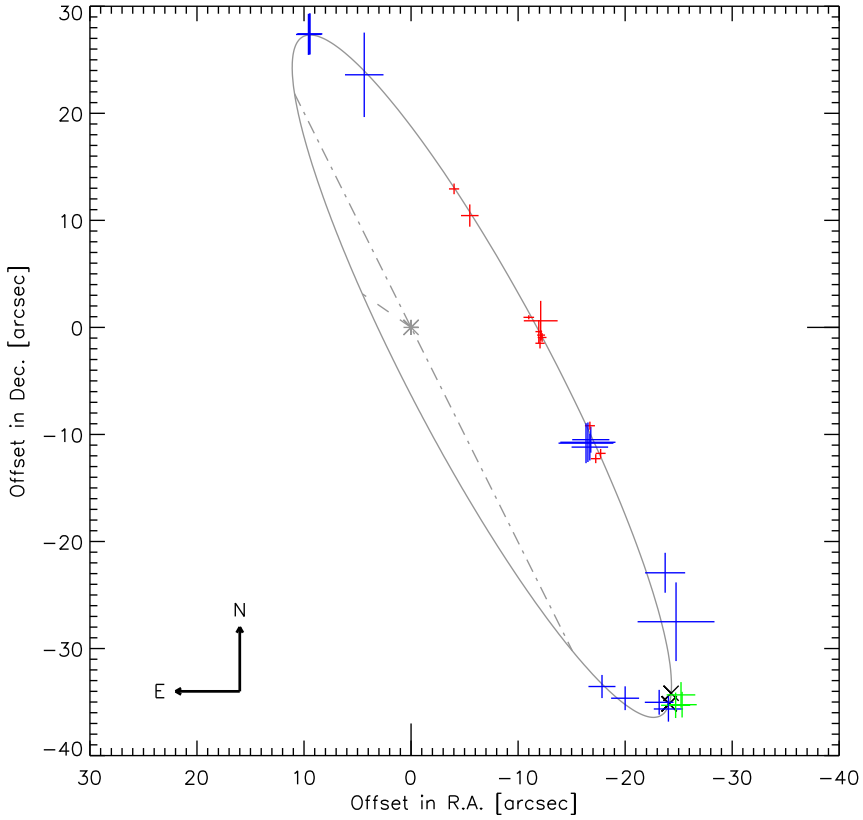

Figure 5.2: Orbit of θ^1 Ori C from Kraus et al. (2009). The green points are the new orbit positions measured with AMBER.

Table 5.3: NACO observations of the close visual companion of θ^1 Ori A

Date	Obs.-ID	Camera	Band
2003.7014	060.A-9026(A)	L27	L'
2003.9452	072.C-0492(A)	L27	L'
2004.9452	074.C-0637(A)	S13	Ks
2005.0603	074.C-0401(A)	L27	4.05
2005.9397	076.C-0057(A)	S27	2.17
2007.7041	079.C-0216(A)	S27	2.17
2009.0192	482.L-0802(A)	S27	2.12
2009.8849	060.A-9800(J)	S27	Ks
2009.8986	084.C-0396(A)	L27	L'
2010.2603	085.C-0277(A)	L27	L'

in between estimates of $\sim$ 7.2 $\pm$ 0.8 km/s by Close et al. (2012) and $\sim$ 10.3 km/s by Schertl et al. (2003). Menten et al. (2007) observed θ^1 Ori A2 using the Very Long Baseline Array. They find a proper motion of 9.5 km/s in RA and -3 km/s in Dec, what leads to a total velocity of $\sim$ 10 km/s well consistent with our velocity measurement. The velocity dispersion of the stars in the ONC has been estimated to be $\approx$ 2.3 km/s (Jones & Walker, 1988) assuming a distance of 470 pc. For a distance of 414 pc this scales to a velocity dispersion of 2.0 km/s. Since the relative velocity of A2 with respect to A1 is more than four times larger than this value it is highly unlikely that we see a random chance projection of unrelated stars. Furthermore, as discussed in Schertl et al. (2003), the probability to see a chance projected star with a K-band magnitude of $\leq$ 9 at an angular separation of $\leq 1''$ to the position of A1 is only 0.4%. Thus, although the observed motion is still linear and shows no significant curvature, we conclude that it is probably part of an binary orbit seen under a relatively high inclination.

5.3.3 θ^1 Ori D

θ^1 Ori D is of spectral type B0.5 and has been observed by Kraus et al. (2007) with the Infrared Optical Telescope Array (IOTA) in the H-band and using the LBT by Close et al. (2012) in the near-IR narrowband (2.16 μm and 1.64 μm). The LBT observations reveal a very wide optical companion with a distance of $\sim 1.4''$. It remains unclear, whether this source is really a physical companion or just, e.g., a background object. Kraus et al. (2007) detected a significant non-zero closure phase signal in the IOTA measurements and suggested the presence of a companion at a distance of 18.4 mas and a flux ratio of 0.14, although the uv-coverage and SNR was too low for a detailed characterization. We observed θ^1 Ori D with AMBER in five different nights (see Table 5.1), however, we can only take into account 2 of the 5 observations (from 30/10/11 and from 17/01/11) as the other ones are very noisy. We do not find a clear sinusoidal variation in the visibility; however, we a see a clear signal in the closure phase (see Fig. 5.4), which is consistent with a very close binary. In this case, we would expect to see only a slight increase or decrease in the visibility over wavelength band, which is consistent with the observations. Using the flux ratio of 0.14 as determined by Kraus et al. 2007 and fitting the data with the LITpro software we find minima for a separation of $\sim$ 2 mas for the observation on 17/01/2011 and a separation of $\sim$ 4 mas for the observation obtained on 30/10/2011. This would mean that the proposed binary has a highly inclined, (nearly) eclipsing orbit. An alternative explanation for the closure phase signal could be an inclined circumstellar disk, which would also be an interesting result for a star of spectral type B0.5.

Table 5.4: Positions of the close visual companion of θ^1 Ori A

Date	PA [°]	Δ PA [°]	Sep. [″]	Δ Sep. [″]	Ref.
1994.901	343.5	5	208	30	3
1995.775	350.6	2	227	5	2
1996.247	352.8	2	227	4	2
1996.746	352.7	2	223	4	2
1997.788	353.0	2	224	4	2
1998.838	353.8	2	221	5	2
1998.841	353.8	2	221.5	5	4
1999.715	355.4	2	219	3	2
1999.737	354.8	2	215	3	2
2000.765	356.2	2	215	4	2
2000.781	356.1	2	216	4	2
2000.781	356.0	2	211	4	2
2001.186	356.0	2	215	3	2
2001.718	356.9	1	205.1	3	1
2003.701	363.9	1	210	5	this paper
2003.945	363.9	1	209	5	this paper
2004.945	364.6	1	207	5	this paper
2005.060	365.3	1	208	5	this paper
2005.940	365.9	1	204	5	this paper
2007.704	366.1	1	202	5	this paper
2009.019	367.5	1	199	5	this paper
2009.885	368.2	1	197	5	this paper
2009.899	368.5	1	198	5	this paper
2010.260	369.4	1	197	5	this paper
2010.877	366.5	0.3	193.1	0.5	1
2010.953	366.2	1	193.0	2	this paper
2011.827	367.3	1	193.2	2	this paper

(1) Close et al. (2012); (2) Schertl et al. (2003); (3) Petr et al. (1998); (4) Weigelt et al. (1999)

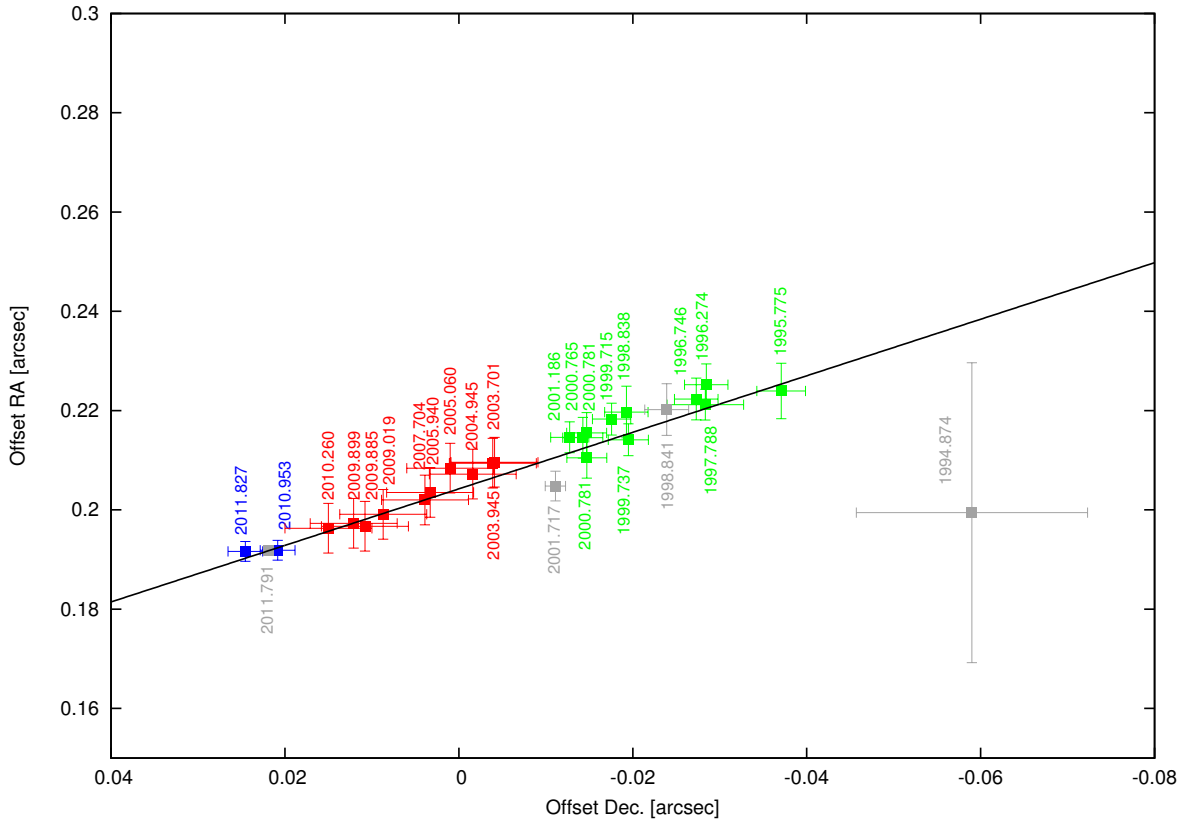

Figure 5.3: Positions of the companion of θ^1 Ori A. The blue positions are the new positions measured with AMBER, red are the new positions measured with NACO, green are the positions from Schertl et al. (2003), and the gray points are various other measurements (see Table 5.4).

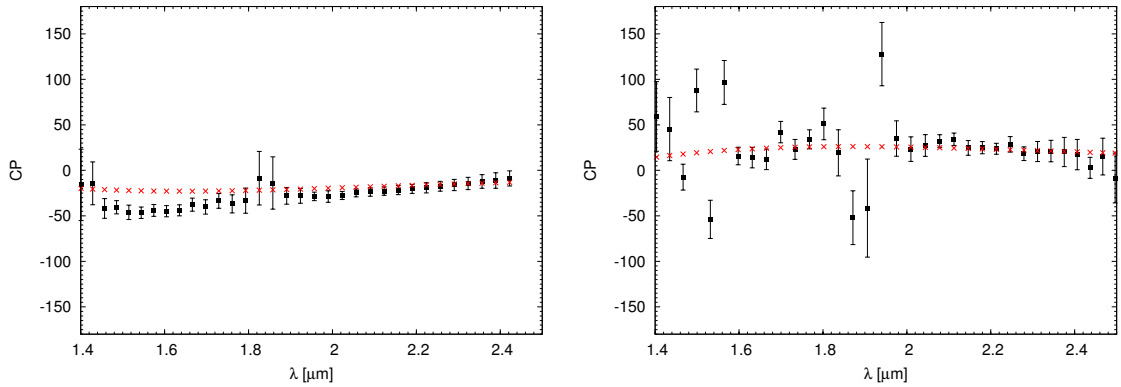

Figure 5.4: Closure phases of θ^1 Ori D from the observations in January 2011 (left) and October 2011 (right) together with the best-fit model as determined with LITpro.

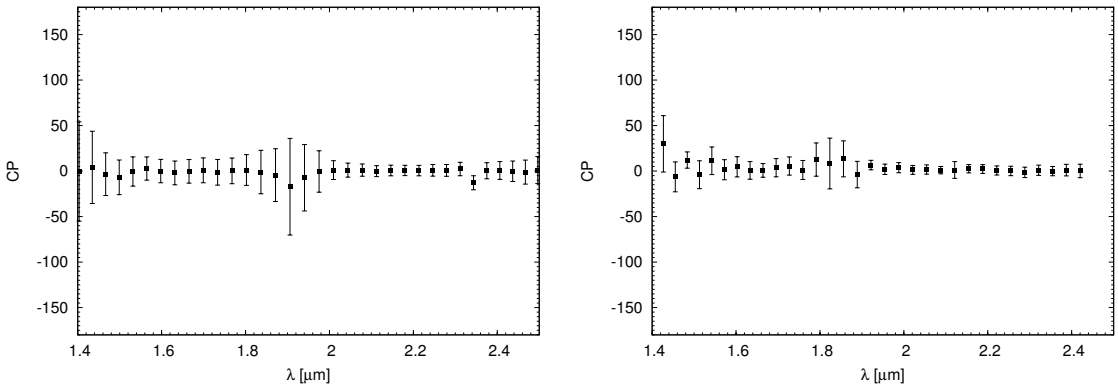

Figure 5.5: Closure phases of θ^2 Ori A and V* T Ori.

5.3.4 NU Ori

The B1 star NU Ori is known to have an spectroscopic companion with a period of 8 days (Morrell & Levato, 1991) and a wide visual companion at a distance of 0.47″ (Köhler et al., 2006). Our AMBER observations from 31/12/11 (see Fig. A.15) show a sine-like variation in the K-band, while the H-band data are too noisy to provide useful information. The data obtained on 26/03/2011 are very noisy on two of the three baselines (see Fig. A.16). However, there seem to be some oscillations in the visibility data. For the observations obtained on 31/12/11 we find a binary model which roughly fits the visibilities for separation of $\sim$ 20 mas, whereas the model for the data from 26/03/2011 favors a separation of $\sim$ 10 mas. The observations thus suggest the presence of a third companion in a hierarchical system, but further observations are needed to verify this prediction.

5.3.5 Other targets

In the data for θ^2 Ori A (spectral type O9.5) and V* T Ori (spectral type A3) we do not detect any clear signal for binarity in the visibilities (see Figs. A.17 and A.18). The closure phases (see Fig. 5.5) are $\sim 0^\circ$ and hence do not show any hint for an asymmetry either. We can thus define an area in the separation-position angle parameter space, where a sufficiently bright companion can be excluded. For this, we make the following assumption: a binary would be detectable in our data if we could see at least half a period of the modulation in one band (i.e., H- or K-band; sometimes we have only flux in the K-band data). In the other case (i.e., a very wide binary) at least three data points per modulation are needed to detect it. Due to the errorbars of the data, we furthermore can only be sure to detect binaries with a flux ratio of $\gtrsim 0.1$ (which would result in an amplitude of variation of ~ 0.2). Plots of the areas where a companion can be excluded from the AMBER data can be found in Fig. 5.6. It can clearly be seen there that the known 0.38″ separated companion of θ^2 Ori A is too far away already to be detected with AMBER. We now can also estimate the probability to miss a companion inside a certain radius, which depends on the baseline configuration (thus it can be different for different observations). The probability to miss a companion around θ^2 Ori A with a separation between 0.002″ and 0.11″ is $\sim$ 10%, if it is by chance in one of the gaps of the covered area. For V* T Ori we can detect a companion with a probability of $\sim$ 90% for separations between 0.002″ and 0.15″. To decrease the probability of missing a companion at least one more AMBER observation with an appropriate baseline configuration would be needed.

Table 5.5: Companions of the ONC targets. As the observational limits for detectable companions change with the brightness of the primary target and the used baseline configuration, in row 7 the limits for each of the observed sample stars are given. The mass is the minimum required mass of the companion as obtained from the Siess et al. (2000) models for an age of 10^6 yrs to be able to be clearly detected. Below the range of separations covered by the observations is given.

Star	Component	Sep./Period [″]/days	SpT	Mass [$M_\odot$]	Detection Method	Comp. detect. limits AMBER	Reference/Comment
θ^1 Ori C	C1		O5.5	~ 38		~ 4 $M_\odot$ 2–240 mas	2,5
	C2	0.040″		~ 5	speckle interferometry		5, this paper
	C3	0.002″		~ 1	spectroscopy		11
θ^1 Ori A	A1		B0.5	~ 20		~ 3 $M_\odot$ 3–280 mas	6
	A2	0.2″		~ 4	AO		2,3,4, this paper
	A3	65 d ≈ 1.5 mas	A0		spectroscopy		1,6
θ^1 Ori D	D1		B0.5			~ 3 $M_\odot$ 2–240 mas	4
	D2	1.401″			AO		10
	D3	0.0184″			interferometry		4, this paper
θ^2 Ori A	A1a		O9.5	~ 25		~ 3.5 $M_\odot$ 2–140 mas	6,7
	A1b			~ 9	spectroscopic		8
	A2	0.38″		~ 7	AO		7
NU Ori	Aa		B1			~ 2.7 $M_\odot$ 2–150 mas	6
	Ab	8 d ≈ 0.4 mas		~ 3	spectroscopic		6,8
	B	0.47″		~ 1	AO		9
	C	~0.015″			interferometry		this paper
V* T Ori	A		A3			~ 2.2 $M_\odot$ 2–200 mas	9

(1) Bossi et al. (1989); (2) Schertl et al. (2003); (3) Petr et al. (1998); (4)(1) Close et al. (2012); (5) Kraus et al. (2009); (6) Stelzer et al. (2005a); (7) Preibisch et al. (1999); (8) Morrell & Levato (1991); (9) Köhler et al. (2006); (10) Close et al. (2012); (11) Lehmann et al. (2010)

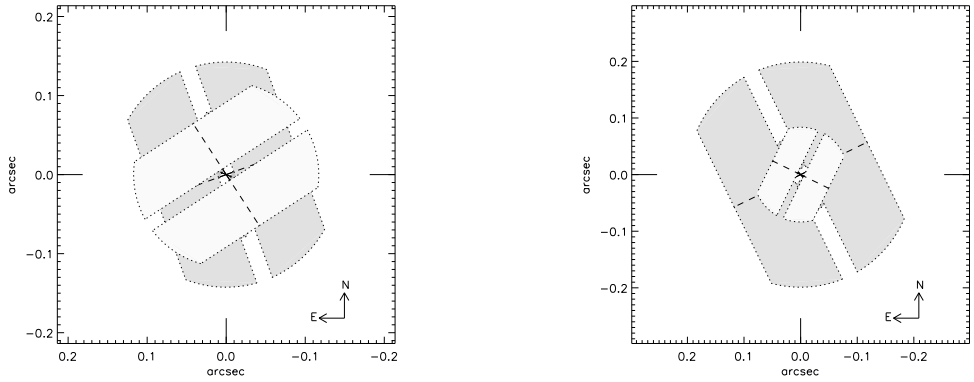

Figure 5.6: Coverage of the area around the observed objects, where a binary component within the defined conditions (see Chap. 5.3) can be excluded from the AMBER data. The different colors indicate the areas for the three different baselines and position angles. *Left:* θ^2 Ori A *Right:* V* T Ori

5.4 Summary & Conclusions

We presented observations of a brightness-selected sample of stars in the Orion Nebula Cluster obtained with the near-infrared interferometric instrument AMBER at the VLTI. We re-observed the already known companions around θ^1 Ori C at a distance of $\sim$ 40 mas and around θ^1 Ori A at a separation of $\sim 0.2''$. The new orbit points for θ^1 Ori C confirm the predicted orbital period of $\sim$ 11 yrs and confirms the stellar parameters derived from the fit. Combining the AMBER data with archival NACO data we can follow the motion of the companion of θ^1 Ori A. The motion is, however, still consistent with a linear movement, no curvature is detected in the trajectory. The relative velocity of $\sim 8.5 \pm 1$ km/s obtained from a linear fit is significantly higher than the velocity dispersion measured for the ONC, such that the observed motion is probably due to a companion with highly inclined orbit. For two of our targets, θ^1 Ori D and NU Ori, we find hints for the presence of further companions, which need to be confirmed by further observations.

The detection limits of the AMBER observations are depending on the brightness of the primary and the used baseline configuration. In Table 4.2 the covered range in angular separation and the required minimum mass of the companion are given for each of the observed targets. As mentioned in Sect. 5.3.5 we assume a minimum flux ratio of $\sim$ 0.1. This corresponds to a magnitude difference of ΔK $\sim$ 2.5 mag. Using the pre-main sequence models from Siess et al. (2000) for an age of 10^6 yrs we can calculate the minimum required companion mass to be detectable. With the AMBER observations we are able to detect companions with masses down to $\sim 3\ M_\odot$ and with projected angular separations of $\sim$ 1 to $\sim$ 80 AU.

The multiplicity in the Orion Nebula Cluster has been measured and discussed in various publications, e.g., Hillenbrand (1997); Preibisch et al. (1999); Köhler et al. (2006). Preibisch et al. (1999) find a companion frequency of $\geq$ 1.5 per primary for the massive stars (earlier than B3) in the ONC, which is around three times higher than for low-mass stars. Including all newly discovered possible companions the multiplicity in the ONC increases further. It might be even higher in reality as all of the techniques used to find companions miss, e.g., very faint companions. For our sample of two O and three B-type stars we find on average 2.2 known companions per primary, around four times more than for low-mass stars. This is in agreement with the finding that stars are more often found in multiple systems, the more massive they are.

Chapter 6

Spectro-interferometry of the Herbig Be star MWC 147

6.1 Introduction

During the last couple of years, infrared long-baseline interferometry has greatly advanced our knowledge about the spatial and temperature structure of the inner circumstellar material around YSOs. Near-infrared interferometry is able to resolve the innermost region on scales of a few AU or less, which were previously inaccessible to direct measurements.

The story of the investigation of the near-IR emitting region starts with the observation of the so-called NIR bump in the spectra of Herbig Ae/Be stars (Hillenbrand et al., 1992). To explain this feature the overall picture of the structure of circumstellar disks was described as a flat or flaring disk with an vertical inner rim of dust located at a distance of 5–15 stellar radii. The inner radii seemed to be consistent with a dust evaporation temperature of 1000–1500 K (depending on grain composition and sizes) and the observed correlation between the derived NIR ring size and the stellar luminosity $R \propto L^{1/2}$ (Monnier & Millan-Gabet, 2002; Monnier et al., 2005). Therefore, it was generally assumed that the near-infrared continuum emission from YSOs originates mainly from hot dust at the inner disk edge surrounding an optically thin region. Deviations from the size-luminosity relation were first explained with a structure of the inner rim different from the simple, vertical wall such as a puffed-up or rounded-of inner rim. While the exact shape of the inner dust rim is still a matter of debate, the situation got even more complex with the availability of larger interferometric data sets.

Near-infrared interferometric observations (Eisner et al., 2007; Kraus et al., 2008b; Benisty et al., 2010a, 2011) showed that the emission regions of some Herbig Ae/Be stars are more compact than what can be explained by emission from an inner dust rim and that an additional hotter component is needed. Therefore, the assumption of an optically thin (and thus transparent and non-emitting) region inside the dust sublimation radius seems to be incorrect. A possible scenario of the origin of this compact hot emission could be the presence of an optically thick inner gas disk. A schematic picture of the disk structure is shown in Fig. 6.1.

The question about the possible origin of the opacity of the inner gas disk is still unsolved. The temperature of the gas is most likely too low to allow strong continuum sources such as H^- to play a significant role, although for high accretion rates the inner disk can become optically thick. Another possibility is that the opacity is produced by a large variety of molecular lines (see Fig. 6.2).

The best way to gain new insight into these questions is to obtain spectro-interferometric obser-

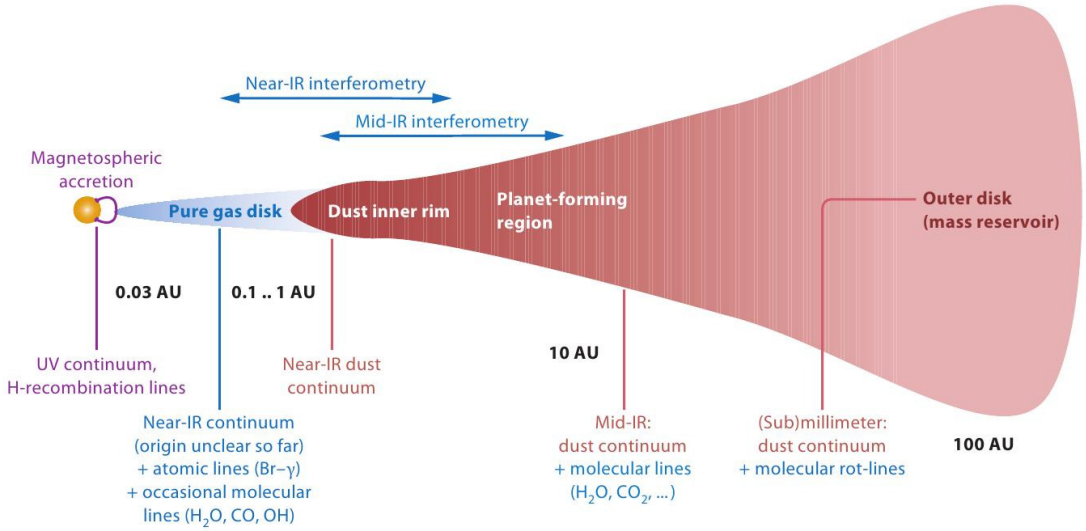

Figure 6.1: Sketch (not to scale) of the structure and scales of a typical circumstellar disk from Dullemond & Monnier (2010). The scale of the x-axis is not linear. The techniques which can resolve the strcutures spatially are shown above the picture.

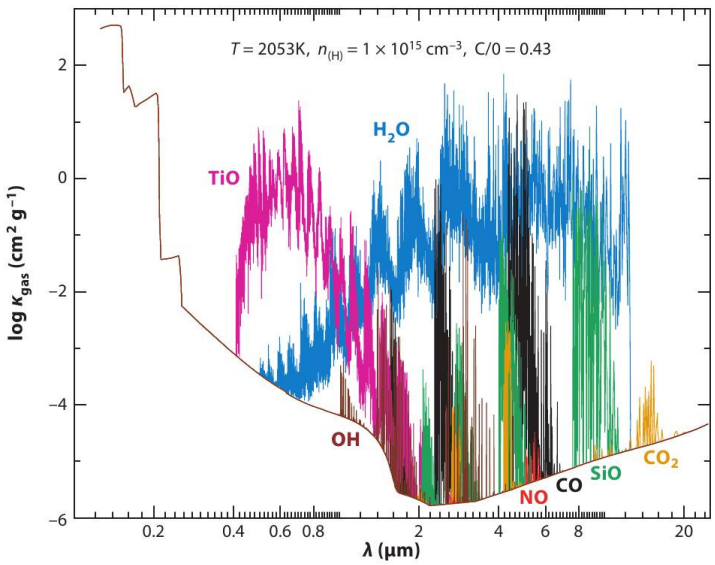

Figure 6.2: Opacities for expected gas constituents of the inner dust-free region of the disk from Dullemond & Monnier (2010).

vations that allow us to identify gas emission by atomic lines and/or molecular bands in the spectra of the innermost disk regions. Such studies have already been attempted but it seems that the inner gaseous disks show much less molecular emission than expected (Wolf et al., 2012). While Tatulli et al. (2008) can detect CO overtone emission originating from the inner 0.15 AU around the young Be star 51 Oph, the apparent detection of hot water molecular emission in MWC 480 (Eisner, 2007) inside the dust sublimation radius was invalidated by spectroscopic observations (Najita et al., 2009). Thus, the origin of the NIR emission inside the dust sublimation radius remains unclear and probably more complex.

Spectro-interferometric data with high spectral resolution ($R > 1000$) are needed to solve this problem, and allow us to clearly detect and identify molecular spectral signatures from hot gas, if present. The idea behind this method was first used by van Boekel et al. (2004) in the mid-infrared to investigate the dust composition at different radii of the circumstellar disk, which can give an insight into dust formation and destruction processes. The usually applied strategy is to compare the total flux (i.e., as measured with one single telescope) to the correlated flux (i.e., the total flux multiplied with the visibility). Depending on the length of the used baseline the measurement traces the emission on smaller or larger scales: the longer the baseline the smaller the scales and vice versa. A visibility amplitude (and thus a correlated flux) can be derived for each spectral channel and provides information about the wavelength-dependent spatial brightness distribution. Thus, comparing the correlated flux and the total flux at the wavelengths where (molecular) line emission is seen it is possible to draw conclusions on the spatial origin of the line emission.

The far most observed NIR emission line in young stars is the *Brackett γ 2.166 μm (Brγ)* line. It is of special importance because it is thought to correlate with the mass accretion luminosity $L_{\rm acc}$ of young stars as determined from UV veiling (Muzerolle et al., 1998; Calvet et al., 2004; van den Ancker, 2005). While the empirical relation between mass accretion is well established for T Tauri and Herbig Ae stars (Eisner et al., 2010), it is debatable for Herbig Be stars, for which Donehew & Brittain (2011) found that the Br γ luminosity is systematically larger than predicted from the relation. They suggest that while the emission of Br γ for Herbig Ae stars is due to accretion, for Herbig Be stars it may be dominated by emission from recombination in a wind or outflow.

Different Brγ formation scenarios have been discussed up to now. In the *magnetospheric accretion* scenario the line emission is produced by accretion of matter onto the star through magnetospheric accretion columns (van den Ancker, 2005). Such an infall should happen inside the *co-rotation radius*, which is defined as the radius where the Keplerian angular velocity equals the stellar angular velocity. As the co-rotation radius is closely located to the star, the infall and thus line emission should be originating from a compact region. Another possibility is the creation of Brγ emission lines by outflowing winds and/or jets. Here, three possible scenarios have to be considered: Stellar wind, stellar-field driven wind (also called *X wind*), and disk-field driven wind (also called *disk wind*). While for the stellar wind and X wind scenarios the line emission region is expected to be smaller than the emission region of the NIR continuum (i.e., the dust sublimation radius), for the disk wind scenario it should be similar or even larger. Furthermore, in the case of the existence of an inner gaseous disk, the recombination line emission from ionized hydrogen in this disk could also contribute to the total line emission. This would lead to sizes of the line emitting region equal or smaller as the continuum emitting region (see also Fig. 6.3 for a sketch of possible origins of Brγ line emission).

As a target for this study we selected the very well investigated Herbig Be star MWC 147. It was classified by Hernández et al. (2004) to be of spectral type B6, have a mass of $6.6\,M_\odot$ and an age of $3.2 \cdot 10^5$ yrs. Although values for the distance of MWC 147 found in the literature are ambiguous, the apparent location of the source in the Mon OB1 association points to a distance of $\sim$ 800 pc. MWC 147 is surrounded by a massive circumstellar accretion disk. Numerous infrared interferometric

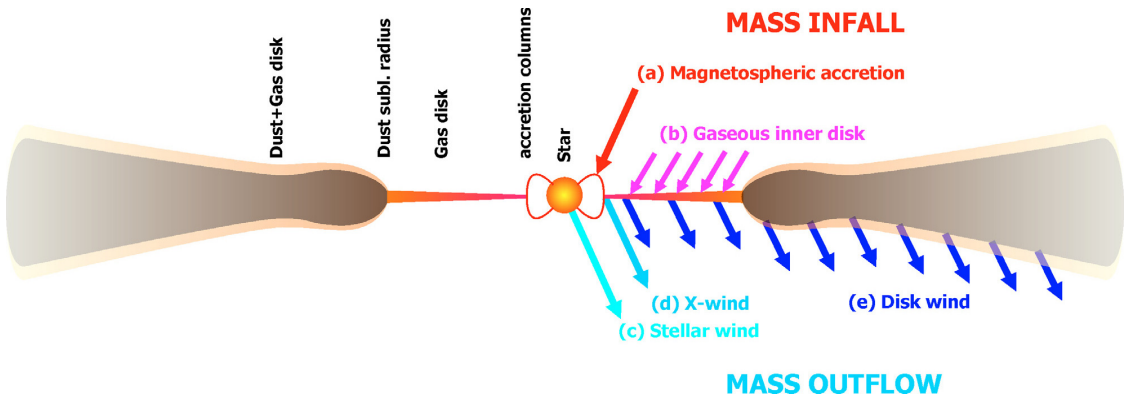

Figure 6.3: Sketch (not to scale) of possible regions emitting hydrogen recombination (e.g., Brγ) lines from Kraus et al. (2008b). Possible processes responsible for the Brγ emission are: Magnetospheric accretion, gaseous inner disk, stellar wind, X-wind, or disk wind.

observations of MWC 147 have been performed, with the Palomar Testbed Interferometer (PTI) and by Kraus et al. (2008b) with MIDI and AMBER at the VLTI, making this object one of the best interferometrically observed young stars in the sky. All available interferometric observations agree in requiring a remarkably small derived characteristic size for the NIR emission, considerably smaller than the expected dust sublimation radius of about 2.7 AU based on the stellar parameters.

Kraus et al. (2008b) performed extensive 2D radiation transfer modeling of the interferometric data for MWC 147. While models of passive, irradiated disks are able to reproduce the SED, they are in strong conflict with the interferometric observables, significantly overestimating the size of both the NIR and MIR emission. Adding an inner gaseous accretion disk component to the model resolves the discrepancies and provides good agreement between the model predictions and the data.

Further indications for the existence of a gaseous disk around MWC 147 inside the dust sublimation radius come from optical spectroscopy. Bagnoli et al. (2010) found that optical spectra of various emission lines point to an origin in a rotating circumstellar disk composed of a weakly emitting inner component and a more strongly emitting outer part. The break between these two components is derived to be at 2 to 3 AU, e.g., close to the expected dust sublimation radius at 2.7 AU. The inner disk is suggested to extend to at least 0.10 AU, what is close to the co-rotation radius estimated to be 0.07 AU.

6.2 Observational Results

MWC 147 was observed from January to March 2011 in the course of ESO observing program 086.C-0156 (P.I.: T. Preibisch) with AMBER at the VLTI in MR-K mode (see Sects. 2.3.3 and 2.3.1). In order to probe the radial dependence of the inner spectra, the approximately linear array UT1-UT2-UT3, that provides similar position angles for the three baselines, was used.

For the data reduction and calibration `amdlib` Vers. 3.0.4 (Tatulli et al., 2007; Chelli et al., 2009) provided by the Jean-Marie-Mariotti-Center[1] was used (see Sect. 2.3.3). For the calibration of the data the calibrator stars HD 45415 and HD 54079 observed before and after the science target, respectively, were used. The total flux is shown in Fig. 6.4. The spectrum was corrected for the telluric absorption lines by dividing the spectrum of the science target through the spectrum of the calibrator. A strong

[1] JMMC, http://www.jmmc.fr

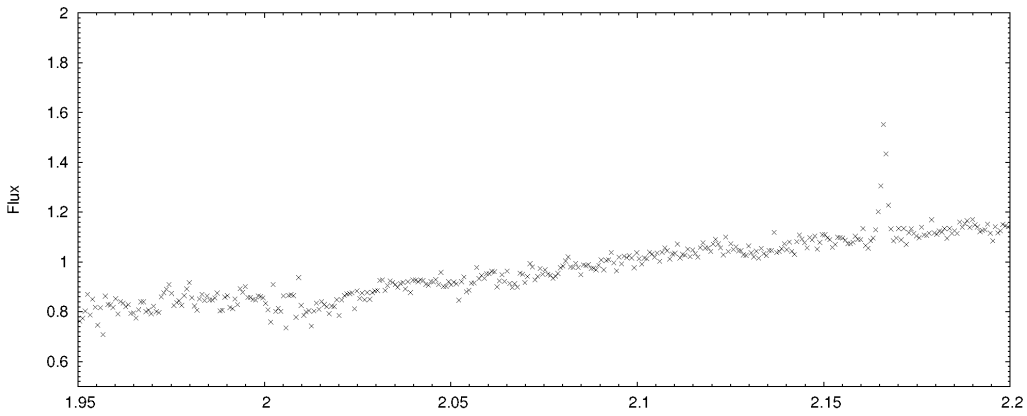

Figure 6.4: Total flux of MWC 14 over total flux of the calibrator versus wavelength as obtained with AMBER. No molecular lines can be identified, but one can clearly see the Br γ line at 2.166µm.

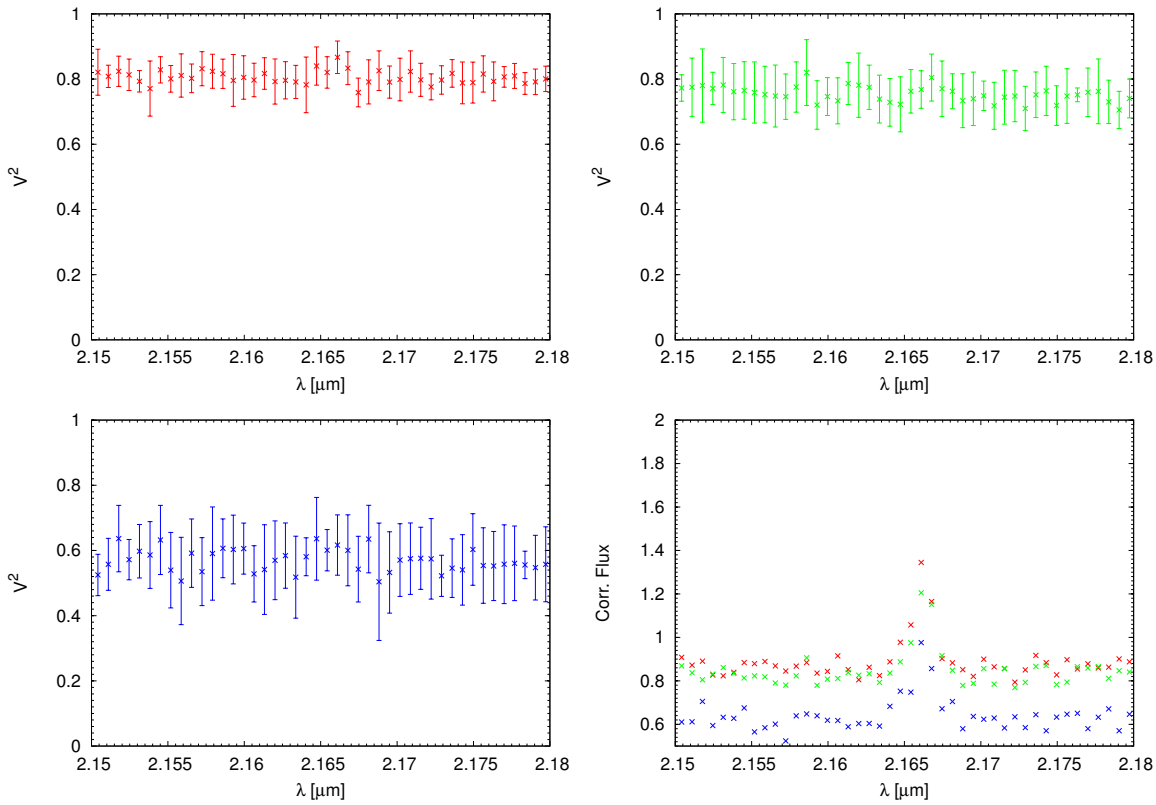

Figure 6.5: Visibilities and correlated spectra for MWC 147 as obtained with AMBER. *Upper Left:* Baseline UT1-UT2 (54.5 m, 35.8°) *Upper right:* Baseline UT2-UT3 (46.4 m, 46.2°) *Lower Left:* Baseline UT1-UT3 (100.4 m, 40.5918°) *Lower Right:* Spectrum including the Br γ line at 2.166µm.

emission line is detected at a wavelength of 2.166µm. This line is due to the 7 $\rightarrow$ 4 transition of atomic hydrogen, the Br γ line. Besides of the Br γ line no emission (or absorption) lines can be seen in the spectrum. The visibilities and the correlated fluxes (total flux multiplied with the visibility) as obtained with AMBER can be found in Fig. 6.5 for each baseline pair. The errorbars shown for the

visibilities were determined by computing the standard deviation between the five data subsamples.

6.3 Modeling

As explained in Sect. 2.2.3 circular symmetric structures with a non-uniform brightness distribution can in a first approximation be described by a Gaussian disk. We thus model the continuum visibilities with a Gaussian brightness distribution for each wavelength. In this way, we obtain a wavelength dependent size estimation for the emission region. The near-IR sizes vs. wavelength for all three baselines are shown in Fig. 6.5.

While the sizes obtained for the UT1-UT2 and the UT1-UT3 baselines are nearly equal, the third baseline (UT2-UT3) measurement provides slightly bigger Gaussian FWHM sizes. The sizes obtained for the UT1-UT2 and the UT1-UT3 baselines range between $\sim$ 1.6 and $\sim$ 2.4 mas (slightly increasing towards longer baselines), whereas the sizes determined for the UT2-UT3 measurement are between $\sim$ 2.5 and $\sim$ 3.0 mas. However, as the position angles of all three measurements are nearly the same, we conclude that the deviation is likely due to an incorrect calibration.

The near-IR continuum size of MWC 147 has been previously measured by Kraus et al. (2008b) using AMBER in Low-Resolution mode. Assuming a Gaussian brightness distribution and a distance of MWC 147 of 800 pc, they determine a characteristic diameter of the near-infrared emitting region of $\sim$ 1.3 AU. Converting the characteristic Gaussian diameters derived from our measurement from mas into AU using the same distance as Kraus et al. (2008b) we get NIR sizes between $\sim$ 1.3 AU and $\sim$ 2.0 AU (for the UT1-UT2 and UT1-UT3 baselines). This is comparable with the numbers as found in Kraus et al. (2008b).

As discussed before, when using spectro-interferometric observations it is not only possible to obtain the size of the continuum emitting region. Such observations provide furthermore information about the size of the line emitting regions (in this case the Br γ line emission region). Within the Br γ line we do not measure any significant deviation of the visibility with respect to the visibility measured in the continuum. This implies that the Br γ line is emitted in the same regions as the near-IR continuum.

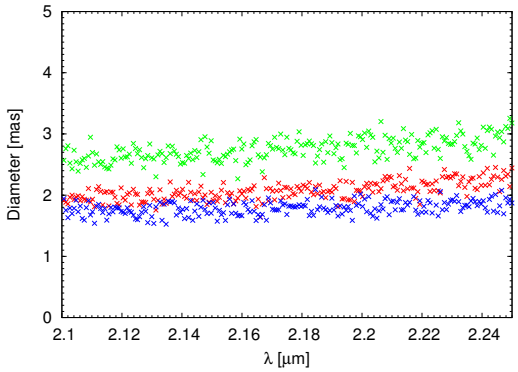

Figure 6.6: Near-IR diameter in mas of MWC 147 for the three different baselines (red: UT1-UT2, green: UT2-UT3, blue: UT1-UT3). To compute the size of the near-IR emission region Gaussian intensity profiles were assumed.

6.4 Discussion and Conclusions

Using spectro-interferometric observations obtained with AMBER in medium resolution mode we do not detect any molecular emission lines originating from the innermost parts of the disk, such as, e.g., H_2O, TiO, or SiO. This result is in contrast to the picture of an inner gaseous disk whose opacity is caused by molecular emission lines. Recent other studies (Wolf et al., 2012) show as well that the inner gaseous disks are poor in molecules. Thus, the composition of the material inside the inner dust rim remains unclear and probably much more complex than in the previously described picture of an inner gas disk. One possible alternative proposed by, e.g., Benisty et al. (2010a) could be the existence of high refractory grains such as iron, corundum, or graphite, which can survive at higher temperatures than the 1500 K usually used as dust sublimation temperature for silicates and thus closer to the star .

The second result of our study is the size of the near-IR emission region in general and in particular the size of the Br γ line emission. The characteristic diameter found for the NIR continuum emission region is determined to be 1.3 – 2 AU, what is in agreement with previously obtained values (Kraus et al., 2008b). As described above, the visibilities show no significant in- or decrease at the wavelengths of Br γ line emission. This means that the Br γ line emission region has a similar size than the continuum emitting region.

From this finding it is possible to draw conclusions on the possible line emission processes. In the magnetospheric accretion scenario matter will fall in along magnetic field lines and will glow brightly very close to the stellar surface. We thus would expect to see the Br γ line emission coming from a very compact region in this case. Our findings point, however, to a much larger line emission region, excluding not only the magnetospheric accretion scenario, but also the X-wind scenario, for which the emission should come from a region of hundredths or tenths of an AU. Therefore, our study supports the disk wind scenario (see also Fig. 6.3). This is in agreement with previous results for Herbig Be stars (Eisner et al., 2004; Malbet et al., 2007; Eisner et al., 2010).

Chapter 7

Summary and Outlook

In this thesis I employed infrared interferometric observations to investigate the formation process of high-mass stars from different points of view. Due to the unprecedented angular resolution interferometric observations in the infrared regime allow us to draw conclusions on the direct circumstellar environment of young stars. Resolving structures on scales between $\sim$ 1 mas and $\sim$ 100 mas they are perfectly suited to shed light on the star formation process from various sides.

One of the possible fields of application for infrared-interferometric observations is to search for companions around young stars. The covered angular separations can close the gap between spectroscopic and adaptive optics observations. Thus, infrared-interferometric observations are needed to provide a complete (in terms of angular resolution) statistics over the multiplicity rate. Another application is to follow the orbital motion of a binary system and thus make predictions about its orbital parameters, most important, the stellar masses. I will review the results obtained from the multiplicity studies in Sect. 7.1.

Furthermore, infrared-interferometric observations can provide important information on circumstellar disks. In order to understand the complex structure of the extended circumstellar disks and envelopes around young stellar objects, spatially resolved observations over an as large as possible wavelength range are required. The hottest material in the innermost ($\sim$ 0.1 to 2 AU) disk regions can be best traced at near-infrared wavelengths, while the warm parts (several hundred Kelvin) of the disk are best studied in the mid-infrared. Such studies are possible with the currently available VLTI instruments AMBER and MIDI, which furthermore provide information about the composition and distribution of the gas and dust due to their spectroscopic capabilities. I will review the results about infrared-interferometric observations in Sect. 7.2.

7.1 Multiplicity

We have used the ESO Very Large Telescope Interferometer to perform long-baseline interferometric observations of a sample of bright stars in the USco OB association and the ONC in the near-infrared. The Orion Nebula Cluster, a part of the Orion OB1 association, and the Upper Scorpius OB association are very good targets for such observations, as their stellar content is very well known from spectroscopic as well as adaptive optics searches. Our data are sensitive to companions in the separation range of $\sim$ 2 to $\sim$ 100 mas for a brightness ratio $\geq$ 0.1.

In Upper Scorpius we do not detect any previously unknown companions with our interferometric observations. A clear binary signal in the AMBER visibilities can be detected only for one of the

targets, ν Sco. We constrain the position of the companion using the AMBER visibilities and closure phase. Combining this new position with additional positions from the literature, we can perform an orbit fit and thus make an estimation for the orbital elements of the system. For the other targets we determine the parameter space in which the presence of companions can be excluded from our data. Furthermore, we used ROSAT X-ray data to search for indications of low-mass companions. For two of the B stars in our sample (π Sco and HR 6026), the detection of X-ray emission provides indirect evidence of low-mass companions. The multiplicity for our selected sample is quite high. Including all stars and companions found we find ≥ 2.0 companions per primary star on average for our sample of seven B-type stars (Grellmann et al., 2012A, submitted to A&A).

In the Orion Nebula Cluster we re-observed the already known companions around θ^1 Ori C at a distance of $\sim$ 40 mas and around θ^1 Ori A at a separation of $\sim 0.2''$. The new orbit points for θ^1 Ori C confirm the predicted orbital period of $\sim$ 11 yrs and the stellar parameters derived from the fit. Combining the AMBER data with archival NACO data we can follow the motion of the companion of θ^1 Ori A. We conclude that the observed motion is probably due to an highly inclined orbit. For two of our targets, θ^1 Ori D and ν Ori, we find hints for the presence of further companions, which however still need to be confirmed by further observations. Including all possible companions we find ~ 2.2 companions per primary for our sample of two O- and three B-type stars (Grellmann et al., 2012B, submitted to A&A).

Although for a more complete statistics our samples would have to be extended in particular with regard to the sensitivity, observations searching for companions in the full range of angular distances have been performed for our target stars. It is thus possible to draw conclusions on the multiplicity rate of OB stars. The number of companions per primary found for the selected sample of O- and B-type stars are comparable for the Upper Scorpius association and the Orion Nebula Cluster and are around four times higher than for low-mass stars. This number may even be higher in reality, as all of the techniques used to find companions (e.g., spectroscopic observations, interferometric observations, and adaptive optic surveys) miss, e.g., very faint companions. Our findings are in agreement with the suggestion that the multiplicity rate of young stars is increasing with increasing stellar mass.

7.2 Circumstellar Disks

NGC 2264 IRS 1: We used MIDI at the VLTI to perform long-baseline interferometric observations of NGC 2264 IRS 1, a massive young stellar object ($\sim 10\,M_\odot$) to spatially resolve the circumstellar material. Our observations resolve the circumstellar material around NGC 2264 IRS 1, provide the first direct measurement of the angular size of the mid-infrared emission, and yield direct constraints on the spatial distribution of the dust. We analyze the spectrally dispersed interferometric data taken with MIDI at two different position angles and baseline lengths. We use different approaches (a geometrical model, a temperature-gradient model, and radiative transfer models) to jointly model the observed interferometric visibilities and the spectral energy distribution.

The derived visibility values between ~ 0.02 and ~ 0.3 show that the mid-infrared emission is clearly resolved. The characteristic size of the MIR-emission region is $\sim 30 - 60$ AU; this value is in the typical range of recent results for other YSOs with similar or somewhat lower luminosities. A comparison of the sizes for the two position angles shows a significant elongation of the dust distribution. Simple spherical envelope models are therefore not consistent with the data. The radiative transfer modeling of our data suggests the presence of a geometrically thin and optically thick circumstellar disk with a mass of about $0.1\,M_\odot$. The data suggest an inclination angle of $\sim 30°$ and a position angle of $\sim 40°$ for the orientation of the disk. These values are consistent with an overall geometrical

model based on the jet-like feature seen to the north-east of IRS 1. Comparing NGC 2264 IRS 1 to other YSOs, the size of its MIR emitting region seems to be typical of its luminosity and mass. However, the large scatter of sizes in this range of luminosities and masses points towards a wide variety of (disk) morphologies among these objects.

Our modeling suggests that NGC 2264 IRS 1 is surrounded by a flat circumstellar disk that has properties similar to the disks found around lower mass young stellar objects. This result supports the assumption that massive young stellar objects form via accretion from circumstellar disks (Grellmann et al., 2011).

MWC 147: The existence of a circumstellar disk is well established for the Herbig Be star MWC 147. A large number of infrared interferometric observations of MWC 147 have been performed, with the PTI, MIDI, and AMBER. Infrared interferometric observations have shown that in some young stellar objects the bulk of the near-infrared emission does not (as usually assumed) originate from the hot dust at the dust sublimation radius, but from a more compact structure. The nature of this compact structure, perhaps hot gas in the inner accretion disk, is currently debated. This is also the case for MWC 147.

AMBER traces the hot inner regions of circumstellar disks and can due to its high possible spectral resolution provide information on the spectrum of proposed inner gas disk. By obtaining AMBER medium resolution K-band spectro-interferometric data we made a first attempt to obtain information about the nature of the compact infrared emission. The Brγ line is of special importance because it is thought to correlate with with the mass accretion luminosity of young stars. While this relation has been clearly established for T Tauri and Herbig Ae stars, it seems to be different in the case of Herbig Be stars what points to a different origin of the Brγ) line emission.

Assuming a Gaussian brightness profile we can estimate a size of the continuum emission region as well as of the Brγ line emission region. The characteristic size found for the NIR continuum emission region is determined to be $\sim$ 2 AU and does not show a significant in- or decrease at the wavelengths of Br γ line emission. From the size of the Br γ line emission region it is possible to draw conclusions on the possible emission processes. In the magnetospheric accretion scenario the line emission should happen very close to the stellar surface, i.e., in a very compact region ($<<$ 2AU). For the X-wind scenario the emission should come from a region of hundredths or tenths of an AU. Our study, however, supports the scenario of emission scenario through disk wind due to the size of the emission region of $\sim$ 2 AU. This is in agreement with previous results for the accretion regions of Herbig Be stars. We do not detect any signatures for emission from any molecules in the AMBER spectrum. This is also the case for spectro-interferometric observations of other Herbig AeBe, which show much less molecular emission the inner gaseous disks than expected. Thus, the origin of the NIR emission inside the dust sublimation radius remains unclear and probably more complex.

Infrared long-baseline interferometry has greatly advanced our knowledge about the spatial and temperature structure of the inner circumstellar material around YSOs which were previously inaccessible to direct measurements. To test the disk accretion scenario in massive star formation, IR-interferometry can be used to search for disks around high-mass stars. The detailed structure of disks can provide information of various important processes, such as the removal of angular momentum, the overcoming of the radiation pressure, and the launching of jets and winds.

7.3 Future perspectives

Many of the processes which are essential to understand star (and also planet) formation have to be studied on very small scales. This includes (to name only a selection) mass accretion processes,

which are closely connected to the structures of the inner parts of circumstellar disks, mass ejection and collimation processes, as well as close binaries and interactions between them. Furthermore, extrasolar planets are located and born at separations between 0.1 AU and 100 AU from the central star.

Interferometry is the only possibility to reach the required angular resolution. This is especially true for stars with higher masses as they are usually located in rather distant regions. The ability of modern interferometric instruments to additionally resolve the interferometric visibilities spectrally delivers further important information. Mid-IR interferometry (e.g., MIDI) can be used to study, e.g., the silicate emission feature of the circumstellar dust and probe the radial composition of the disks atmosphere. In the context of planet formation this can provide information about the mechanism of grain growth. Furthermore, density fluctuations and gaps in the disk, e.g., due to forming planets, can be detected. In the near-IR the high spatial and spectral resolution of interferometric instruments, e.g., AMBER, can be used to study the molecular content of the gas located inside the dust-sublimation radius.

Current limitations of interferometric observations are one the one hand the current sensitivity limits, which only allow to observe the brightest objects, and on the other hand the limited number of available baselines. Although single visibility measurements can support the determination of the disk parameters, observations with various baseline lengths and position angles are finally needed to fix them. Ideally even images can be reconstructed. MIDI, combining only two baselines at a time does not provide any unbiased phase information and can thus not be used to reconstruct images. To get highly resolved images of the warm parts of the circumstellar disk we will therefore have to wait till the completion and commissioning of the second generation VLTI instrument MATISSE (Lopez et al., 2006; Wolf et al., 2009), which will be able to combine light from four telescopes simultaneously at mid-IR wavelengths. While image reconstruction is theoretically already possible (and has been done) in the near-IR using AMBER a large amount of time is currently needed to obtain the great number of visibilities and phases required for an unbiased image reconstruction.

To reconstruct the complex structure of the extended circumstellar disks and envelopes around young stellar objects, spatially resolved observations over the largest possible wavelength range are required. While MIDI and AMBER trace the warm and hot regions of disks, observations at (sub-) millimeter wavelengths are sensitive to the cool material in the outer parts and the only way to derive the disk mass and the outer radius. The Atacama Large Millimeter Array (ALMA, Casasola & Brand 2012; Sheth 2012; Peck 2012) which is currently build will consist of 50 radio antennas and will have baselines ranging from as short as 15 m to as long as 16 km. The receivers will allow observations from wavelengths of 0.3 mm up to 1 cm. A comparison of images taken at different wavelengths, e.g. comparing AMBER, MATISSE, and ALMA results, will lead to a self-consistent picture of the disk at all scales. Such an approach will allow to test theoretical predictions of disk evolution and dust chemistry.

Interferometric studies are also needed for multiplicity studies to close the gap of covered companion separations between spectroscopic and speckle searches. While this is in principle already possible using AMBER, due to the sensitivity limit and the required observing time such observations are not very efficient. Significant progress will be made once the interferometric instrument for the Large Binocular Telescope (Hill, 2010) LINC-NIRVANA (Bertero et al., 2011) will be working. It will then be possible to make wide eld images with the spatial resolution corresponding to a 23 m telescope.

Bibliography

Abt, H. A., Wang, R., & Cardona, O. 1991, ApJ, 367, 155

Acke, B. & van den Ancker, M. E. 2004, A&A, 426, 151

Acke, B., Verhoelst, T., van den Ancker, M. E., et al. 2008, A&A, 485, 209

Allen, D. A. 1972, ApJ, 172, L55

Alonso-Albi, T., Fuente, A., Bachiller, R., et al. 2009, A&A, 497, 117

Alves, J., Lombardi, M., & Lada, C. J. 2007, A&A, 462, L17

Andersen, J. & Nordstrom, B. 1983, A&AS, 52, 471

Andre, P., Ward-Thompson, D., & Barsony, M. 1993, ApJ, 406, 122

Andre, P., Ward-Thompson, D., & Barsony, M. 2000, Protostars and Planets IV, 59

Asano, R. S., Takeuchi, T. T., Hirashita, H., & Inoue, A. K. 2012, ArXiv e-prints, 1206.0817

Baade, D., Meisenheimer, K., Iwert, O., et al. 1999, The Messenger, 95, 15

Bagnoli, T., van Lieshout, R., Waters, L. B. F. M., et al. 2010, ApJ, 724, L5

Ballesteros-Paredes, J., Klessen, R. S., Mac Low, M.-M., & Vazquez-Semadeni, E. 2007, Protostars and Planets V, 63

Bally, J. 2008, Overview of the Orion Complex, 459

Bally, J., Sutherland, R. S., Devine, D., & Johnstone, D. 1998, AJ, 116, 293

Bally, J. & Zinnecker, H. 2005, AJ, 129, 2281

Banerjee, R., Vázquez-Semadeni, E., Hennebelle, P., & Klessen, R. S. 2009, MNRAS, 398, 1082

Banerjee, S., Kroupa, P., & Oh, S. 2012a, ApJ, 746, 15

Banerjee, S., Kroupa, P., & Oh, S. 2012b, ArXiv e-prints, 1208.0826

Bate, M. R. 2009, MNRAS, 397, 232

Bate, M. R., Bonnell, I. A., & Bromm, V. 2002, MNRAS, 336, 705

Batten, A. H., Fletcher, J. M., & MacCarthy, D. G. 1989, Publications of the Dominion Astrophysical Observatory Victoria, 17, 1

Baxter, E. J., Covey, K. R., Muench, A. A., et al. 2009, AJ, 138, 963

Benisty, M., Natta, A., Isella, A., et al. 2010a, A&A, 511, A74

Benisty, M., Renard, S., Natta, A., et al. 2011, A&A, 531, A84

Benisty, M., Tatulli, E., Ménard, F., & Swain, M. R. 2010b, A&A, 511, A75

Berger, J. P. & Segransan, D. 2007, NewAR, 51, 576

Berger, J.-P., Zins, G., Lazareff, B., et al. 2010, in Society of Photo-Optical Instrumentation Engineers (SPIE) Conference Series, Vol. 7734, Society of Photo-Optical Instrumentation Engineers (SPIE) Conference Series

Bergin, E. A. & Tafalla, M. 2007, ARA&A, 45, 339

Bertero, M., Boccacci, P., La Camera, A., Olivieri, C., & Carbillet, M. 2011, Inverse Problems, 27, 113001

Beuther, H., Linz, H., & Henning, T. 2012, A&A, 543, A88

Blaauw, A. 1991, in NATO ASIC Proc. 342: The Physics of Star Formation and Early Stellar Evolution, ed. C. J. Lada & N. D. Kylafis, 125

Blitz, L., Fukui, Y., Kawamura, A., et al. 2007, Protostars and Planets V, 81

Bodenheimer, P. H. 2011, Principles of Star Formation, Astronomy and Astrophysics Library, Springer-Verlag Berlin Heidelberg, 2011

Bonnell, I. A. 2000, in ESA Special Publication, Vol. 445, Star Formation from the Small to the Large Scale, ed. F. Favata, A. Kaas, & A. Wilson, 273

Bonnell, I. A. 2005, in Astrophysics and Space Science Library, Vol. 327, The Initial Mass Function 50 Years Later, ed. E. Corbelli, F. Palla, & H. Zinnecker, 425

Bonnell, I. A. & Bate, M. R. 2005, MNRAS, 362, 915

Bonnell, I. A. & Bate, M. R. 2006, MNRAS, 370, 488

Bonnell, I. A., Bate, M. R., & Zinnecker, H. 1998, MNRAS, 298, 93

Bonnell, I. A. & Smith, R. J. 2011, in IAU Symposium, Vol. 270, Computational Star Formation, ed. J. Alves, B. G. Elmegreen, J. M. Girart, & V. Trimble, 57–64

Born, M. & Wolf, E. 1980, Principles of Optics Electromagnetic Theory of Propagation, Interference and Diffraction of Light, Pergamon Press, 1980

Boss, A. P. & Keiser, S. A. 2012, ArXiv e-prints, 1207.4993

Bossi, M., Gaspani, A., Scardia, M., & Tadini, M. 1989, A&A, 222, 117

Calvet, N., Muzerolle, J., Briceño, C., et al. 2004, AJ, 128, 1294

Carrasco-González, C., Galván-Madrid, R., Anglada, G., et al. 2012, ApJ, 752, L29

Casasola, V. & Brand, J. 2012, Memorie della Societa Astronomica Italiana Supplementi, 19, 330

Chandrasekhar, S. 1960, Radiative transfer, New York: Dover, 1960

Chelli, A., Utrera, O. H., & Duvert, G. 2009, A&A, 502, 705

Chen, H., Myers, P. C., Ladd, E. F., & Wood, D. O. S. 1995, ApJ, 445, 377

Chesneau, O. 2007, New Astronomy Reviews, 51, 666

Chiang, E. I. & Goldreich, P. 1997, ApJ, 490, 368

Chini, R., Hoffmeister, V. H., Nasseri, A., Stahl, O., & Zinnecker, H. 2012, ArXiv e-prints

Chini, R., Kruegel, E., & Kreysa, E. 1986, A&A, 167, 315

Clark, P. C. 2010, Highlights of Astronomy, 15, 771

Close, L. M., Puglisi, A., Males, J. R., et al. 2012, ApJ, 749, 180

Cohen, D. H., Cassinelli, J. P., & Waldron, W. L. 1997, ApJ, 488, 397

Cohen, M., Walker, R. G., Carter, B., et al. 1999, AJ, 117, 1864

Colavita, M. M. 1999, PASP, 111, 111

Commercon, B., Launhardt, R., Dullemond, C. P., & Henning, T. 2012, ArXiv e-prints, 1207.0656

Cox, D. P. 2005, ARA&A, 43, 337

Crampton, D. & Fisher, W. A. 1974, Publications of the Dominion Astrophysical Observatory Victoria, 14, 283

Cunningham, A., Krumholz, M. R., Klein, R. I., & McKee, C. F. 2009, in American Astronomical Society Meeting Abstracts 214, 604.05

Cunningham, A. J., Klein, R. I., Krumholz, M. R., & McKee, C. F. 2011, ApJ, 740, 107

Da Rio, N., Robberto, M., Hillenbrand, L. A., Henning, T., & Stassun, K. G. 2012, ApJ, 748, 14

Da Rio, N., Robberto, M., Soderblom, D. R., et al. 2010, ApJ, 722, 1092

Dapp, W. B., Basu, S., & Kunz, M. W. 2012, A&A, 541, A35

de Bruijne, J. H. J. 1999, MNRAS, 310, 585

de Wit, W. J., Hoare, M. G., Fujiyoshi, T., et al. 2009, A&A, 494, 157

de Wit, W. J., Hoare, M. G., Oudmaijer, R. D., & Lumsden, S. L. 2010, A&A, 515, A45

de Wit, W. J., Hoare, M. G., Oudmaijer, R. D., & Mottram, J. C. 2007, ApJ, 671, L169

de Zeeuw, P. T., Hoogerwerf, R., de Bruijne, J. H. J., Brown, A. G. A., & Blaauw, A. 1999, AJ, 117, 354

Diolaiti, E., Bendinelli, O., Bonaccini, D., et al. 2000, A&AS, 147, 335

Donehew, B. & Brittain, S. 2011, AJ, 141, 46

Draine, B. T. 2009, in EAS Publications Series, Vol. 35, EAS Publications Series, ed. F. Boulanger, C. Joblin, A. Jones, & S. Madden, 245–268

Draine, B. T. & Lee, H. M. 1984, ApJ, 285, 89

Drew, J. E., Busfield, G., Hoare, M. G., et al. 1997, MNRAS, 286, 538

Duarte-Cabral, A., Dobbs, C. L., Peretto, N., & Fuller, G. A. 2011, A&A, 528, A50

Duchêne, G., Delgado-Donate, E., Haisch, Jr., K. E., Loinard, L., & Rodríguez, L. F. 2007, Protostars and Planets V, 379

Dullemond, C. P. & Dominik, C. 2004, A&A, 417, 159

Dullemond, C. P., Dominik, C., & Natta, A. 2001, ApJ, 560, 957

Dullemond, C. P., Hollenbach, D., Kamp, I., & D'Alessio, P. 2007, Protostars and Planets V, 555

Dullemond, C. P. & Monnier, J. D. 2010, ARA&A, 48, 205

Dunham, M. M., Evans, II, N. J., Terebey, S., Dullemond, C. P., & Young, C. H. 2010, ApJ, 710, 470

Duquennoy, A. & Mayor, M. 1991, A&A, 248, 485

Eggleton, P. P. & Tokovinin, A. A. 2008, MNRAS, 389, 869

Eisner, J. A. 2007, Nature, 447, 562

Eisner, J. A., Chiang, E. I., Lane, B. F., & Akeson, R. L. 2007, ApJ, 657, 347

Eisner, J. A., Lane, B. F., Hillenbrand, L. A., Akeson, R. L., & Sargent, A. I. 2004, ApJ, 613, 1049

Eisner, J. A., Monnier, J. D., Woillez, J., et al. 2010, ApJ, 718, 774

Elmegreen, B. G. 2011, in EAS Publications Series, Vol. 51, EAS Publications Series, ed. C. Charbonnel & T. Montmerle, 45–58

Evans, N. R., DeGioia-Eastwood, K., Gagné, M., et al. 2011, ApJS, 194, 13

Fallscheer, C., Beuther, H., Sauter, J., Wolf, S., & Zhang, Q. 2011, ApJ, 729, 66

Favata, F. & Micela, G. 2003, Space Sci. Rev., 108, 577

Follert, R., Linz, H., Stecklum, B., et al. 2010, A&A, 522, A17

Frau, P., Girart, J. M., Beltran, M. T., et al. 2012, ArXiv e-prints, 1207.3310

Fried, D. L. 1965, Journal of the Optical Society of America (1917-1983), 55, 1427

Fuente, A., Rizzo, J. R., Caselli, P., Bachiller, R., & Henkel, C. 2005, A&A, 433, 535

Fukui, Y. & Kawamura, A. 2010, ARA&A, 48, 547

Gai, M., Menardi, S., Cesare, S., et al. 2004, in Society of Photo-Optical Instrumentation Engineers (SPIE) Conference Series, Vol. 5491, Society of Photo-Optical Instrumentation Engineers (SPIE) Conference Series, ed. W. A. Traub, 528

Gavilan, L., Lemaire, J. L., & Vidali, G. 2012, MNRAS, 3377

Gibb, E. L., Whittet, D. C. B., Boogert, A. C. A., & Tielens, A. G. G. M. 2004, ApJS, 151, 35

Gitton, P. B., Leveque, S. A., Avila, G., & Phan Duc, T. 2004, in Society of Photo-Optical Instrumentation Engineers (SPIE) Conference Series, Vol. 5491, Society of Photo-Optical Instrumentation Engineers (SPIE) Conference Series, ed. W. A. Traub, 944

Glindemann, A. 2011, Principles of Stellar Interferometry, Astronomy and Astrophysics Library,Springer-Verlag Berlin Heidelberg, 2011

Glindemann, A., Ballester, P., Bauvir, B., et al. 2001a, The Messenger, 106, 1

Glindemann, A., Bauvir, B., Delplancke, F., et al. 2001b, The Messenger, 104, 2

Goodwin, S. P., Kroupa, P., Goodman, A., & Burkert, A. 2007, Protostars and Planets V, 133

Grellmann, R., Ratzka, T., Kraus, S., et al. 2011, A&A, 532, A109

Gritschneder, M., Lin, D. N. C., Murray, S. D., & Burkert, A. 2011, in Astronomical Society of the Pacific Conference Series, Vol. 451, Astronomical Society of the Pacific Conference Series, ed. S. Qain, K. Leung, L. Zhu, & S. Kwok, 199

Güdel, M. & Nazé, Y. 2009, A&A Rev., 17, 309

Guertler, J., Henning, T., Koempe, C., et al. 1996, A&A, 315, L189

Harmanec, P. 1987, Bulletin of the Astronomical Institutes of Czechoslovakia, 38, 283

Hartkopf, W. I., Mason, B. D., McAlister, H. A., et al. 2000, AJ, 119, 3084

Hartkopf, W. I., McAlister, H. A., Mason, B. D., et al. 1997, AJ, 114, 1639

Hartkopf, W. I., Tokovinin, A., & Mason, B. D. 2012, AJ, 143, 42

Harvey, P. M., Campbell, M. F., & Hoffmann, W. F. 1977, ApJ, 215, 151

Hennebelle, P. 2012, ArXiv e-prints, 1204.5063

Henning, T. 2010, ARA&A, 48, 21

Herbig, G. H., Andrews, S. M., & Dahm, S. E. 2004, AJ, 128, 1233

Herbig, G. H. & Griffin, R. F. 2006, AJ, 132, 1763

Herbst, E. & van Dishoeck, E. F. 2009, ARA&A, 47, 427

Hernández, J., Calvet, N., Briceño, C., Hartmann, L., & Berlind, P. 2004, AJ, 127, 1682

Hill, J. M. 2010, Appl. Opt., 49, D115

Hillenbrand, L. A. 1997, AJ, 113, 1733

Hillenbrand, L. A., Strom, S. E., Calvet, N., et al. 1998, AJ, 116, 1816

Hillenbrand, L. A., Strom, S. E., Vrba, F. J., & Keene, J. 1992, ApJ, 397, 613

Högbom, J. A. 1974, A&AS, 15, 417

Hsu, W., Hartmann, L., Heitsch, F., & Gómez, G. C. 2011, in Astronomical Society of the Pacific Conference Series, Vol. 440, UP2010: Have Observations Revealed a Variable Upper End of the Initial Mass Function?, ed. M. Treyer, T. Wyder, J. Neill, M. Seibert, & J. Lee, 107

Ivanescu, L., Arsenault, R., Fedrigo, E., et al. 2004, in Society of Photo-Optical Instrumentation Engineers (SPIE) Conference Series, Vol. 5490, Society of Photo-Optical Instrumentation Engineers (SPIE) Conference Series, ed. D. Bonaccini Calia, B. L. Ellerbroek, & R. Ragazzoni, 1534–1545

Jackson, J. D. 1962, Classical Electrodynamics, New York, Wiley, 1962

Jeans, J. H. 1902, Royal Society of London Philosophical Transactions Series A, 199, 1

Jeffries, R. D., Littlefair, S. P., Naylor, T., & Mayne, N. J. 2011, MNRAS, 418, 1948

Jennison, R. C. 1958, MNRAS, 118, 276

Jones, B. F. & Walker, M. F. 1988, AJ, 95, 1755

Kastner, J. H., Weintraub, D. A., & Aspin, C. 1992, ApJ, 389, 357

Kenyon, S. J. & Hartmann, L. 1987, ApJ, 323, 714

King, R. R., Parker, R. J., Patience, J., & Goodwin, S. P. 2012, MNRAS, 421, 2025

Köhler, R. & Jaffe, W. 2008, in The Power of Optical/IR Interferometry: Recent Scientific Results and 2nd Generation (Springer, Heidelberg), ed. A. Richichi, F. Delplancke, F. Paresce, & A. Chelli, 569

Köhler, R. & Leinert, C. 1998, A&A, 331, 977

Köhler, R., Petr-Gotzens, M. G., McCaughrean, M. J., et al. 2006, A&A, 458, 461

Köhler, R., Ratzka, T., Herbst, T. M., & Kasper, M. 2008, A&A, 482, 929

Köhler, R., Ratzka, T., & Leinert, C. 2012, A&A, 541, A29

Kolmogorov, A. 1941, Akademiia Nauk SSSR Doklady, 30, 301

Kolmogorov, A. N. 1991, Royal Society of London Proceedings Series A, 434, 9

Kouwenhoven, M. B. N., Brown, A. G. A., Portegies Zwart, S. F., & Kaper, L. 2007, A&A, 474, 77

Kouwenhoven, M. B. N., Brown, A. G. A., Zinnecker, H., Kaper, L., & Portegies Zwart, S. F. 2005, A&A, 430, 137

Kraus, S. 2007, PhD thesis, Max-Planck-Institut für Radioastronomie, Auf dem Hügel 69, Bonn, Germany

Kraus, S., Balega, Y. Y., Berger, J.-P., et al. 2007, A&A, 466, 649

Kraus, S., Hofmann, K., Menten, K. M., et al. 2010, Nature, 466, 339

Kraus, S., Hofmann, K.-H., Benisty, M., et al. 2008a, A&A, 489, 1157

Kraus, S., Preibisch, T., & Ohnaka, K. 2008b, ApJ, 676, 490

Kraus, S., Weigelt, G., Balega, Y. Y., et al. 2009, A&A, 497, 195

Kroupa, P. 2001, MNRAS, 322, 231

Krumholz, M. R. & Bonnell, I. A. 2007, ArXiv e-prints, 0712.0828

Krumholz, M. R., Klein, R. I., McKee, C. F., Offner, S. S. R., & Cunningham, A. J. 2009, Science, 323, 754

Kudritzki, R.-P. & Puls, J. 2000, ARA&A, 38, 613

Kuiper, R., Klahr, H., Beuther, H., & Henning, T. 2010, ApJ, 722, 1556

Lada, C. J. 1987, in IAU Symposium, Vol. 115, Star Forming Regions, ed. M. Peimbert & J. Jugaku, 1–17

Lada, C. J. 2006, ApJ, 640, L63

Lawson, P. R., ed. 2000, Principles of Long Baseline Stellar Interferometry

Lehmann, H., Vitrichenko, E., Bychkov, V., Bychkova, L., & Klochkova, V. 2010, A&A, 514, A34

Leinert, C., Graser, U., Przygodda, F., et al. 2003, Ap&SS, 286, 73

Leinert, C., van Boekel, R., Waters, L. B. F. M., et al. 2004, A&A, 423, 537

Lester, D. F., Harvey, P. M., Joy, M., & Ellis, Jr., H. B. 1986, ApJ, 309, 80

Levato, H., Malaroda, S., Morrell, N., & Solivella, G. 1987, ApJS, 64, 487

Li, H.-b., Houde, M., Lai, S.-p., & Sridharan, T. K. 2010, ApJ, 718, 905

Lin, M.-K., Krumholz, M. R., & Kratter, K. M. 2011, MNRAS, 416, 580

Linz, H., Henning, T., Feldt, M., et al. 2009, A&A, 505, 655

Lopez, B., Wolf, S., Lagarde, S., et al. 2006, in Society of Photo-Optical Instrumentation Engineers (SPIE) Conference Series, Vol. 6268, Society of Photo-Optical Instrumentation Engineers (SPIE) Conference Series

Lord, ed. 1992, A New Software Tool for Computing Earth's Atmospheric, NASA technical memorandum 103957

Maeder, A. & Behrend, R. 2002, in Astro. Society of the Pacific Conference, Vol. 267, Hot Star Workshop III: The Earliest Phases of Massive Star Birth, ed. P. Crowther, 179

Malbet, F., Benisty, M., de Wit, W.-J., et al. 2007, A&A, 464, 43

Malbet, F., Duvert, G., Millour, F. A., et al. 2010, in Society of Photo-Optical Instrumentation Engineers (SPIE) Conference Series, Vol. 7734, Society of Photo-Optical Instrumentation Engineers (SPIE) Conference Series

Malbet, F., Lachaume, R., Berger, J., et al. 2005, A&A, 437, 627

Mason, B. D., Hartkopf, W. I., Gies, D. R., Henry, T. J., & Helsel, J. W. 2009, AJ, 137, 3358

Mathieu, R. D. & Zinnecker, H. 2000, PASP, 112, 1512

Mathis, J. S., Rumpl, W., & Nordsieck, K. H. 1977, ApJ, 217, 425

McAlister, H., Hartkopf, W. I., & Franz, O. G. 1990, AJ, 99, 965

McAlister, H. A., Hartkopf, W. I., Hutter, D. J., & Franz, O. G. 1987, AJ, 93, 688

McAlister, H. A., Mason, B. D., Hartkopf, W. I., & Shara, M. M. 1993, AJ, 106, 1639

McCaughrean, M. J. & Stauffer, J. R. 1994, AJ, 108, 1382

McKee, C. F. & Ostriker, E. C. 2007, ARA&A, 45, 565

Megeath, S. T., Flaherty, K. M., Hora, J., et al. 2005, in IAU Symposium, Vol. 227, Massive Star Birth: A Crossroads of Astrophysics, ed. R. Cesaroni, M. Felli, E. Churchwell, & M. Walmsley, 383–388

Men'shchikov, A. B. & Henning, T. 1997, A&A, 318, 879

Menten, K. M., Reid, M. J., Forbrich, J., & Brunthaler, A. 2007, A&A, 474, 515

Mewe, R., Raassen, A. J. J., Cassinelli, J. P., et al. 2003, Advances in Space Research, 32, 1167

Michelson, A. A. 1920, ApJ, 51, 257

Monnier, J. D. 2003, Reports on Progress in Physics, 66, 789

Monnier, J. D. & Millan-Gabet, R. 2002, ApJ, 579, 694

Monnier, J. D., Millan-Gabet, R., Billmeier, R., et al. 2005, ApJ, 624, 832

Monnier, J. D., Tuthill, P. G., Ireland, M., et al. 2009, ApJ, 700, 491

Morrell, N. & Levato, H. 1991, ApJS, 75, 965

Muench, A., Getman, K., Hillenbrand, L., & Preibisch, T. 2008, Star Formation in the Orion Nebula I: Stellar Content, ed. B. Reipurth, 483

Murakawa, K. 2010, A&A, 522, A46

Murakawa, K., Preibisch, T., Kraus, S., et al. 2008, A&A, 488, L75

Muzerolle, J., Hartmann, L., & Calvet, N. 1998, AJ, 116, 2965

Najita, J. R., Doppmann, G. W., Carr, J. S., Graham, J. R., & Eisner, J. A. 2009, ApJ, 691, 738

Nakano, M., Sugitani, K., & Morita, K. 2003, PASJ, 55, 1

Nakano, T. 1989, ApJ, 345, 464

Natta, A., Prusti, T., Neri, R., et al. 2001, A&A, 371, 186

North, J. R., Davis, J., Tuthill, P. G., Tango, W. J., & Robertson, J. G. 2007, MNRAS, 380, 1276

Offner, S., Kratter, K. M., Matzner, C. D., Krumholz, M. R., & Klein, R. I. 2011, in Bulletin of the American Astronomical Society, Vol. 43, American Astronomical Society Meeting Abstracts 217, 258

Offner, S. S. R., Robitaille, T. P., Hansen, C. E., McKee, C. F., & Klein, R. I. 2012, ApJ, 753, 98

Osorio, M., Anglada, G., Lizano, S., & D'Alessio, P. 2009, ApJ, 694, 29

Padgett, D. L., Strom, S. E., & Ghez, A. 1997, ApJ, 477, 705

Patience, J., Zavala, R. T., Prato, L., et al. 2008, ApJ, 674, L97

Peck, A. 2012, in American Astronomical Society Meeting Abstracts, Vol. 219, American Astronomical Society Meeting Abstracts, 309.01

Petr, M. G., Coudé du Foresto, V., Beckwith, S. V. W., Richichi, A., & McCaughrean, M. J. 1998, ApJ, 500, 825

Petrov, R. G., Malbet, F., Weigelt, G., et al. 2007, A&A, 464, 1

Pickett, B. K., Mejía, A. C., Durisen, R. H., et al. 2003, ApJ, 590, 1060

Pinte, C., Ménard, F., Berger, J. P., Benisty, M., & Malbet, F. 2008, ApJ, 673, L63

Povich, M. S. 2012, ArXiv e-prints, 1202.0791

Pradas, J. & Kerp, J. 2003, Astronomische Nachrichten, 324, 151

Preibisch, T., Balega, Y., Hofmann, K.-H., Weigelt, G., & Zinnecker, H. 1999, New Astronomy, 4, 531

Preibisch, T., Brown, A. G. A., Bridges, T., Guenther, E., & Zinnecker, H. 2002, AJ, 124, 404

Preibisch, T., Kim, Y.-C., Favata, F., et al. 2005, ApJS, 160, 401

Preibisch, T. & Mamajek, E. 2008, The Nearest OB Association: Scorpius-Centaurus (Sco OB2), ed. Reipurth, B., 235

Preibisch, T. & Zinnecker, H. 1999, AJ, 117, 2381

Press, W. H., Teukolsky, S. A., Vetterling, W. T., & Flannery, B. P. 1992, Numerical Recipes in C, 2nd edn. (Cambridge, UK: Cambridge University Press)

Raghavan, D., McAlister, H. A., Henry, T. J., et al. 2010a, ApJS, 190, 1

Raghavan, D., McAlister, H. A., Henry, T. J., et al. 2010b, ApJS, 190, 1

Ratzka, T. 2005, PhD thesis, Max-Planck-Institute for Astronomy, Königstuhl 17, 69117 Heidelberg, Germany

Ratzka, T., Schegerer, A. A., Leinert, C., et al. 2009, A&A, 502, 623

Reipurth, B. 2008, Handbook of Star Forming Regions, Volume I: The Northern Sky

Robitaille, T. P., Whitney, B. A., Indebetouw, R., & Wood, K. 2007, ApJS, 169, 328

Robitaille, T. P., Whitney, B. A., Indebetouw, R., Wood, K., & Denzmore, P. 2006, ApJS, 167, 256

Roddier, F. 1981, Progress in optics. Volume 19. Amsterdam, North-Holland Publishing Co., 1981, p. 281-376., 19, 281

Rosen, A. L., Krumholz, M. R., & Ramirez-Ruiz, E. 2012, ApJ, 748, 97

Salpeter, E. E. 1955, ApJ, 121, 161

Sana, H., de Mink, S. E., de Koter, A., et al. 2012, ArXiv e-prints, 1207.6397

Sargent, A. I., van Duinen, R. J., Nordh, H. L., et al. 1984, A&A, 135, 377

Savage, B. D. & Mathis, J. S. 1979, ARA&A, 17, 73

Schegerer, A. A., Wolf, S., Hummel, C. A., Quanz, S. P., & Richichi, A. 2009, A&A, 502, 367

Schertl, D., Balega, Y. Y., Preibisch, T., & Weigelt, G. 2003, A&A, 402, 267

Schmitt, J. H. M. M., Kahabka, P., Stauffer, J., & Piters, A. J. M. 1993, A&A, 277, 114

Schreyer, K., Helmich, F. P., van Dishoeck, E. F., & Henning, T. 1997, A&A, 326, 347

Schreyer, K., Semenov, D., Henning, T., & Forbrich, J. 2006, ApJ, 637, L129

Schreyer, K., Stecklum, B., Linz, H., & Henning, T. 2003, ApJ, 599, 335

Schulz, N. S. 2005, From Dust To Stars Studies of the Formation and Early Evolution of Stars, Springer

Schwartz, P. R., Thronson, Jr., H. A., Odenwald, S. F., et al. 1985, ApJ, 292, 231

Shaklan, S. & Roddier, F. 1988, Appl. Opt., 27, 2334

Sheth, K. 2012, in American Astronomical Society Meeting Abstracts, Vol. 220, American Astronomical Society Meeting Abstracts, 517.01

Shevchenko, V. S. & Yakubov, S. D. 1989, Soviet Ast., 33, 370

Siess, L., Dufour, E., & Forestini, M. 2000, A&A, 358, 593

Simon, M., Close, L. M., & Beck, T. L. 1999, AJ, 117, 1375

Simón-Díaz, S., Herrero, A., Esteban, C., & Najarro, F. 2006, A&A, 448, 351

Slesnick, C. L., Hillenbrand, L. A., & Carpenter, J. M. 2008, ApJ, 688, 377

Sloan, G. C., Kraemer, K. E., Price, S. D., & Shipman, R. F. 2003, ApJS, 147, 379

Snow, T. P. & McCall, B. J. 2006, ARA&A, 44, 367

Spitzer, L. 1978, New York Wiley-Interscience, 1978. 333 p.

Stahler, S. W. & Palla, F. 2005, The Formation of Stars, Wiley-VCH , January 2005

Stehle, R. & Spruit, H. C. 2001, MNRAS, 323, 587

Stelzer, B., Flaccomio, E., Montmerle, T., et al. 2005a, ApJS, 160, 557

Stelzer, B., Huélamo, N., Hubrig, S., et al. 2005b, in ESA Special Publication, Vol. 560, 13th Cambridge Workshop on Cool Stars, Stellar Systems and the Sun, ed. F. Favata, G. A. J. Hussain, & B. Battrick, 213

Stelzer, B., Micela, G., Hamaguchi, K., & Schmitt, J. H. M. M. 2006, A&A, 457, 223

Stone, J. M. & Pringle, J. E. 2001, MNRAS, 322, 461

Tachihara, K., Saigo, K., Higuchi, A. E., et al. 2012, ApJ, 754, 95

Tallon-Bosc, I., Tallon, M., Thiébaut, E., et al. 2008, in Society of Photo-Optical Instrumentation Engineers (SPIE) Conference Series, Vol. 7013, Society of Photo-Optical Instrumentation Engineers (SPIE) Conference Series

Tatulli, E., Malbet, F., Ménard, F., et al. 2008, A&A, 489, 1151

Tatulli, E., Millour, F., Chelli, A., et al. 2007, A&A, 464, 29

Taylor, G. B., Carilli, C. L., & Perley, R. A., eds. 1999, Astronomical Society of the Pacific Conference Series, Vol. 180, Synthesis Imaging in Radio Astronomy II

Thamm, E., Steinacker, J., & Henning, T. 1994, A&A, 287, 493

Thiebaut, E., Bouvier, J., Blazit, A., et al. 1995, A&A, 303, 795

Thompson, A. R., Moran, J. M., & Swenson, Jr., G. W. 2001, Interferometry and synthesis in radio astronomy 2nd ed New York Wiley

Thompson, R. I., Corbin, M. R., Young, E., & Schneider, G. 1998, ApJ, 492, L177

Thompson, R. I. & Tokunaga, A. T. 1978, ApJ, 226, 119

Tokovinin, A. 2012, AJ, 144, 56

Tokovinin, A., Mason, B. D., & Hartkopf, W. I. 2010, AJ, 139, 743

Tokovinin, A. A. 1997, A&AS, 124, 75

Townsley, L. K., Broos, P. S., Corcoran, M. F., et al. 2011, ApJS, 194, 1

Tristram, K. R. W. 2007, PhD thesis, Max-Planck-Institut für Astronomie, Königstuhl 17, 69117 Heidelberg, Germany

van Boekel, R. 2008, Journal of Physics Conference Series, 131, 012023

van Boekel, R., Ábrahám, P., Correia, S., et al. 2006, in Society of Photo-Optical Instrumentation Engineers (SPIE) Conference Series, Vol. 6268, Society of Photo-Optical Instrumentation Engineers (SPIE) Conference Series

van Boekel, R., Min, M., Leinert, C., et al. 2004, Nature, 432, 479

van den Ancker, M. 2005, in High Resolution Infrared Spectroscopy in Astronomy, ed. H. U. Käufl, R. Siebenmorgen, & A. Moorwood, 309–314

van der Tak, F. F. S., van Dishoeck, E. F., Evans, II, N. J., Bakker, E. J., & Blake, G. A. 1999, ApJ, 522, 991

Varricatt, W. P. 2012, A&A, 540, A59

Vehoff, S., Hummel, C. A., Monnier, J. D., et al. 2010, A&A, 520, A78

Viana Almeida, P., Melo, C., Santos, N. C., et al. 2012, A&A, 539, A62

Ward-Thompson, D., Zylka, R., Mezger, P. G., & Sievers, A. W. 2000, A&A, 355, 1122

Weigelt, G., Balega, Y., Preibisch, T., et al. 1999, A&A, 347, L15

Weigelt, G., Grinin, V. P., Groh, J. H., et al. 2011, A&A, 527, A103

Whitney, B. A., Wood, K., Bjorkman, J. E., & Wolff, M. J. 2003, ApJ, 591, 1049

Wolf, S., Lopez, B., Jaffe, W., et al. 2009, in Science with the VLT in the ELT Era, ed. A. Moorwood, 359

Wolf, S., Malbet, F., Alexander, R., et al. 2012, A&A Rev., 20, 52

Yorke, H. W. & Sonnhalter, C. 2002, ApJ, 569, 846

Young, T. 1802, Philosophical Transactions of the Royal Society of London, 92, 12

Zagury, F. 2012, Astronomische Nachrichten, 333, 160

Zinnecker, H. & Bate, M. R. 2002, in Astronomical Society of the Pacific Conference Series, Vol. 267, Hot Star Workshop III: The Earliest Phases of Massive Star Birth (ASP, San Francisco), ed. P. Crowther, 209

Zinnecker, H. & Yorke, H. W. 2007, ARA&A, 45, 481

Appendix A

Appendix

A.1 Additional material related to Chapt. 3

Table A.1: MIR-sizes of MYSOs and Herbig Be stars

Object	Diameter [AU]	Distance [pc]	Luminosity [$L_\odot$]	Mass [$M_\odot$]	SpT	Reference
NGC 3603 IRS 9A	2177	7000	$2.3{\cdot}10^5$	40		1
W 33A	115-230	3800	$1{\cdot}10^5$	10		2
V376 Cas	23	630	43		B5e	3, 4
MWC 147	19	800	1550	6.6	B6	3, 5, 6
R Mon	75	800	1400	10.4	B0	3, 7, 8
Z CMa	61	1000	2400	16	B	3, 9, 10
MWC 297	14	250	10600	10	B1.5	3, 11, 12
V1685 Cyg	28	980	5890		B3	3, 4
MWC 361	20	440	6600		B2	3, 4
LkHα 234	27	1000	500	5	B7	3, 13, 14
AFGL 490	100	1000	$2{\cdot}10^3$	8-10	B2	3, 15
LkHα 101	49	700	$2\text{-}6{\cdot}10^4$	15	Be	3, 16
S140 IRS 1	122	910	$2{\cdot}10^4$			3, 17, 18
AFGL 2136	240	2000	$2{\cdot}10^4$	>10		3, 19
AFGL 2591	118	1000	$2{\cdot}10^4$	10-15		3, 20
M 17 SW IRS 1	69-84	2100	$5{\cdot}10^3$		B0	21
M8E-IR	30-57	1500	$2{\cdot}10^4$		B0	22
NGC 2264 IRS 1	30-60	913	$1.5\text{-}4.7{\cdot}10^3$	9.5	B0-B2	see Chapt. 3.1, 3.3.1

(1) Vehoff et al. (2010); (2) de Wit et al. (2007); (3) Monnier et al. (2009); (4) Acke & van den Ancker (2004); (5) Kraus et al. (2008b); (6) Hernández et al. (2004); (7) Murakawa et al. (2008); (8) Murakawa (2010); (9) Alonso-Albi et al. (2009); (10) Thiebaut et al. (1995); (11) Acke et al. (2008); (12) Drew et al. (1997); (13) Shevchenko & Yakubov (1989); (14) Fuente et al. (2005); (15) Schreyer et al. (2006); (16) Herbig et al. (2004); (17) Crampton & Fisher (1974); (18) Lester et al. (1986); (19) Kastner et al. (1992); (20) van der Tak et al. (1999); (21) Follert et al. (2010); (22) Linz et al. (2009)

A.2 Additional material related to Chapt. 4

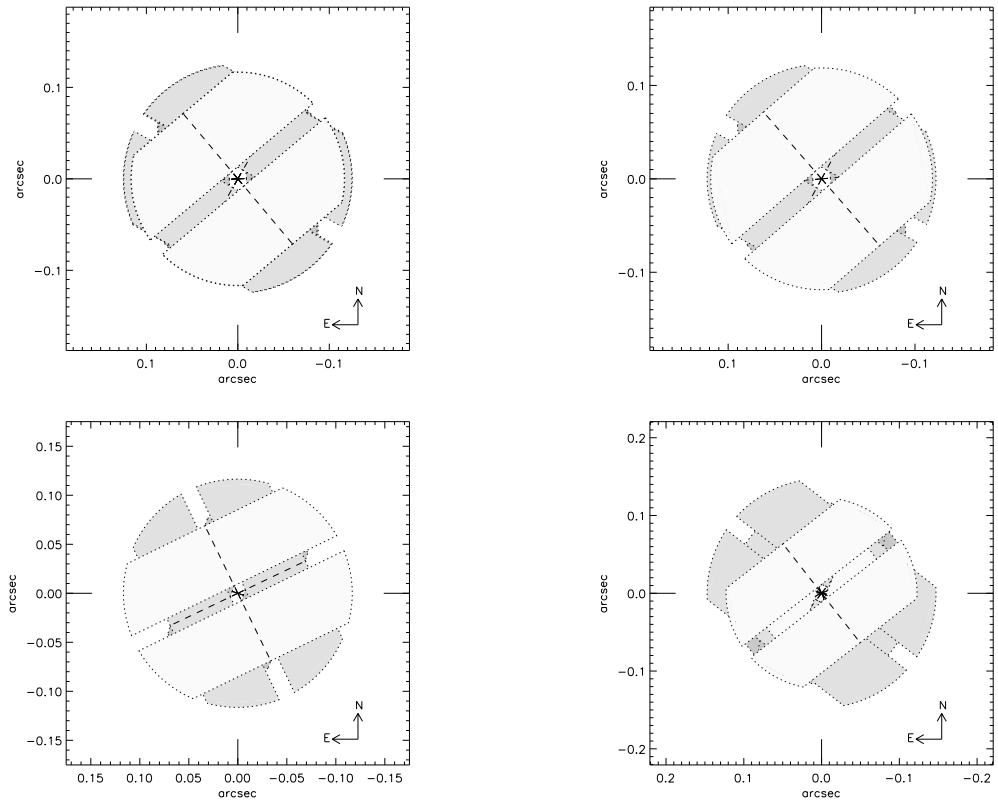

Figure A.1: Coverage of the area around the observed objects, where a binary component within the defined conditions (see Chap. 4.3) can be excluded from the AMBER data. The different colors indicate the areas for the three different baselines and position angles. *Upper Left:* π Sco *Upper Right:* τ Sco *Lower Left:*ω Sco *Lower Right:* χ Oph

Table A.2: Orbital Parameters of the spectroscopic Binary HR 6027 A

Parameter	Value
P [days]	5.5521
T [JD -2400000]	42185.555
ω [°]	267
e	0.11
K [km/s]	26.5
V_0	+4.1
$a \sin i$ [10^6km]	2.01

All values from Batten et al. (1989).

Table A.3: Positions of HR 6027 B and C relative to HR 6027 A

Comp.	Date [°]	PA [°]	Δ PA [″]	Sep. [″]	Δ Sep.	Ref.
C	1988.1658	172.3	0.5	0.056	0.010	3
C	1989.3065	164.8	0.4	0.063	0.008	2
C	2009.2630	162.3	9.0	0.055	0.011	8
C	2010.3589	345.7		0.072		Sect. 4.4.1
C	2011.2892	347.3	0.7	0.075	0.003	9
C	2012.3540	345.8	1.2	0.076	0.0035	7
B	1983.4282	2.0	0.4	1.219	0.008	1
B	1989.3065	1.9	0.4	1.302	0.008	2
B	1990.3468	2.8	0.4	1.304	0.008	3
B	1995.4395	2.0	0.4	1.296	0.008	4
B	1996.1842	2.1	0.4	1.317	0.008	5
B	1996.4196	1.7	0.4	1.306	0.008	5
B	2006.1945	1.6	0.4	1.330	0.008	6

(1) McAlister et al. (1987); (2) McAlister et al. (1990); (3) McAlister et al. (1993); (4) Hartkopf et al. (1997); (5) Hartkopf et al. (2000); (6) Mason et al. (2009); (7) Tokovinin (2012); (8) Tokovinin et al. (2010); (9) Hartkopf et al. (2012)

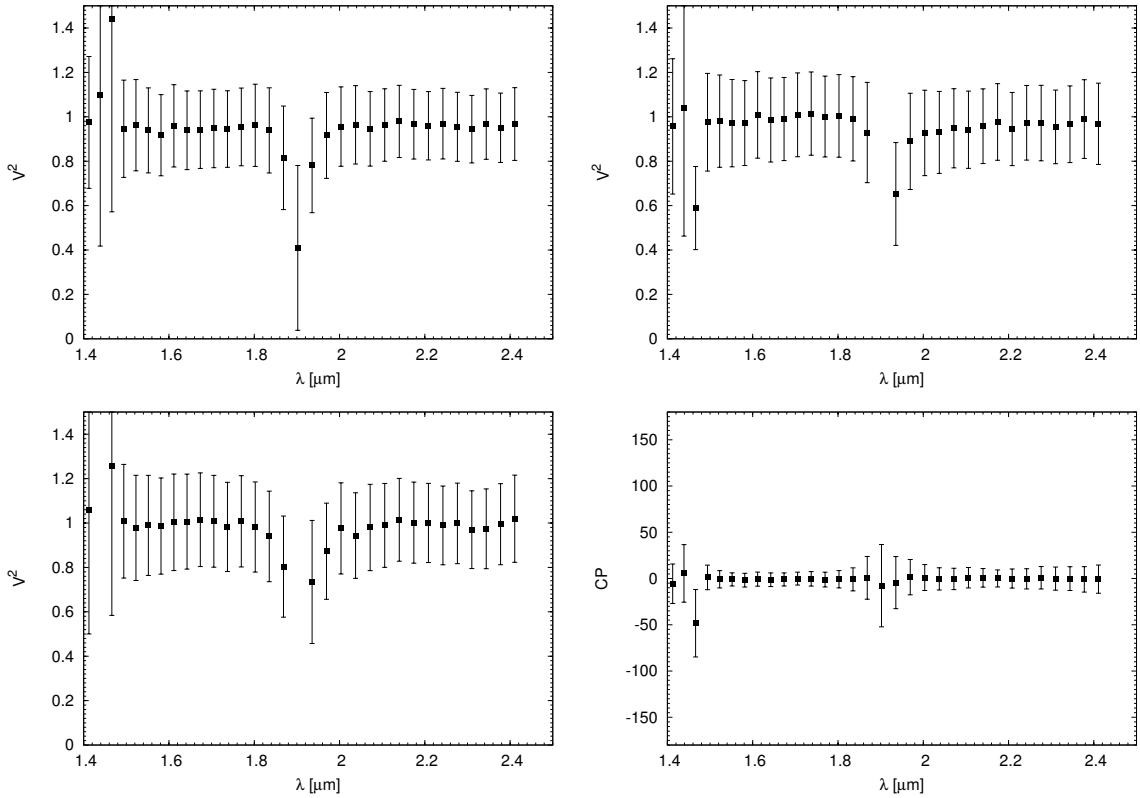

Figure A.2: Visibilities and closure phase of π Sco versus wavelength for the H- and K-band measured with AMBER on 06/05/10.

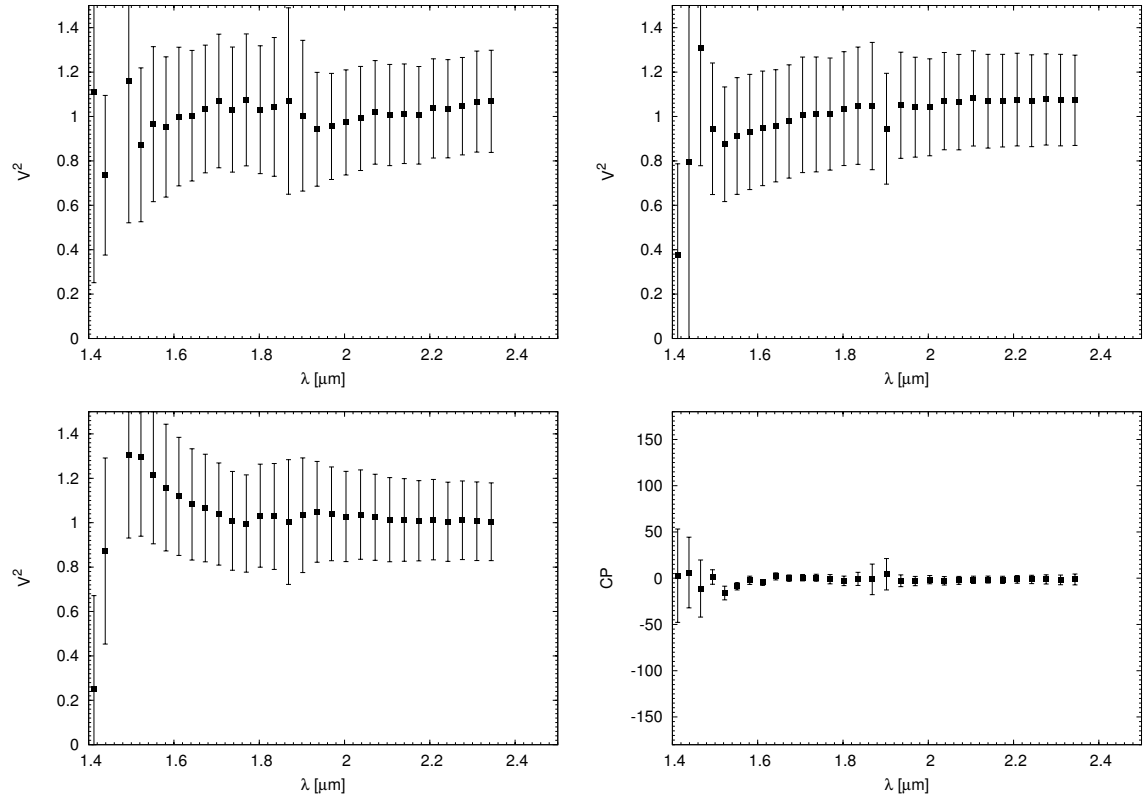

Figure A.3: Visibilities and closure phase of π Sco versus wavelength for the H- and K-band measured with AMBER on 10/05/10.

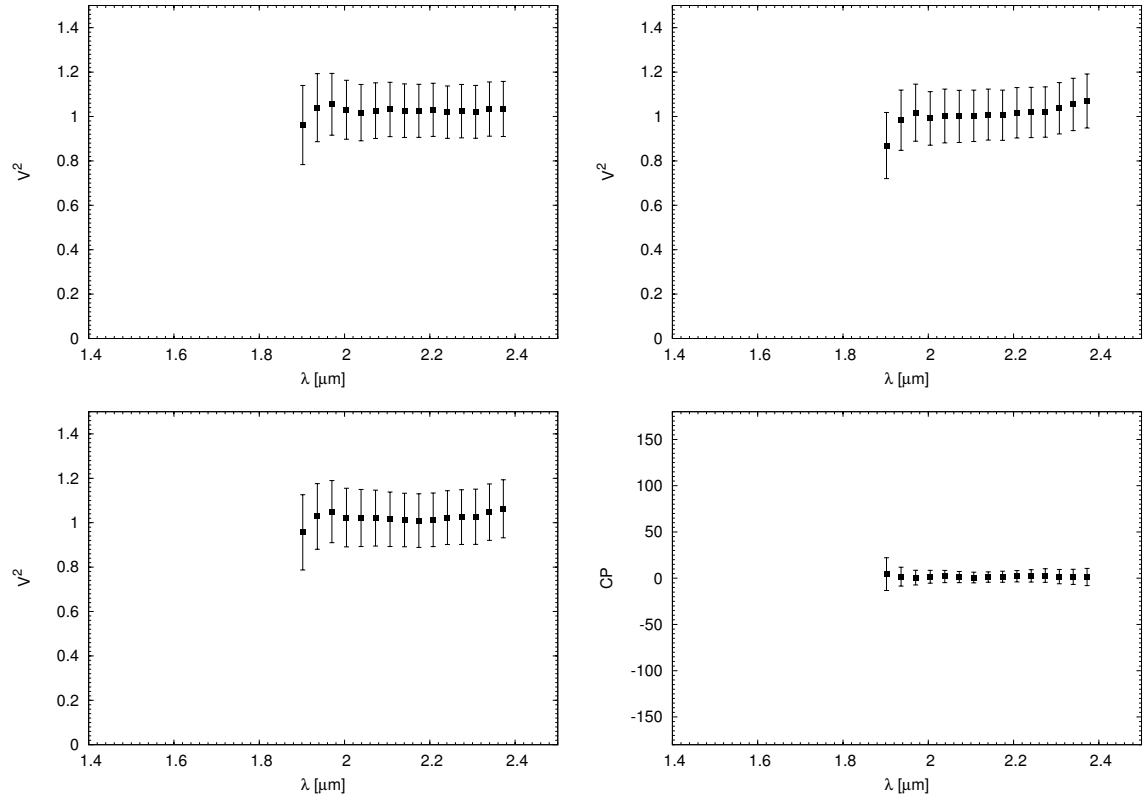

Figure A.4: Visibilities and closure phase of ω Sco versus wavelength for the H- and K-band measured with AMBER on 11/05/10

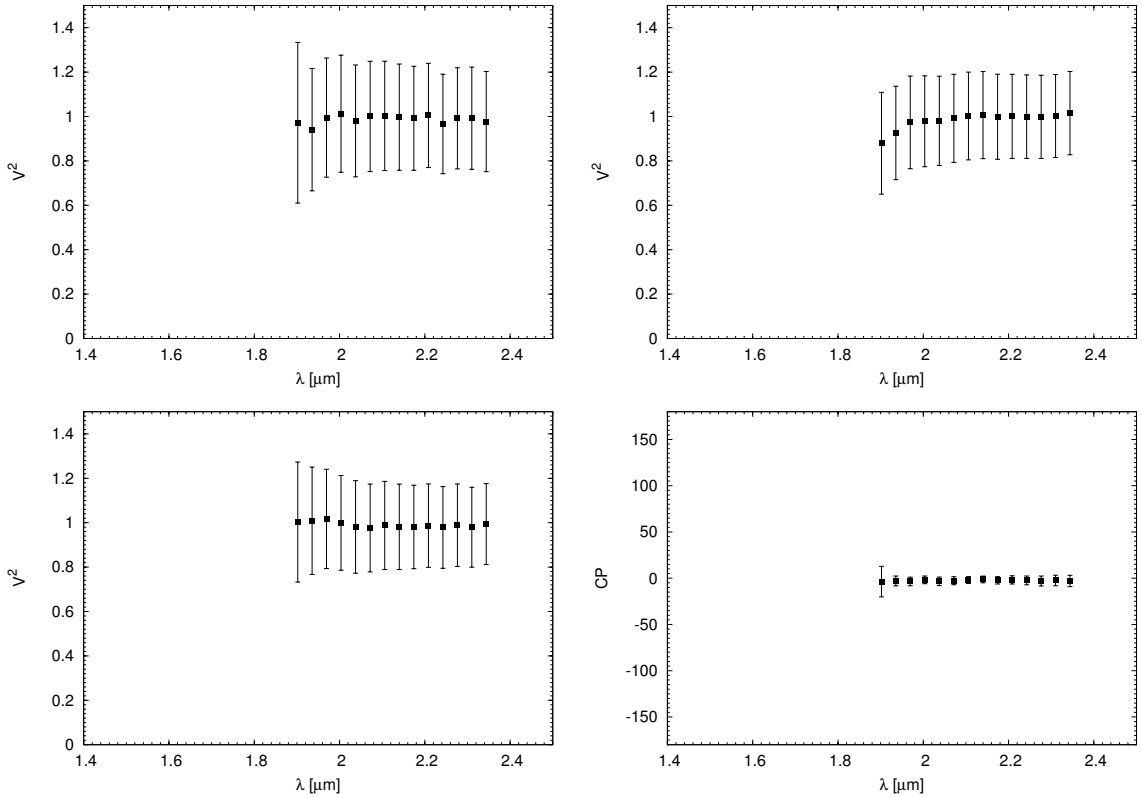

Figure A.5: Visibilities and closure phase of τ Sco versus wavelength for the H- and K-band measured with AMBER on 10/05/10

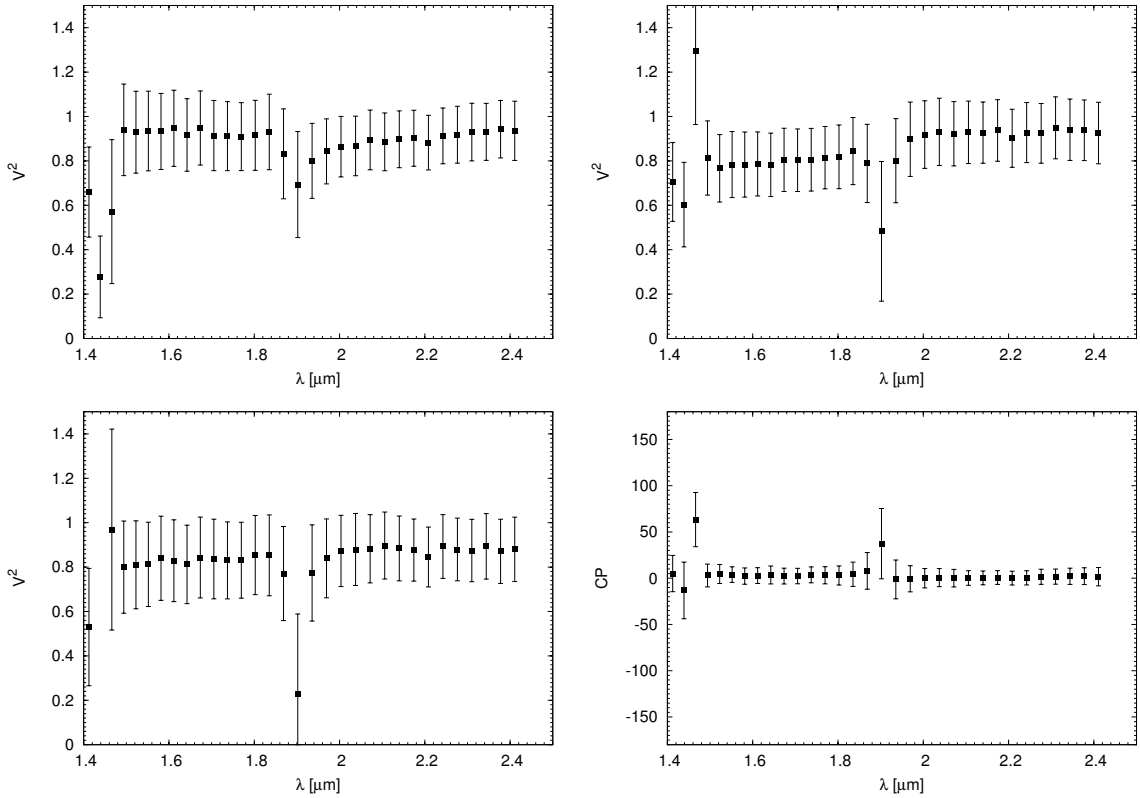

Figure A.6: Visibilities and closure phase of χ Oph versus wavelength for the H- and K-band measured with AMBER on 06/05/10

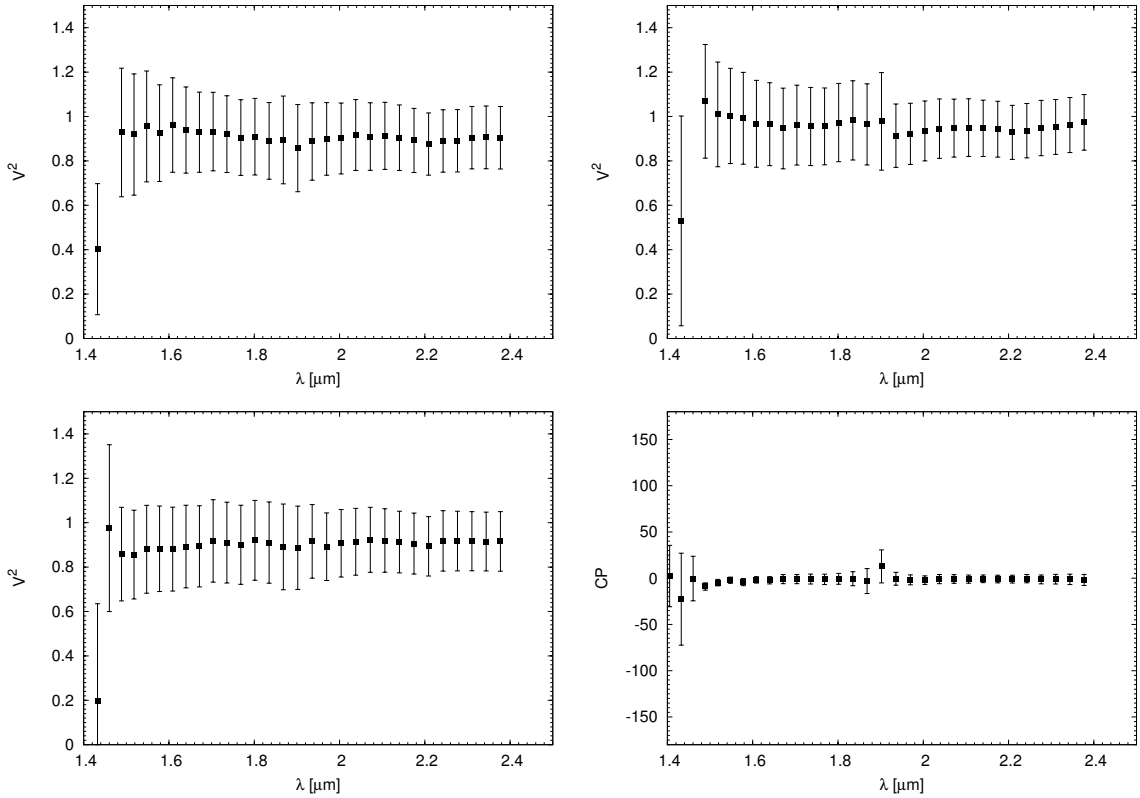

Figure A.7: Visibilities and closure phase of χ Oph versus wavelength for the H- and K-band measured with AMBER on 11/05/10

A.3 Additional material related to Chapt. 5

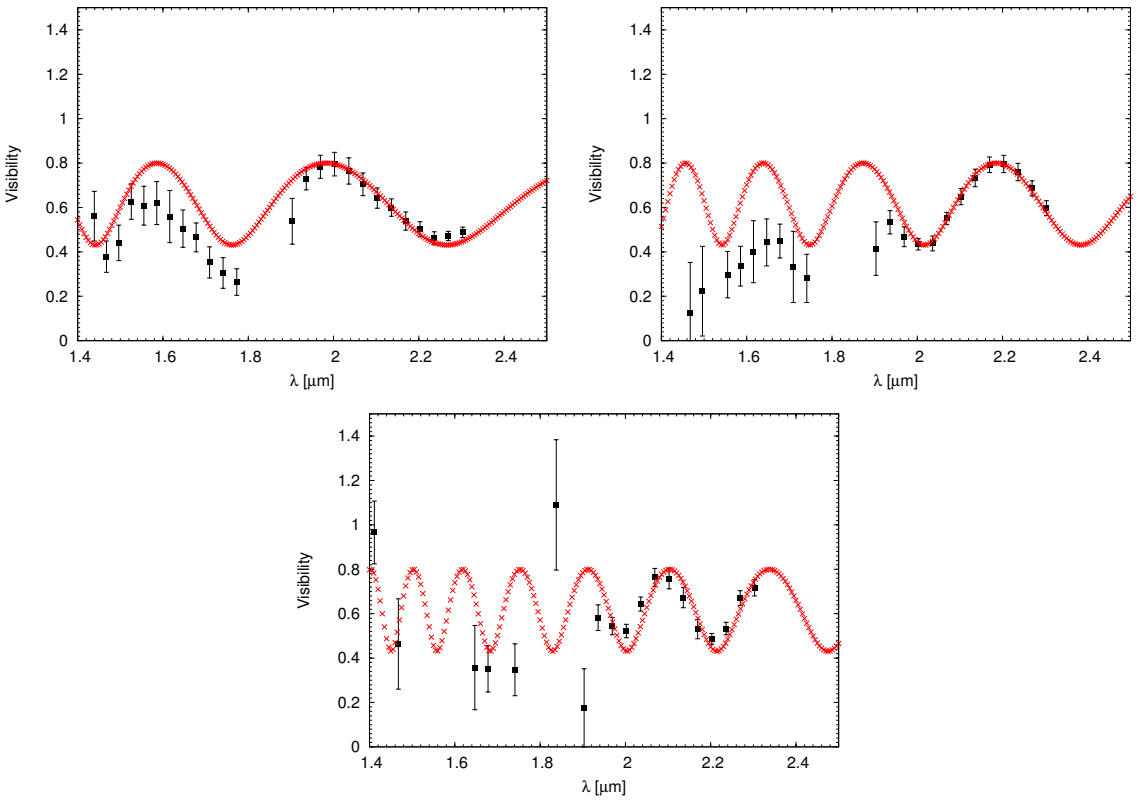

Figure A.8: Visibilities of θ^1 Ori C observed on 05/10/2010.

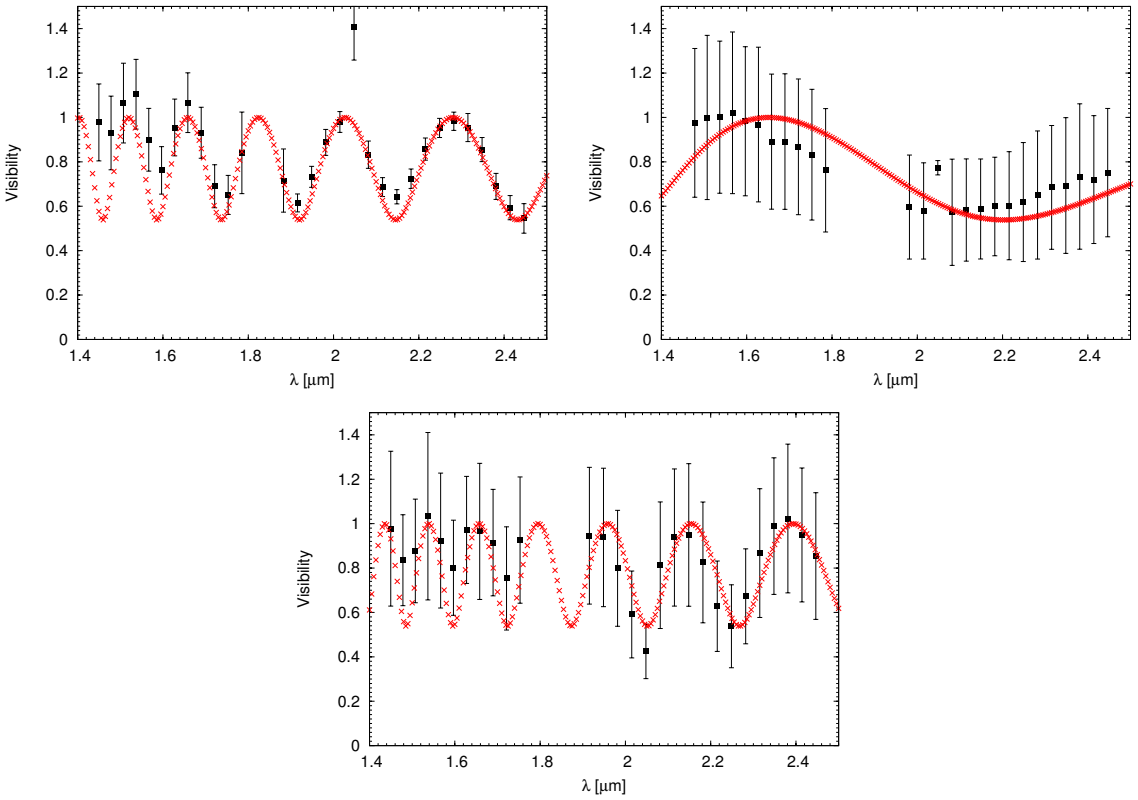

Figure A.9: Visibilities of θ^1 Ori C observed on 26/12/2010.

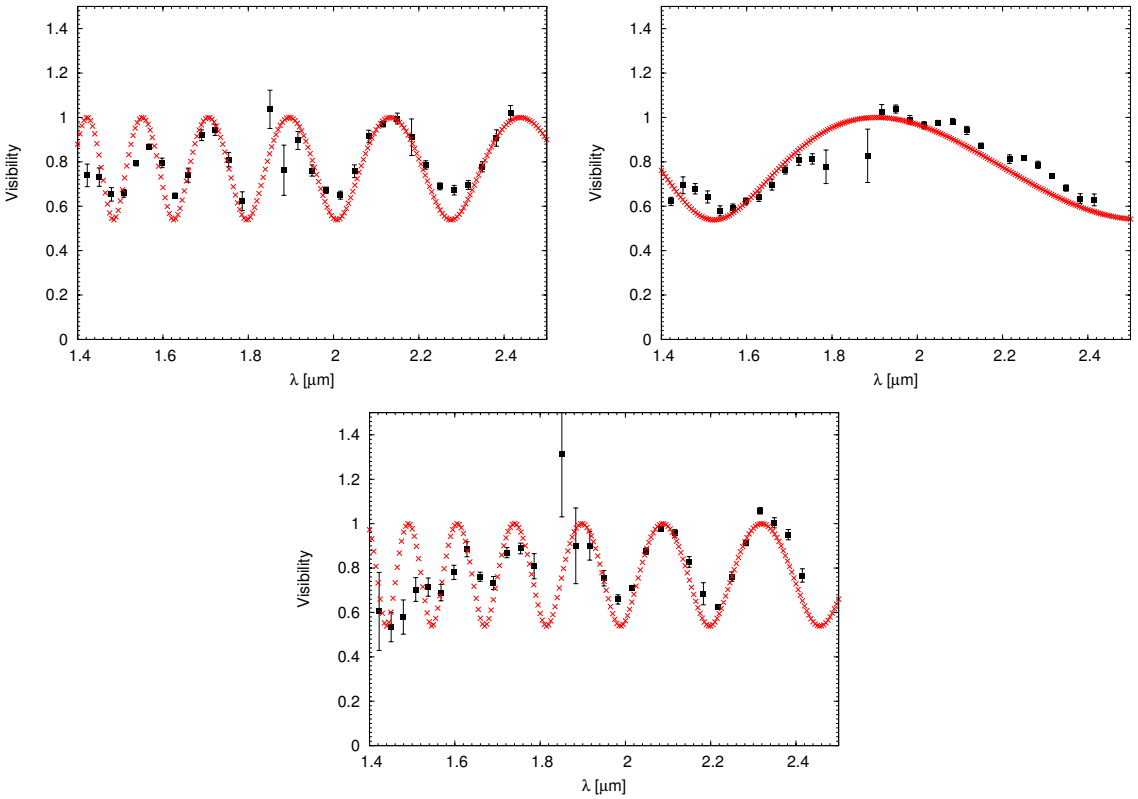

Figure A.10: Visibilities of θ^1 Ori C observed on 27/12/2010.

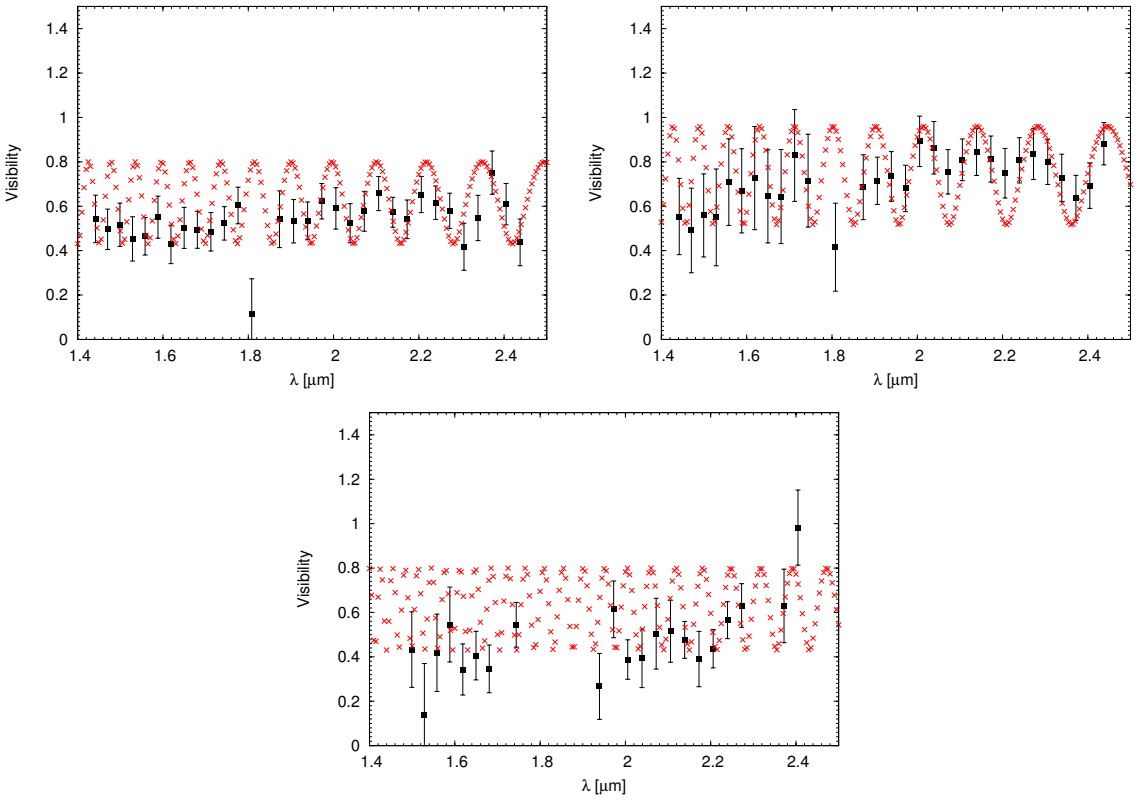

Figure A.11: Visibilities of θ^1 Ori A observed on 14/12/2010.

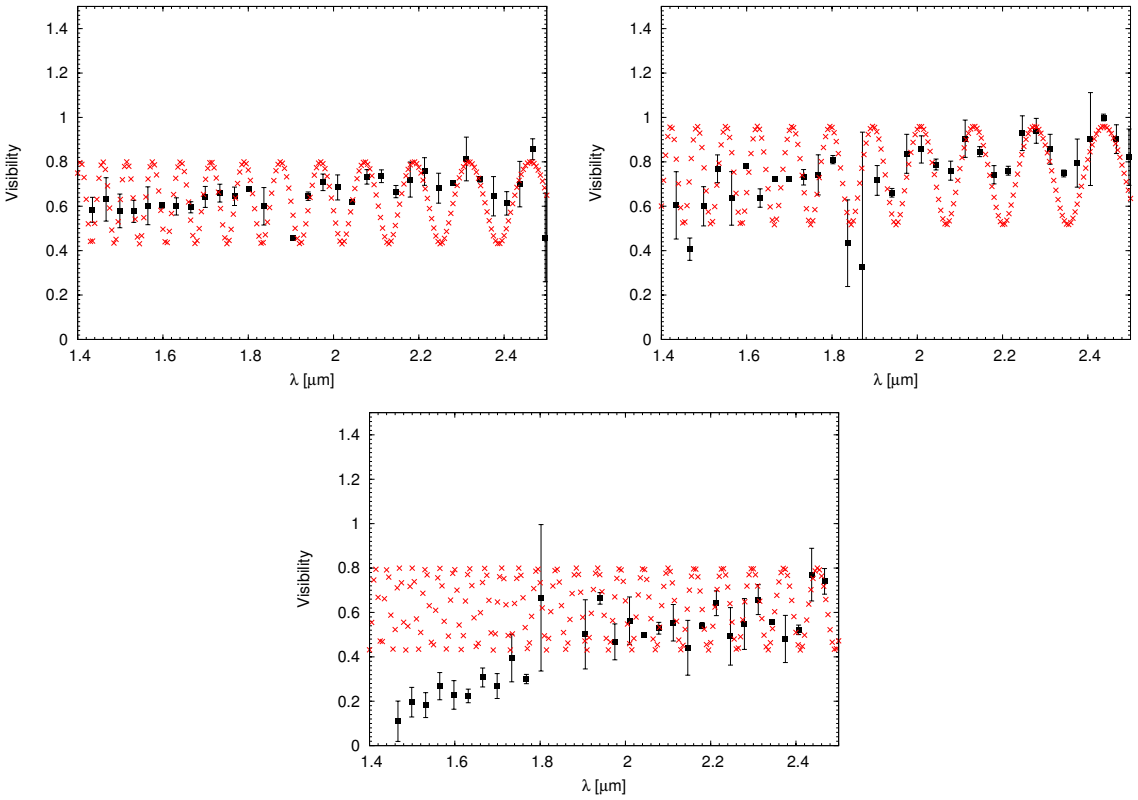

Figure A.12: Visibilities of θ^1 Ori A observed on 29/10/2011.

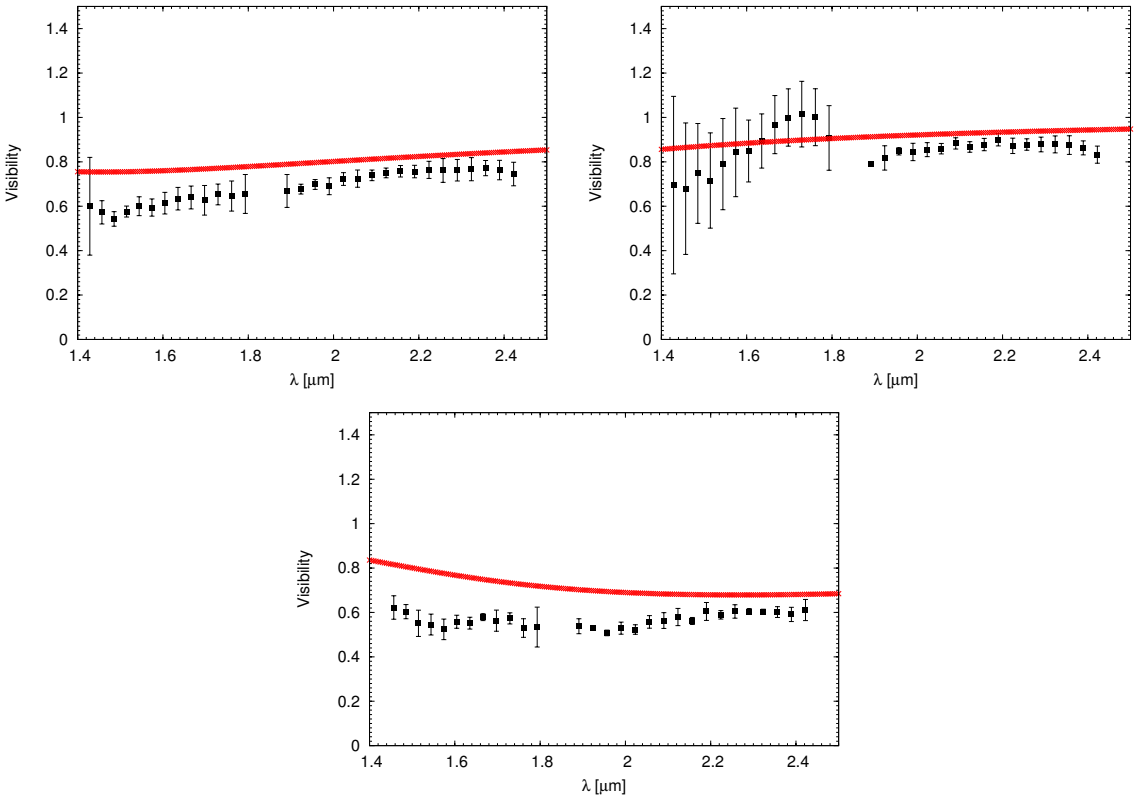

Figure A.13: Visibilities of θ^1 Ori D observed on 17/01/2011.

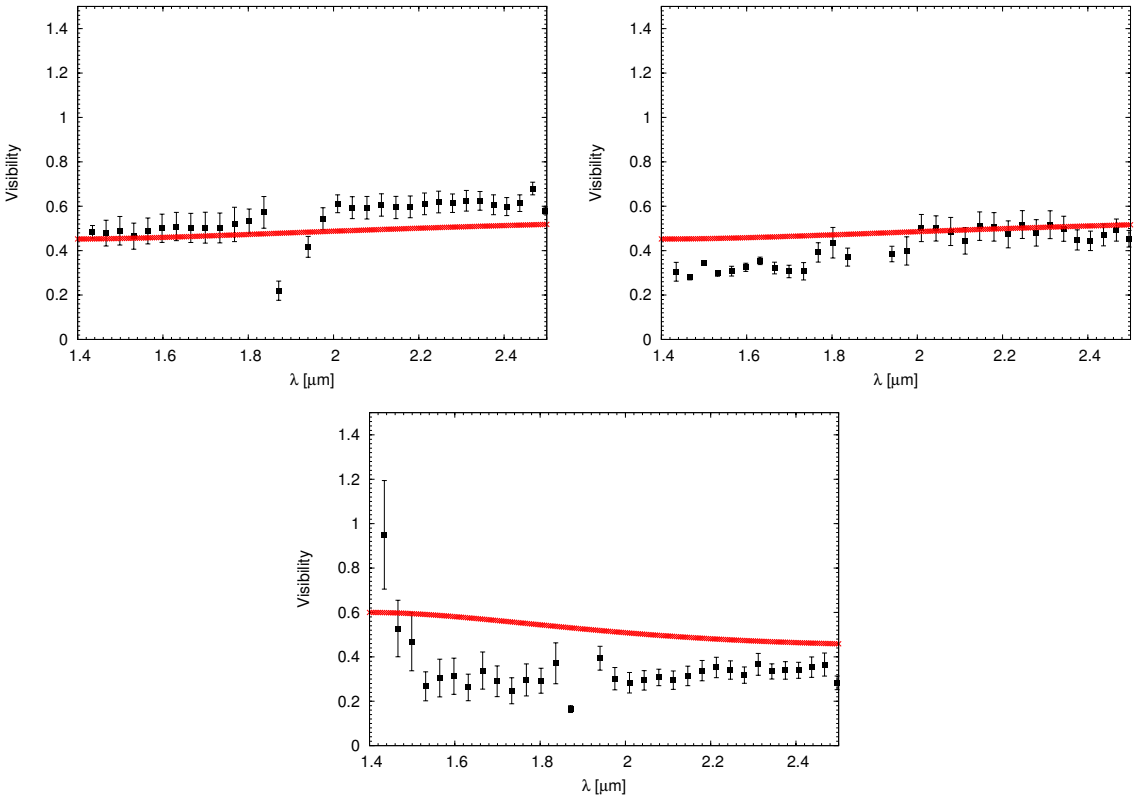

Figure A.14: Visibilities of θ^1 Ori D observed on 30/10/2011.

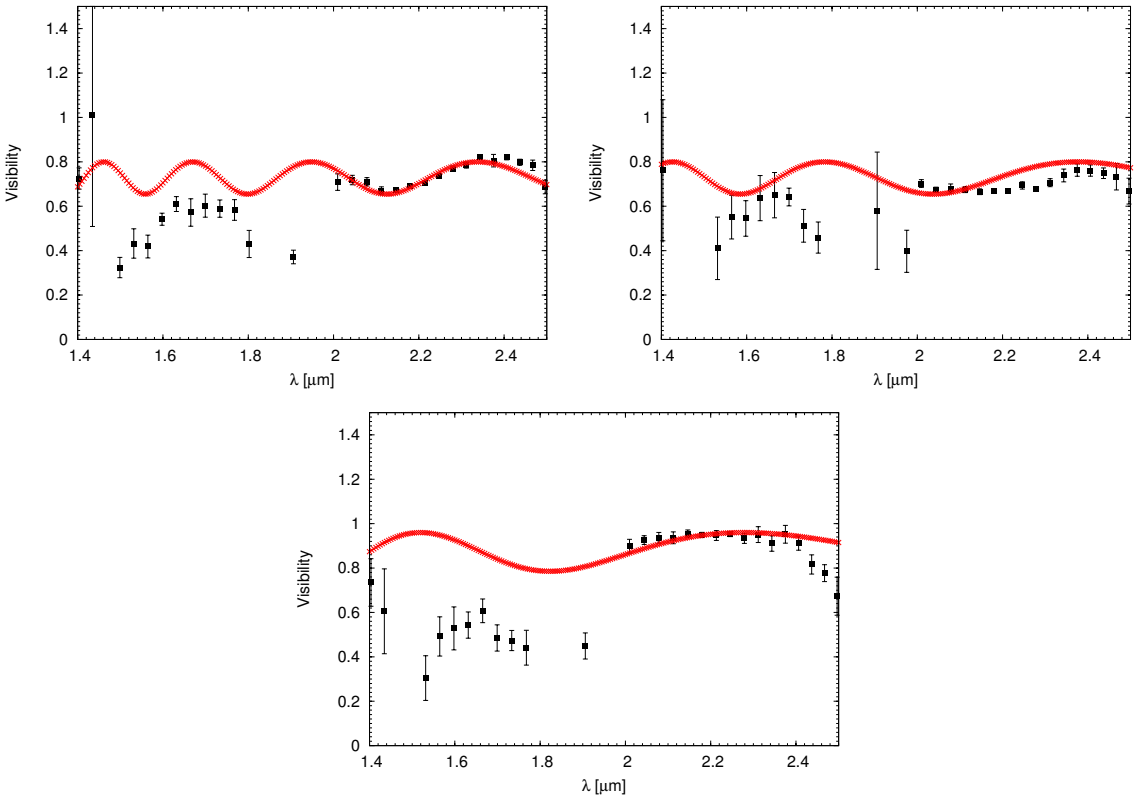

Figure A.15: Visibilities of ν Ori observed on 31/12/2011.

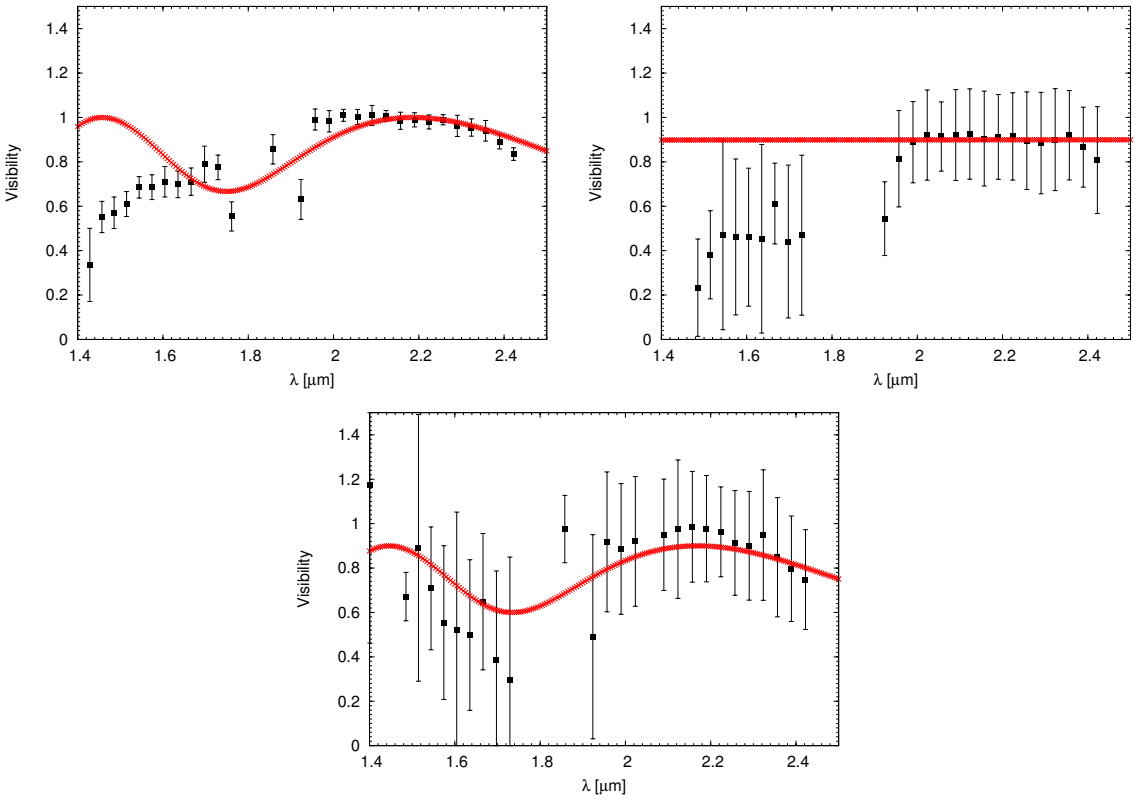

Figure A.16: Visibilities of ν Ori observed on 26/03/2011.

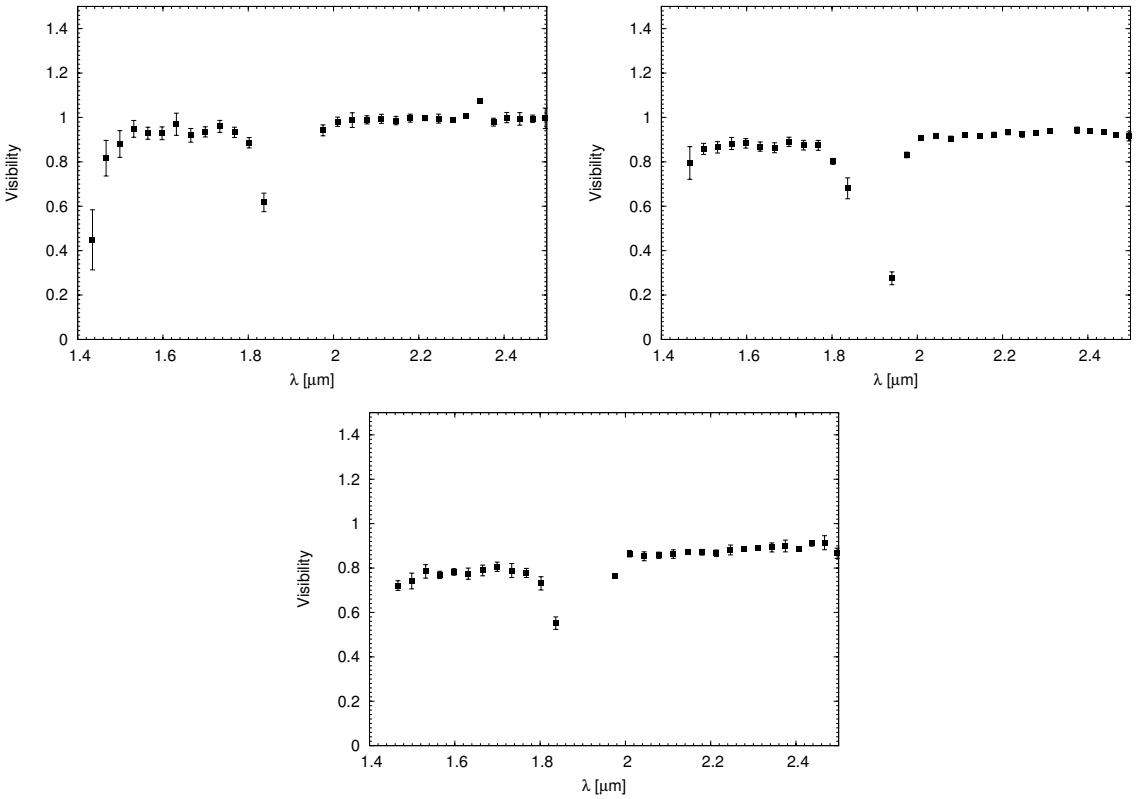

Figure A.17: Visibilities θ^2 Ori A of observed on 31/12/2011.

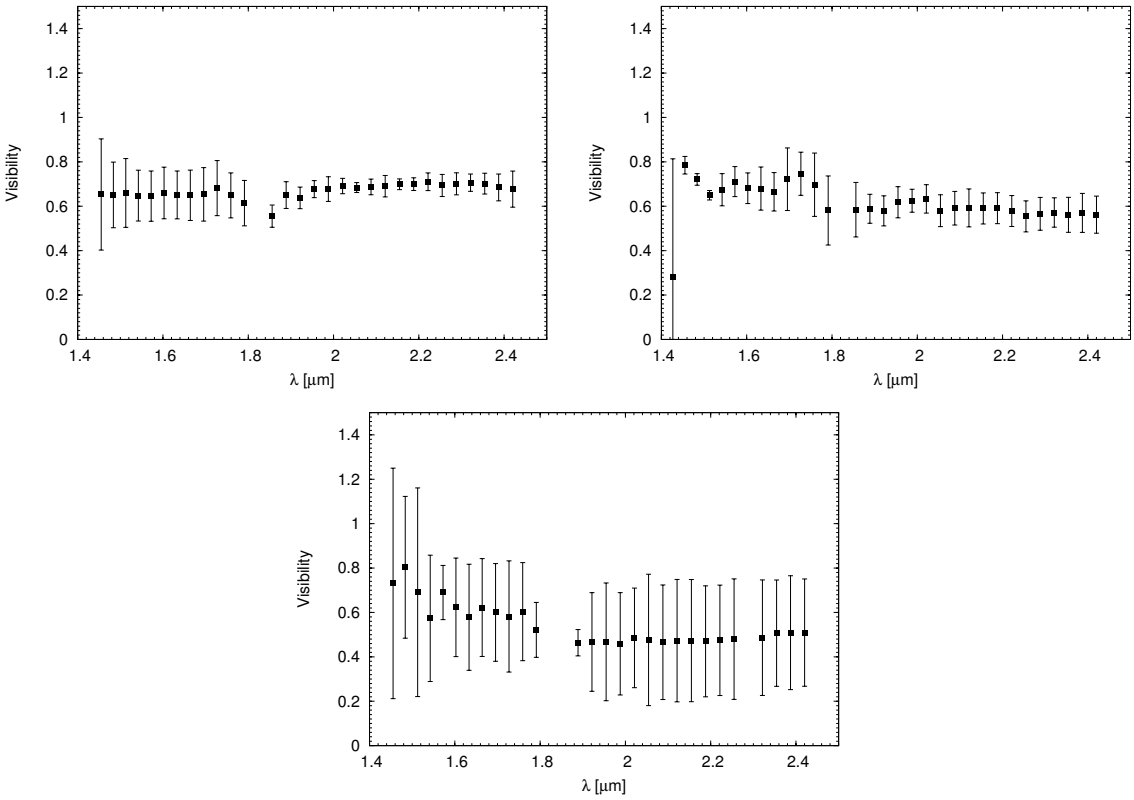

Figure A.18: Visibilities of T Ori observed on 18/01/2011.

Appendix B

Acknowledgements

Diese Arbeit wäre nicht möglich gewesen ohne die Hilfe und Unterstützung von vielen Menschen. Als erstes möchte ich mich bei meinem Doktorvater Thomas Preibisch bedanken der mir die Möglichkeit gegeben hat an diesem Projekt zu arbeiten. Insbesondere möchte ich mich bedanken für die tolle Betreuung, die Unterstützung beim Entwickeln und Durchführen von eigenen Ideen, sowie die Möglichkeit, viele interessante Konferenzen und Workshops zu besuchen. Ein ganz besonderer Dank gilt Thorsten, der stets Zeit für meine Probleme und Ideen hatte und es mir sehr einfach gemacht hat, jede noch so dumme Frage zu stellen die aufkam. Ich bin sehr froh, einen so hilfreichen und kompetenten Betreuer gehabt zu haben! Vielen Dank an dieser Stelle auch an die komplette "Young stars and star formation" Arbeitsgruppe für die angenehme Arbeitsatmosphäre und das Interesse an meiner Arbeit. Desweiteren auch herzlichen Dank an Achim Weiss, der sich bereiterklärt hat diese Arbeit zu lesen und zu bewerten.

Viele Mitarbeiter der Sternwarte haben dazu beigetragen meine Zeit dort angenehmer und abwechslungsreicher zu machen. Hier möchte ich mich zunächst bei Tadziu für das Lösen diverser Computerprobleme sowie die Berge von Keksen und Schokolade bedanken. Sehr viel Spaß haben mir auch die täglichen Kaffeerunden und die darin enthaltenen Diskussionen über Wissenschaft und den Rest der Welt gemacht. Vielen Dank an die gesamte Kaffe- (und Tee-) Gruppe dafür die Arbeitszeit viel unterhaltsamer zu machen! Die letzten drei Jahre hatte ich ebenfalls viel Glück mit meinen Büronachbarn, die ein konzentriertes Arbeiten möglich gemacht haben, aber trotzdem immer für interessante oder lustige Gespräche zu haben waren. Namentlich erwähnen möchte ich an dieser Stelle noch Rhea, Steffi und Natascha die immer ein offenes Ohr für mich hatten und mit denen ich viele schöne Abende verbracht habe.

Ganz besonders wichtig in so einer manchmal doch recht anstrengenden Zeit ist der Rückhalt durch Freunde und Familie. Ich möchte mich daher auch bei Sabine, Hilde und Kurt bedanken, die es mir leichter gemacht haben, mich in München einzuleben und zuhause zu fühlen. Ich danke auch allen, die sich aus der Heimat auf den weiten Weg nach München gemacht haben, um mich zu besuchen und die immer daran geglaubt haben, dass ich irgendwann fertig werde: Georg, Kathi S., Andrea, Andreas, Lara, Kathi K., Henning, Jasmin, und natürlich auch allen, die ich jetzt vergessen habe.

Den letzten Abschnitt dieser Danksagung ist den für mich wichtigsten Menschen in meinem Leben gewidmet: Meinen Brüdern Thomas und Simon, meinen Eltern, und Julian. Meiner Familie danke ich zunächst daür, dass sie meine Entscheidungen immer mitgetragen und mich darin unterstützt hat, auch wenn das bedeutet, dass ich weit von ihnen entfernt bin und wir uns selten sehen. Meinem Bruder

Thomas (und Kathi) möchte ich auch nochmal dafür danken, dass sie sich extra auf den Weg gemacht haben um für diese Arbeit ein schönes Foto vom Dom zu machen. Mama und Papa, ich möchte euch ganz besonders dafür danken, dass ich mich immer auf euch verlassen konnte und kann und dass ihr mir Sicherheit gebt und mich aufmuntert, auch wenn mal nicht alles nach Pan verläuft. Insbesondere aber wäre das Schreiben dieser Arbeit nicht möglich gewesen ohne die Unterstützung von meinem Freund Julian. Ich danke dir, dass du mich und meine auch manchmal schlechte Laune in den letzten Jahren ertragen, mich getröstet, für mich gekocht und für viel Spass gesorgt hast (und noch so vieles mehr, dass den Rahmen dieser Danksagung aber wohl sprengen würde).